USING NUCLEAR DATA AND MONTE-CARLO TECHNIQUES TO STUDY AREAL DENSITY AND MIX IN D_2 INERTIAL CONFINEMENT FUSION IMPLOSIONS

by

Shinya Kurebayashi

B.A. Physics, University of Montana, 2000

Submitted to the Department of Physics
in partial fulfillment of the requirements for the degree of

Master of Science in Physics
at the
MASSACHUSETTS INSTITUTE OF TECHNOLOGY

JUNE, 2004

Author ....
Department of Physics
March 3, 2004

Certified by ....
Richard D. Petrasso
Senior Research Scientist, Plasma Science and Fusion Center
Thesis Supervisor

Certified by ....
Miklos Porkolab
Professor of Physics
Thesis Co-Supervisor

Accepted by ....
Thomas J. Greytak
Professor of Physics
Associate Department Head for Education

USING NUCLEAR DATA AND MONTE-CARLO TECHNIQUES TO STUDY AREAL DENSITY AND MIX IN D_2 INERTIAL CONFINEMENT FUSION IMPLOSIONS

by

Shinya Kurebayashi

Submitted to the Department of Physics on March 3, 2004
in partial fulfillment of the requirements for the degree of
Master of Science in Physics

Abstract

Measurements from three classes of direct-drive implosions at the OMEGA laser system [T. R. Boehly *et al.*, Opt. Commun. **133**, 495 (1997)] were combined with Monte-Carlo simulations to investigate models for determining hot-fuel areal density (ρR_{hot}) in compressed, D_2-filled capsules, and to assess the impact of mix and other factors on the determination of ρR_{hot}. The results of the Monte-Carlo calculations were compared to predictions of commonly used models that use ratios of either secondary D^3He proton yields or secondary DT neutron yields to primary DD neutron yields to provide estimates $\rho R_{hot,p}$ or $\rho R_{hot,n}$, respectively, for ρR_{hot}. For the first class of implosions, where ρR_{hot} is low (≤ 3 mg/cm^2), $\rho R_{hot,p}$ and $\rho R_{hot,n}$ often agree with each other and are often good estimates of the actual ρR_{hot}. For the second class of implosions, where ρR_{hot} is of order 10 mg/cm^2, $\rho R_{hot,p}$ often underestimates the actual value due to secondary proton yield saturation. In addition, fuel-shell mix causes $\rho R_{hot,p}$ to further underestimate, and $\rho R_{hot,n}$ to overestimate, ρR_{hot}. As a result, values of $\rho R_{hot,p}$ and $\rho R_{hot,n}$ can be interpreted as lower and upper limits, respectively. For the third class of implosions, involving cryogenic capsules, secondary protons and neutrons are produced mainly in the hot and cold fuel regions, respectively, and the effects of the mixing of hot and cold fuel must be taken into account when interpreting the values of $\rho R_{hot,p}$ and $\rho R_{hot,n}$. From these data sets, we conclude that accurate inference of ρR_{hot} requires comprehensive measurements in combination with detailed modeling.

Thesis Supervisor: Richard D. Petrasso
Title: Senior Research Scientist, Plasma Science and Fusion Center

Thesis Co-Supervisor: Miklos Porkolab
Title: Professor of Physics

This work described here was performed in part at the LLE National Laser Users' Facility (NLUF), and was supported in part by the US DoE (grant DE-FG03-03SF22691), US DoE DP/NNSA (Cooperative Agreement DE-FG03-03NA00058), LLE (subcontract 412160-001G), and LLNL (subcontract B504974).

Acknowledgments

I would like to thank my research supervisor Richard Petrasso for giving me the opportunity to carry out this research. He provided invaluable guidance, support, and encouragement throughout the duration of my graduate education and my work on this thesis project. Discussions with Rich, Johan Frenje, Fredrick Séguin, and Chikang Li helped to elucidate many of the complex issues involved in this work. I would also like to thank Johan and Fredrick for their tremendous help with modeling, programming and interpretation, and Chikang for arranging the experiments necessary for this study. Furthermore, I am very grateful to my fellow students and friends Ryan Rygg, Joe DeCiantis, and Mike Canavan for many fruitful discussions. Many thanks to Jocelyn Schaeffer at MIT, and Sam Roberts and Candice Culligan at LLE for their help processing the data and setting up experiments. Additionally, I would like to express my appreciation for support by the engineering staff at LLE. I would also like to thank my thesis co-supervisor Mikolos Porkolab and academic advisor John Belcher for their support over the past few years.

This work is a result of a collaboration between the High Energy Density Physics group at the Massachusetts Institute of Technology (MIT), Laboratory for Laser Energetics (LLE) at the University of Rochester, and Lawrence Livermore National Laboratory. I would especially like to thank the co-authors of my paper, which has been submitted to *Physics of Plasmas*: Johan Frenje, Fredrick Séguin, Ryan Rygg, Chikang Li, Richard Petrasso, Vladimir Glebov, Jacques Delettrez, Craig Sangster, David Meyerhofer, Christian Stoeckl, John Soures, Peter Amendt, Steve Hatchett, and Bob Turner for many helpful discussions and their support.

Finally, I would like to thank my family for their encouragement and support. I thank my dear wife, Tomomi for providing unparalleled support ever since we started dating in the summer of 1996. She and our lovely daughter, Rena, have provided me with a home to relax and reboot. I would like to thank my parents for offering various forms of assistance, while always allowing me to make my own decisions. Tomomi and I are grateful for the help we received from her mother and father.

Table of Contents

List of Figures

List of Tables

1. Introduction

For several decades, scientists have been working toward the goal of generating energy using inertial confinement fusion (ICF) [1-4]. Current and near-future experiments utilize lasers to implode capsules filled with gas and ice of mainly deuterium (D), tritium (T), and helium-3 (^{3}He). The inertia of the imploding capsules confines the fuel at high density and temperature, allowing fusion reactions to take place at a high rate.

Because the cross section of the deuterium-tritium (DT) fusion reaction is significantly larger than those of other fusion reactions (Fig. 1.1), DT fuel will probably be used in future practical applications. However, the handling of DT-filled capsules is complicated by the radioactivity of tritium. As a result, many experiments for benchmarking laser and capsule performance in direct- and indirect-drive ICF experiments are performed with D_2-filled capsules; deuterium is non-radioactive, and DD reaction rates are relatively large compared to those for other non-DT fuels. Since the reactions themselves have little impact on capsule compression in current experiments, the hydrodynamics of DT capsule implosions can be predicted from measured characteristics of "hydrodynamically similar" D_2 capsule implosions.

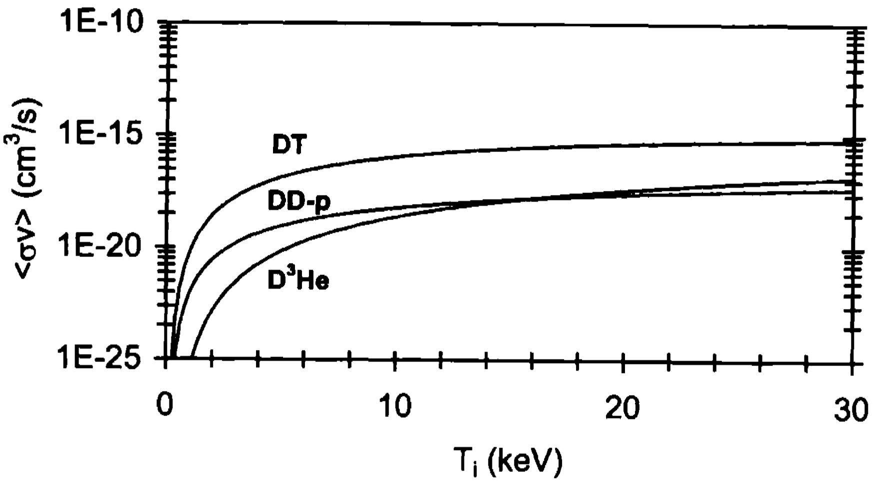

Figure 1.1: Calculated reactivity of the most relevant fusion reactions according to Ref. 5. At ion temperatures of interest, the DT reactivity is several orders of magnitude larger than the DD and D^3He reactivities.

One of the most important characteristics of an imploded target capsule is the areal density ρR, defined as the integral

$$\rho R \equiv \int_0^R \rho(r)\, dr$$

of the radially dependent local density ρ from the center of the capsule to the outer radius. It provides a measure of how well a capsule is compressed. Although ρR is actually a function of time, the values we consider here are averaged over time with a weighting factor equivalent to the fusion burn rate ("burn-averaged"). For D_2-filled capsule implosions, values of hot-fuel areal density (ρR_{hot}) have often been inferred from the ratios of secondary proton and neutron yields to primary neutron yields (Y_{2p}/Y_{1n} and Y_{2n}/Y_{1n}) using simple existing models, which assume a uniform density and temperature plasma (see Section 2-II for more details). However, these models have limitations that often result in disagreement between the proton- and neutron-implied values of ρR_{hot}.

To understand the limitations of these models, data from experiments and Monte-Carlo simulations were used. Several series of experiments, imploding three types of inertial confinement fusion capsules (Fig. 1.2), were conducted at the OMEGA laser facility [6] to obtain data for implosions with a wide range of ρR_{hot}. Several charged particle spectrometers [7], positioned at different locations on the OMEGA target chamber (Fig. 1.3), along with neutron diagnostics, were used to obtain data from nuclear particles produced within the imploding capsule (see Section 2-III). A Monte-Carlo code was developed to simulate these experiments and to obtain more realistic pictures of the implosions (see Section. 2-IV).

The following sections of this thesis will show that effects of fuel-shell mix, and density and temperature profiles, which are not considered in the existing models, have a significant impact on the production of secondary particles. These factors cause the difference in secondary proton and neutron production and require more complex analysis to infer ρR_{hot}.

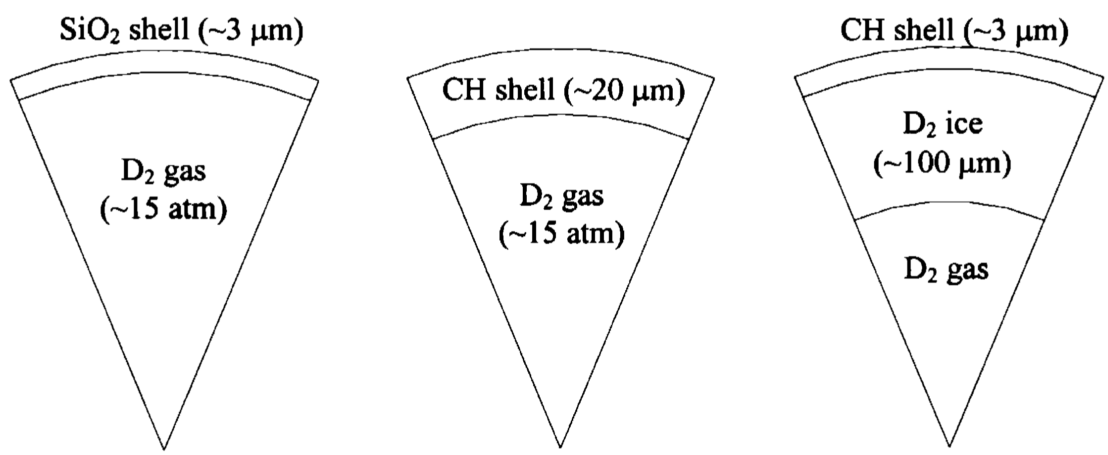

Figure 1.2: Capsules with thin glass shells (left), thick plastic shells (center), and cryogenic shells (right) were used for the study of low, medium, and high ρR_{hot} implosions, respectively. They are nominally 900 μm in diameter.

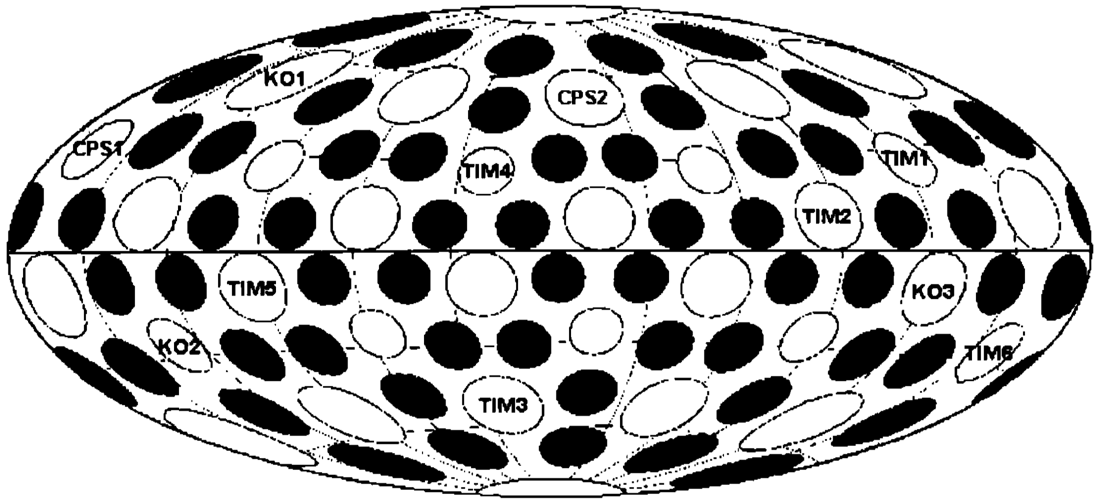

Figure 1.3: OMEGA port diagram showing the locations of two magnet-based charged-particle spectrometers (CPS1 and CPS2) as well as the available ports for Wedge-Range-Filter proton spectrometers (WRFs) [7] (TIM and KO ports). Up to six WRFs were used to obtain secondary proton spectra simultaneously from different directions.

The paper "Using nuclear data and Monte-Carlo techniques to study areal density and effects of mix in D_2 implosions," which has been submitted to Physics of Plasmas, is shown in Section 2. The section has its own appendix (Appendix A) and references. Unsolved problems and future work are described in Section 3. A Monte-Carlo program and the results of the simulations are explained in detail in Appendices B and C, respectively. Experimental data is compiled in Appendix D.

2. Using nuclear data and Monte-Carlo techniques to study areal density and effects of mix in D_2 implosions (paper submitted to *Physics of Plasmas*)

S. Kurebayashi, J. A. Frenje, F. H. Séguin, J. R. Rygg, C. K. Li, and R. D. Petrasso[a]
Plasma Science and Fusion Center, Massachusetts Institute of Technology, Cambridge, Massachusetts 02139

V. Yu. Glebov, J. A. Delettrez, T. C. Sangster, D. D. Meyerhofer[b], C. Stoeckl, and J. M. Soures
Laboratory for Laser Energetics, University of Rochester, Rochester, New York 14623

P. A. Amendt, S. P. Hatchett, and R. E. Turner
Lawrence Livermore National Laboratory, Livermore, California 94550

ABSTRACT

Measurements from three classes of direct-drive implosions at the OMEGA laser system [T. R. Boehly *et al.*, Opt. Commun. **133**, 495 (1997)] were combined with Monte-Carlo simulations to investigate models for determining hot-fuel areal density (ρR_{hot}) in compressed, D_2-filled capsules, and to assess the impact of mix and other factors on the determination of ρR_{hot}. The results of the Monte-Carlo calculations were compared to predictions of simple commonly used models that use ratios of either secondary D^3He proton yields or secondary DT neutron yields to primary DD neutron yields to provide estimates $\rho R_{hot,p}$ or $\rho R_{hot,n}$, respectively, for ρR_{hot}. For the first class of implosions, where ρR_{hot} is low (≤ 3 mg/cm^2), $\rho R_{hot,p}$ and $\rho R_{hot,n}$ often agree with each other and are often good estimates of the actual ρR_{hot}. For the second class of implosions, where ρR_{hot} is of order 10 mg/cm^2, $\rho R_{hot,p}$ often underestimates the actual value due to secondary proton yield saturation. In addition, fuel-shell mix causes $\rho R_{hot,p}$ to further underestimate, and $\rho R_{hot,n}$ to overestimate, ρR_{hot}. As a result, values of $\rho R_{hot,p}$ and $\rho R_{hot,n}$ can be interpreted as lower and upper limits, respectively. For the third class of implosions, involving cryogenic capsules, secondary protons and neutrons are produced mainly in the hot and cold fuel regions, respectively, and the effects of the mixing of hot and cold fuel must be taken into account when interpreting the values of $\rho R_{hot,p}$ and $\rho R_{hot,n}$. From these data sets, we conclude that accurate inference of ρR_{hot} requires comprehensive measurements in combination with detailed modeling.

a) Also visiting Senior Scientist, Laboratory for Laser Energetics, University of Rochester.

b) Also Department of Mechanical Engineering, Physics and Astronomy.

I. Introduction

Maximizing the hot-fuel areal density (ρR_{hot}) and understanding the effects of mix upon it are fundamental issues of inertial confinement fusion (ICF).[1-3] One method used to estimate ρR_{hot} of D_2-filled capsule implosions is to measure the yields of secondary protons (Y_{2p}) and/or secondary neutrons (Y_{2n}) relative to the primary neutron yield (Y_{1n}).[4-12] These secondary particles result from sequential reactions in which the energetic primary products of reactions,

$$D + D \rightarrow n(2.45\text{ MeV}) + {}^3He(0.82\text{ MeV}), \quad (1)$$

$$D + D \rightarrow p(3.02\text{ MeV}) + T(1.01\text{ MeV}), \quad (2)$$

undergo fusion reactions with thermal deuterons in the fuel

$${}^3He(\leq 0.82\text{ MeV}) + D \rightarrow p(12.5 - 17.4\text{ MeV}) + {}^4He(6.6 - 1.7\text{ MeV}), \quad (3)$$

$$T(\leq 1.01\text{ MeV}) + D \rightarrow n(11.9 - 17.2\text{ MeV}) + {}^4He(6.7 - 1.4\text{ MeV}). \quad (4)$$

These processes produce secondary particles with spectra spread over significant energy intervals due to the kinetic energy of the primary reactants. The secondary particle yields are typically two to three orders of magnitude lower than the primary yield, and the ratios Y_{2n}/Y_{1n}, and Y_{2p}/Y_{1n} (which are linearly dependent on ρR_{hot} in certain plasma regimes) can each be used to infer a value of ρR_{hot} for implosions of D_2-filled capsules in both direct- and indirect-drive experiments.[12-15] In those studies, the simple "hot-spot" and/or the "uniform" models were used to relate these ratios to ρR_{hot}. Although these simple models have been widely used to infer a value of ρR_{hot}, they have some serious limitations which can result in misinterpretation and errors (as described in Section II); one manifestation of these problems is often disagreement between the proton- and neutron-inferred values of ρR_{hot} calculated from experimental data (see Fig. 1). These deviations are related to a combination of mix, temperature profile, and the difference between the cross section for secondary reactions (3) and (4). These factors can cause secondary protons and neutrons to be produced in different regions of the compressed capsules (Fig. 2). In addition, other workers have noted some puzzling issues with recent secondary neutron measurements in indirect drive implosions on OMEGA.[16] In that work, the authors observed a factor-of-three larger Y_{2n}/Y_{1n} ratio and a narrower secondary neutron spectrum than predicted for these low-convergence implosions (where mix should be relatively unimportant). In contrast, for high-convergence implosions, they found better agreement between measured and predicted Y_{2n}/Y_{1n} values.

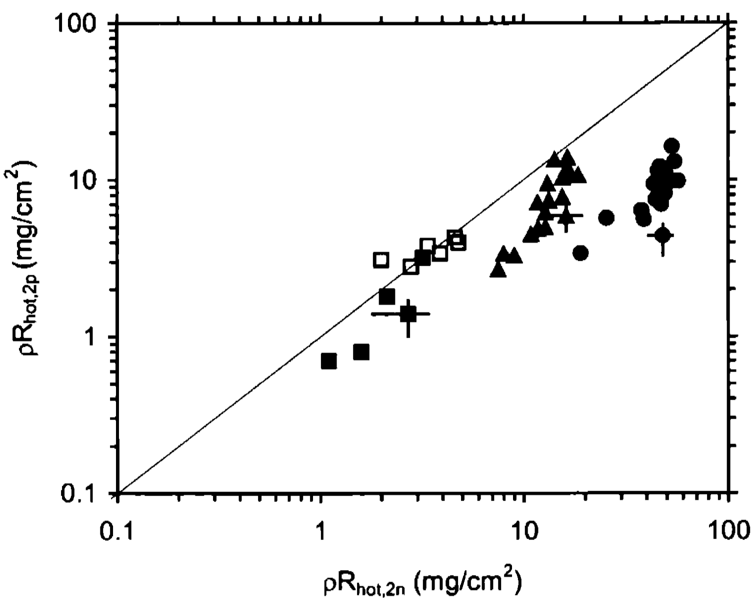

FIG. 1. Secondary proton- and neutron-implied values of ρR_{hot} are compared for implosions of small ρR_{hot} (squares), medium ρR_{hot} (triangles), and cryogenic (circles) capsules at the OMEGA laser facility. For small ρR_{hot} implosions, the values of ρR_{hot} inferred from secondary protons and neutrons using the simple hot-spot model agree well. It is also shown that values of ρR_{hot} are larger for implosions with ~12-kJ laser energy (open squares) than for implosions with ~23-kJ laser energy (closed squares) (Fig. A.1). For these dramatically overdriven implosions, it is possible that the effects of mix are coming back into play, as indicated by the observation that $\rho R_{hot,2n}$ is larger than $\rho R_{hot,2p}$. However, for implosions with larger ρR_{hot}, the values inferred from secondary neutrons are always larger than the values from secondary protons. The error bars shown are typical of each type of implosion; they include uncertainties in the measurements and in the assumed values of the density.

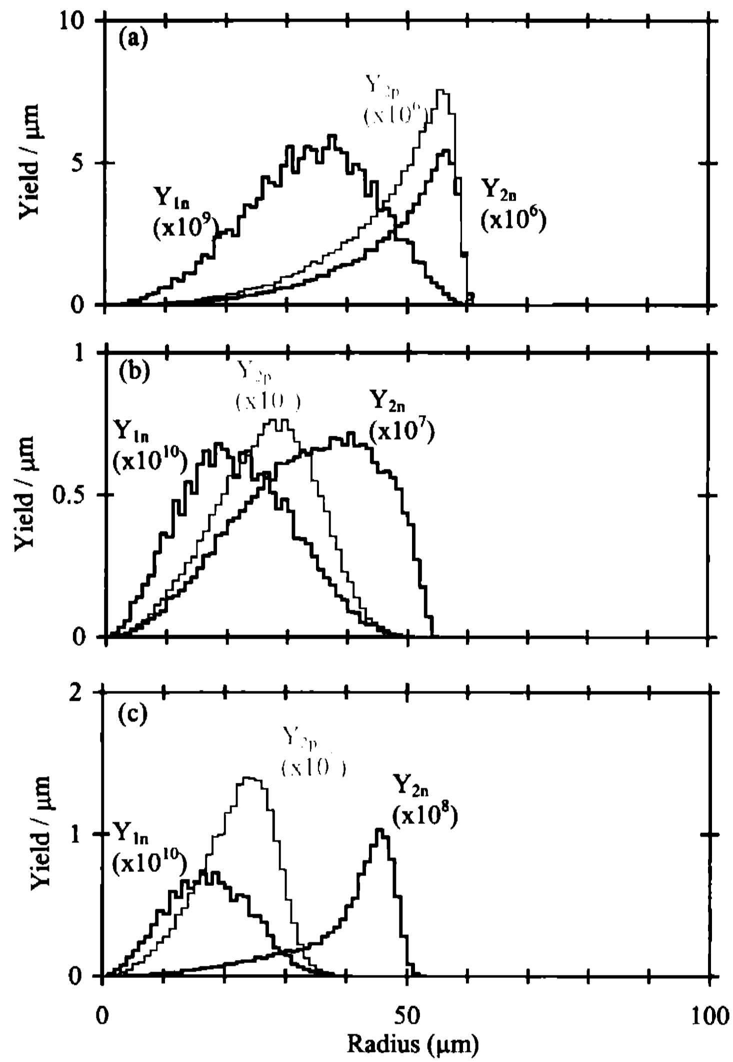

FIG. 2. Calculated radial distributions of primary and secondary birth positions per unit length for (a) low ρR implosion 30981, (b) medium ρR implosion 27443, and cryogenic implosion 28900. For low ρR implosions, where ρR_{2p} and ρR_{2n} agree reasonably well, birth positions of secondary protons and neutrons are virtually identical. However, for medium ρR and cryogenic implosions, where ρR_{2n} is always larger than ρR_{2p}, secondary neutrons are produced in more outer regions compared to secondary protons. Note that calculated radial distributions of primary birth rates per unit volume (as opposed to unit radius) are shown in FIGs. A.3, A.4, and A.5 for these three implosions.

In previous work,[12] high-resolution secondary-proton spectra were obtained during experiments at the OMEGA laser facility.[17] The yields were used with measured neutron yields to estimate ρR_{hot} with the hot-spot and uniform models and it was shown that the Y_{2p}/Y_{1n} –

inferred ρR_{hot} was often lower than the Y_{2n}/Y_{1n}, -inferred ρR_{hot}. This was attributed to the effects of fuel-shell mix, and it was suggested that the two inferences might be considered lower and upper limits, respectively. In this paper, that work is extended to cover a wider range of implosion types and to include Monte-Carlo simulations that allow a detailed study of the implications of more realistic models of the compressed core on the secondary production. Section II describes the hot-spot and uniform models and their limitations. Section III describes the experiments and the range of parameters that are measured. Section IV describes a Monte-Carlo program that has been developed to model the implosions to understand how particle production occurs. Results from both experiments and Monte-Carlo calculations are discussed in Section V, with an emphasis on how ρR_{hot} is related to the yields of primary and secondary particles. The results are summarized in Section VI.

II. Primary and secondary products

The hot-spot and uniform models have been commonly used to relate Y_{2p}/Y_{1n} and Y_{2n}/Y_{1n} to ρR_{hot}. The hot-spot model assumes that an imploded capsule is a sphere of uniform density and temperature and that all primary reactions occur at the very center of the capsule. A fraction of the primary ^{3}He (tritons) fuse with thermal deuterons, producing secondary protons (neutrons) as they move radially outward. As the primary particles travel through the D plasma, they lose energy and the probability for producing secondary particles along the path varies greatly since the secondary D^{3}He and DT fusion cross sections (σ_{D3He} and σ_{DT}) are strong functions of the primary ^{3}He and T energies (Fig. 3a).[18] σ_{D3He} peaks at ~ 0.65 MeV, close to the ^{3}He birth energy (0.8 MeV), while σ_{DT} peaks at ~ 0.18 MeV, significantly lower than the triton birth energy (1.0 MeV). As a result, secondary protons are mainly produced near the ^{3}He birth position, while secondary neutrons are mainly produced further away from the triton birth position (see Fig. 3b). This information is used to calculate ρR_{hot} from Y_{2p}/Y_{1n} and Y_{2n}/Y_{1n}, and the resulting dependencies are shown in Fig. 4 for D plasmas with different temperatures and densities. The ratios each saturate at different values of ρR_{hot} for different temperatures and densities, because the primary ^{3}He and tritons generally have significantly different ranges in the plasma. If either particle stops before leaving the fuel, it will not sample the entire ρR_{hot}, and the implied value of ρR_{hot} underestimates the actual value. Y_{2p}/Y_{1n} does not depend on temperature until it starts to saturate, while Y_{2n}/Y_{1n} is sensitive to temperature well below the saturation level. Therefore, without a reasonable estimate of plasma temperature, Y_{2n}/Y_{1n} cannot be used to accurately infer ρR_{hot}.

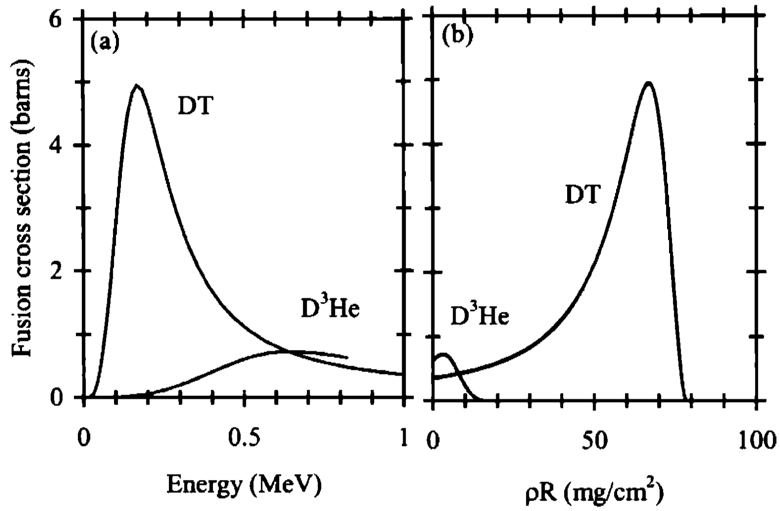

FIG. 3. (a) Dependence of the secondary D^3He (DT) reaction cross section on the energy of the primary ^3He (T) in a cold D plasma.[18] The D^3He reaction cross section is peaked close to the birth energy of ^3He, while the DT reaction cross section peaks dramatically after T has lost most of its energy. (b) As a result, secondary protons are created close to the birth points of primary ^3He (here defined as $\rho R=0$) while secondary neutrons are produced away from the birth points of primary T ($\rho R=0$). Although this plot is for a 1g/cc, 3keV D plasma, it looks similar for plasmas with different densities and temperatures.

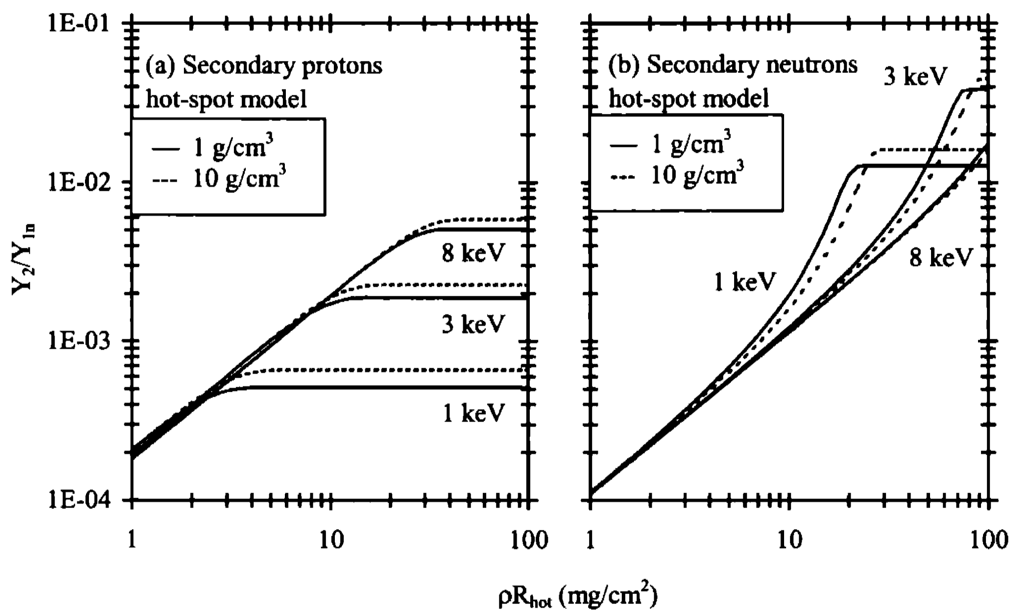

FIG. 4. (a) Y_{2p}/Y_{1n} and (b) Y_{2n}/Y_{1n} as functions of ρR_{hot} for a 1, 3, and 8 keV D plasma of 1 g/cc (solid line) and 10 g/cc (dashed line) using the hot-spot model. The energy losses of primary ^3He and T were calculated according to Ref. 19, and the fusion cross sections were calculated according to Ref. 18. Y_{2p}/Y_{1n} is temperature independent until it reaches the saturation levels. In contrast, Y_{2n}/Y_{1n} is temperature dependent well below saturation levels.

The uniform model assumes that the primary particles are produced uniformly in a sphere of constant density and temperature. The Y_{2p}/Y_{1n} and Y_{2n}/Y_{1n} dependencies show similar behavior to the hot-spot model. The primary difference is that values of ρR_{hot} implied by the uniform model are always larger than values from the hot-spot model because the mean path length of primary particles in the D plasma is shorter by 25% in the uniform model, when saturation has not occurred. The simulations described in Section V indicate that the hot-spot model gives more meaningful values of ρR_{hot} than the uniform model. Thus, the hot-spot model will be used throughout the remainder of the paper.

Both models have limitations which can introduce errors into the analysis of ρR_{hot}. These include the saturation of Y_{2p} and Y_{2n} and the uncertainty introduced by the temperature dependence of Y_{2n}. The shapes of temperature and density profiles, and the presence of fuel-shell mix[20-22] can have substantial impact on secondary particle production. In reality, the temperature is highest and the density is lowest at the center of the implosion. As the temperature decreases and the density increases, the rate of energy loss of primary particles becomes larger. This typically causes a reduction of the secondary proton production rate and an enhancement of the secondary neutron production rate (see Fig. 3a). Fuel-shell mix lowers the temperature in the mix region, which increases the energy loss rate and results in a further reduction of the secondary proton production rate and an enhancement of the secondary neutron production rate. Shell material mixed into the fuel can directly affect secondary production by increasing the energy lost by T and ^{3}He after traveling through a given amount of D, due to the higher effective charge of the shell material mixed in.

III. Experiments

In the direct-drive experiments described here, distributed phase plates,[23] polarization smoothing using birefringent wedges,[24] and 1-THz, two-dimensional smoothing by spectral dispersion[25] were applied to smooth the OMEGA laser beams in order to enhance implosion uniformity and the nuclear reaction rate. Three types of capsules were used to study implosions with a wide range of areal densities. Low-ρR_{hot} implosions were studied using thin (~3 μm) glass (SiO_2) shells filled with ~15 atm of D_2. Some of these capsules were irradiated with a 1-ns square pulse delivering 23 kJ of on-target energy, while others were irradiated with a shorter (600 – 800 ps) pulse with on-target energy of ~12 kJ.[26] Medium and large ρR implosions were studied using capsules with thick (~20 μm) plastic (CH) shells filled with ~15 atm of D_2, and cryogenic capsules with a ~100 μm layer of D_2 ice enclosed within a 3~5 μm thick CH shell, respectively. They were all irradiated with 1-ns square pulses, delivering 23 kJ of on-target energy.

Charged-particle data were collected with two types of spectrometers. Wedge-range-filter proton spectrometers[12,27] provided secondary-proton spectra from up to six different directions simultaneously. These spectra were used to calculate the yield and mean energy of secondary protons. Two magnet-based charged-particle spectrometers[27] provided the spectra of primary protons and tritons for low ρR implosions. Neutron data were obtained from three diagnostics. Neutron time-of-flight detectors[28] provided primary and secondary neutron yields as well as primary-neutron-yield-averaged ion temperature ($\langle T_i \rangle_{Y1n}$), and a neutron temporal diagnostic[29] measured the peak primary neutron production time and the DD burn duration. In addition, secondary-neutron spectra were obtained from the 1020-scintillator array[30] on some of the more recent implosions.

The data from each implosion then includes the five quantities, Y_{1n}, Y_{2n}, Y_{2p}, $<T_i>_{Y1n}$ and $<E_{2p}>$, which will be matched to simulations in the next section. In addition, the spectral energy distributions of the secondary protons (and sometimes secondary neutrons) will be compared with the simulations. The yields and $<T_i>_{Y1n}$, together with a realistic plasma density, can also be used to determine what the simple hot-spot and uniform models imply for values of $\rho R_{hot,2p}{}^{exp1}$ and $\rho R_{hot,2n}{}^{exp1}$ (where the superscript exp1 refers to use of the measured $<T_i>_{Y1n}$ as the characteristic ion temperature).

IV. Monte-Carlo simulations

A Monte-Carlo program was developed to model the experiments described in Section III. This allows us to use more realistic temperature and density profiles than those in the hot-spot and uniform models. The burn-averaged ion temperature profile [$T_i(r)$] and the shell (or cold fuel, for cryogenic capsules) density profile [$\rho_{cold}(r)$] are assumed to have super- or sub-Gaussian profiles, and the six input parameters are: T_{i0}, T_{iw}, T_{ip}, S_{r0}, S_w, and S_p characterizing the temperature and density profiles

$$T_i(r) = T_{i0} \exp[-(r/T_{iw})^{Tip}] \tag{5}$$

and

$$\rho_{cold}(r) = \rho_{cold0} \exp\{-[(r-S_{r0})/S_w]^{Sp}\}. \tag{6}$$

These parameters are varied to produce simulated particle production that best fits the measured data for each implosion. The hot-fuel density profile [$\rho_{hot}(r)$] is calculated assuming that the plasma is isobaric out to the peak shell pressure region; with this constraint ρ_{cold0} is then adjusted in order to conserve the fuel mass. (The initial fuel mass is calculated based on the initial fuel pressure and the size of the capsule.)

For computational purposes, each primary particle is assumed to produce a secondary particle, and a spectrum of particles per unit energy dN_2/dE is obtained. Since only a small fraction of the primary particles actually undergo secondary reactions, the secondary yield and spectrum need to be normalized according to $Y_2 = \langle P_2 \rangle Y_1$ and $dY_2/dE \approx \langle P_2 \rangle Y_1 (dN_2/dE)/N_2$; $\langle P_2 \rangle \equiv \langle \int n_D(l)\sigma_{sec}(l)dl \rangle$ is the probability of primary-to-secondary conversion, calculated in the program as the primary-yield-weighted mean value of the line integral of the D number density (n_D) times the secondary fusion cross section (σ_{sec}) for all possible primary particle trajectories. The primary particle production is determined by the density and temperature profiles. The particles are followed along their trajectories through the capsule until either they escape or lose all of their energy. The probability of a secondary fusion reaction is calculated along the path of the primary particle, and then the birth position, direction, and energy of the secondary particle are calculated. The energy loss of the secondary particles is calculated to determine its contribution to a secondary spectrum. In addition to these spectra, the radial distributions of the primary and secondary particle birth positions are recorded to illustrate the effects of profiles and fuel-shell mix.

Since the model is static, the primary yield is calculated by multiplying the burn profile by the burn duration (full-width-half-maximum of the neutron production rate); therefore, the error in the measurement of the burn duration is included in the error of the primary yield. $\langle E_{2p} \rangle$ is calculated from the secondary-proton spectrum, and $\langle T_i \rangle_{Y1n}$ is determined in the region where the primary particles are produced.[31] Each of the six input parameters is varied over a large range, initially using large steps to identify the region of small χ^2. This region is then more carefully explored using finer grids; as a result, the six-dimensional parameter space is explored completely. For each set of model parameters, the predicted values of the experimentally-measured quantities are calculated and the quality of agreement with the data from a particular implosion is characterized with the total χ^2, which takes account of uncertainties in the experimental measurements. For each implosion, it is found that multiple local minima exist within the space of model parameters but that there is one clear region with the smallest values of χ^2. Errors on the values of individual model parameters are then estimated by asking how much they can be changed without causing the total χ^2 to increase by more than one. Although the widths and shapes of secondary-proton spectra are not used as fit criteria, it will be seen that the predicted spectra match the measured spectra quite well; this fact provides extra confidence that the best-fit model parameters are realistic.

The characteristics of the best-fit model for each implosion were used to determine how realistic the hot-spot-model inferred values of ρR_{hot} are. Values of Y_{2p}/Y_{1n}, Y_{2n}/Y_{1n}, $\langle T_i \rangle_{Y1n}$ and plasma density from the simulations were used to infer $\rho R_{hot,2p}^{sim1}$ and $\rho R_{hot,2n}^{sim1}$ according to Fig. 4 (the superscript sim1 indicates that $\langle T_i \rangle_{Y1n}$ was used as the characteristic ion temperature). The values of $\rho R_{hot,2p}^{sim2}$ and $\rho R_{hot,2n}^{sim2}$ were calculated assuming that the appropriate temperatures are averages weighted by secondary yields ($\langle T_i \rangle_{Y2p}$ and $\langle T_i \rangle_{Y2n}$, respectively). These values were then compared with $\rho R_{hot}^{int} \equiv \int \rho_D dr$, integrated over the hot-fuel region.

V. Results

A. Low areal density implosions

For low-ρR_{hot} implosions, the primary ^{3}He and T traverse the entire hot-fuel region, and the values of ρR_{hot} inferred from secondary protons and neutrons using the hot-spot (or uniform) model generally agree with each other and usually give a reasonable estimate of the actual value of ρR_{hot}. This is shown experimentally by the square points in Fig. 1, which compares values of $\rho R_{hot,2p}{}^{expl}$ and $\rho R_{hot,2n}{}^{expl}$. These values were inferred according to Fig. 4 assuming a D plasma with a a temperature of $\langle T_i \rangle_{Y1n}$ keV and a density of 1.5 g/cc (obtained from a typical best-fit simulation, as discussed below). Fig. 1 also illustrates that $\rho R_{hot,2p}{}^{expl}$ and $\rho R_{hot,2n}{}^{expl}$ are larger for implosions with lower (~12 kJ) on-target laser energy (open squares) than for implosions with full (~23 kJ) laser energy (closed squares). This could be explained by a larger amount of glass shell being ablated away in full energy implosions, resulting in less material to drive the fuel inward.[32,33] (Fig. A.1). In addition, these values of $\rho R_{hot}{}^{expl}$ from D_2 implosions with full laser energy show reasonable agreement with values from similar thin-glass shell DT implosions,[34,12] for which the knock-on method[35] was used to determine the ρR_{hot}.

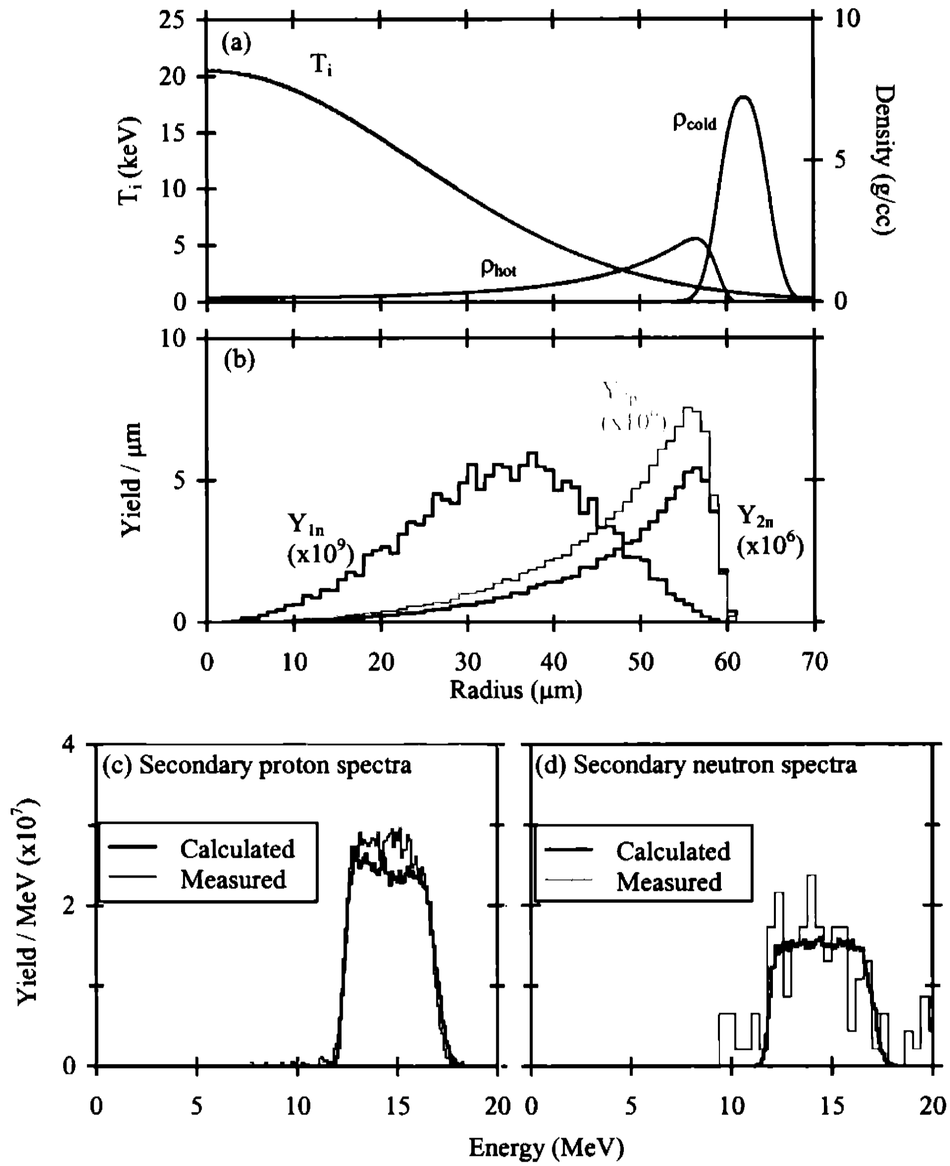

FIG. 5. Parameters from the best-fit Monte-Carlo simulation of shot 30981 (3.1 μm SiO_2 shell filled with 14.7 atm D_2). (a) $T_i(r)$ and $\rho(r)$. Fuel mass is fully conserved, while 11 % of the shell mass remains. (b) Radial distributions of the birth positions of primary and secondary particles indicate that secondary protons and neutrons are produced in a virtually identical region of the capsule. (c) Measured and simulated secondary-proton and (d) secondary-neutron spectra. Note that the shape and width of the simulated proton spectrum are very similar to those of the measured spectrum, even though these were not part of the fitting procedure. The difference in calculated and measured secondary yields are within the measurement uncertainties. Measured and simulated values of implosion characteristics are summarized in Table I. Fig. A.3 indicates how the radial profiles of T_i and ρ can change without changing the quality of the fit to the data too much.

For implosion 30981, which involved a 3.1 μm glass shell filled with 14.7 atm of D_2 gas, Fig. 5a shows simulated density and temperature profiles from the best-fit simulation. Fig. 5b shows radial distributions of the primary and secondary particle birth positions; secondary protons and neutrons are produced in virtually identical regions of the capsule. In addition, a high plasma temperature and a low ρR_{hot} result in similar values of ρR_{hot}^{siml} inferred from the simulated secondary yields. Values of ρR_{hot}^{siml} are inferred using the hot-spot model and assuming a plasma temperature of $\langle T_i \rangle_{Y1n}$ keV and a plasma density of 1.5 g/cc (obtained from simulation). In addition, values of ρR_{hot}^{siml} agree with ρR_{hot}^{int} obtained from the fuel density profile shown in Fig. 5a; this indicates that the small amount of fuel-shell mix in this type of implosion does not have much impact on the accuracy of the simple model. Results of the simulation along with measured data are summarized in Table I.

Simulated secondary spectra are in good agreement with measured spectra as shown in Figs. 5c and 5d. The measured secondary proton spectrum is an average of five spectra obtained simultaneously at different angles from implosion 30981.

Table I. Measured and simulated values of yields and ρR for OMEGA implosion 30981. Experimental data were fitted by adjusting $\rho(r)$ and $T_i(r)$. Total χ^2 along with parameters specifying the cold (SiO_2) temperature and density Gaussian profiles [peak temperature (T_{i0}), 1/e radius (T_{iw}), power of the exponent (T_{ip}), peak density radius (S_{r0}), 1/e radius (S_w), and power of the exponent (S_p)] are also listed. $\rho R_{cold} = \int \rho_{cold} dr$, integrated radially over the SiO_2 shell region, and $\rho R_{hot} = \int \rho_D dr$ integrated radially over the hot-fuel region of the simulated profiles. Values of $\rho R_{hot,\ 2n}$ and $\rho R_{hot,\ 2p}$ were deduced using measured (left column) and simulated (right column) yield ratios assuming a 1.5 +/- 1 g/cc (obtained from Fig. 5a) D plasma at $\langle T_i \rangle_{Y1n}$ +/- 0.5 keV.

Shot 30981

	Measured	Simulated
Y_{1n}	(1.5 +/- 0.15) E+11	(1.5 +0.23 –0.18) E+11
Y_{2n}/Y_{1n}	(5.1 +/- 0.98) E-4	(5.1 +1.1 –0.57) E-4
Y_{2p}/Y_{1n}	(7.9 +/- 1.1) E-4	(7.5 +1.0 –0.96) E-4
$\langle E_{2p} \rangle$ (MeV)	14.47 +/- 0.1	14.64 +0.14 –0.16
$\langle T_i \rangle_{Y1n}$ (keV)	8.2 +/- 0.5	8.2 +0.7 –0.5
χ^2	...	0.1
T_{i0} (keV)	...	20.5 +2.5 –10
T_{iw} (μm)	...	34 +14 –4
T_{ip}	...	2 +5 –0
S_{r0} (μm)	...	62 +6 –10
S_w (μm)	...	3.5 +3 –3.3
S_p	...	2.5 +≥7.5 –2
ρR_{cold} (mg/cm^2)	...	4.5 +4.3 –4.2
ρR_{hot} (mg/cm^2)	...	3.7 +0.8 –0.4
$\rho R_{hot,2n}$ (mg/cm^2)	4.6 +0.9 – 1.2	4.6 +1.0 –0.6
$\rho R_{hot,2p}$ (mg/cm^2)	4.3 +0.6 – 0.8	4.1 +/- 0.5

B. Medium areal density implosions

Correctly inferring the value of ρR_{hot} is more difficult for implosions of capsules with thick plastic shells because Y_{2p} reaches saturation when ρR_{hot} is sufficiently large, and Y_{2n} is enhanced in the presence of increased fuel-shell mix. The triangles in Fig. 1 show that the values of $\rho R_{hot,2p}^{expl}$ are often smaller than values of $\rho R_{hot,2n}^{expl}$, as previously reported in Ref. 12. Values of $\rho R_{hot,2p}^{expl}$ and $\rho R_{hot,2n}^{expl}$ are inferred assuming a temperature of $<T_i>_{Y1n}$ keV and a D plasma with a density of 2 g/cc.

Fig. 6a shows the temperature and density profiles that result in the best fit to the measured data for implosion 27443 (19.4 μm plastic shell filled with 15 atm of D_2 gas), and Fig. 6b shows the resulting radial distributions of primary and secondary particle birth positions. About 32 % of the initial CH mass remains, and ~ 1.3 μm of the initial CH layer has mixed into the fuel (which is similar to the amount of mix reported in Refs. 20-22.[36] The ^3He are ranged out before traversing the entire fuel region. Fig. 6b also illustrates an enhancement of Y_{2n} by fuel-shell mix; the increased energy loss of T per unit ρR_{hot}, due to the cooler, dense shell material, results in an enhanced DT fusion cross section (Fig. 3), which causes Y_{2n}/Y_{1n} to overestimate ρR_{hot}^{int}. In addition, Y_{2n}/Y_{1n} is more sensitive to temperature in this ρR_{hot} range; using $<T_i>_{Y1n}$, which is always higher than $<T_i>_{Y2n}$, results in a larger inferred value of ρR_{hot}.

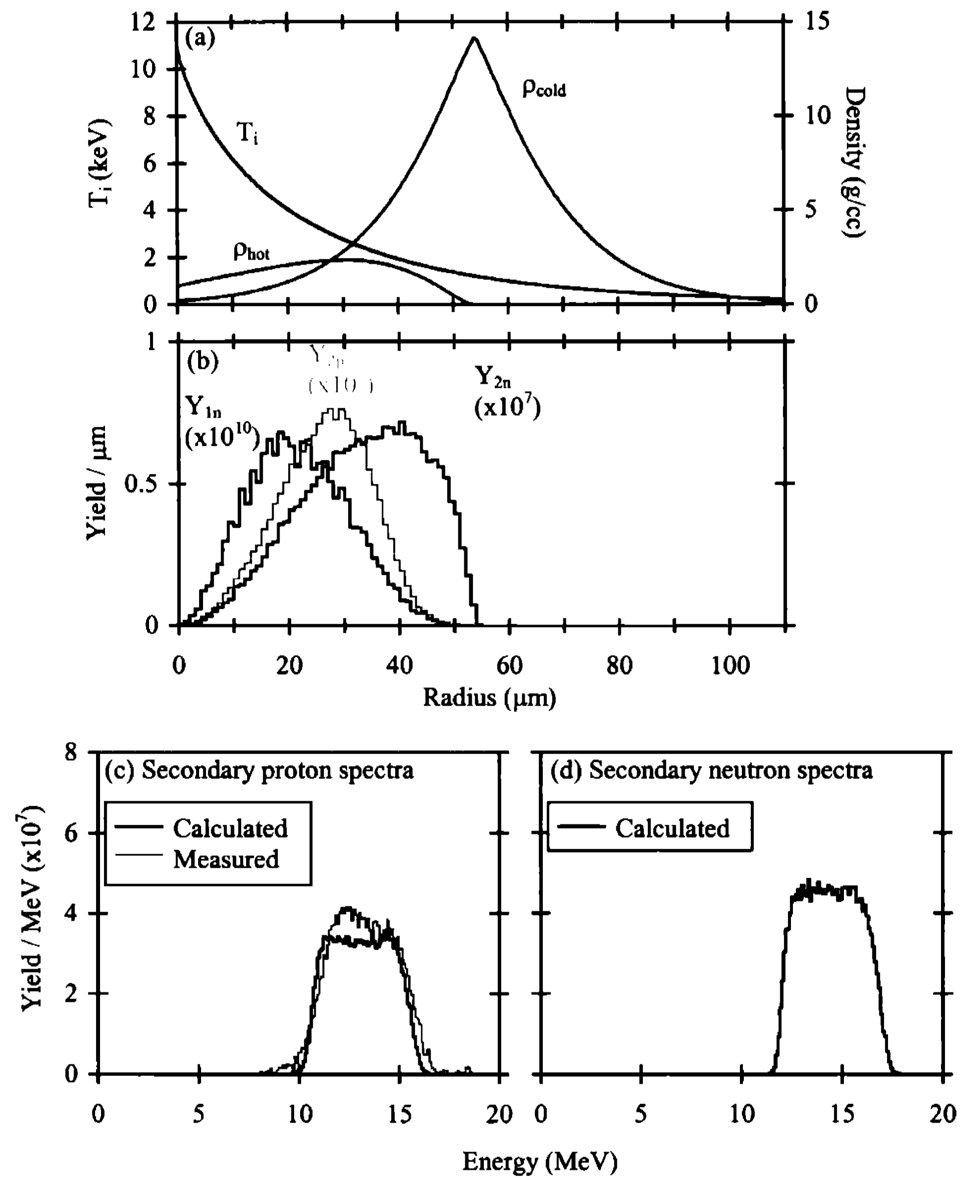

FIG. 6. Best-fit parameters from the Monte-Carlo simulation for shot 27443, which involved a 19.4 µm CH shell filled with 15 atm D_2. (a) $T_i(r)$ and $\rho(r)$. Fuel mass is fully conserved, while 32 % of the shell mass remains. (b) Radial distributions of the birth positions of primary and secondary particles show that secondary proton production is diminished, while secondary neutron production is enhanced in the region of significant fuel-shell mix. This causes secondary protons to underestimate, and secondary neutrons to overestimate the actual value of ρR_{hot}. (c) Measured and simulated secondary proton spectra are compared, and (d) simulated secondary neutron spectrum is shown. The secondary proton spectra show more energy downshift, and the width of the secondary spectra are slightly narrower, than the low ρR_{hot} case because the average primary particle energy is smaller at the time of secondary reaction. Experimental and simulated values of implosion characteristics are listed in Table II, while other fits are illustrated in Fig. A.4.

Simulated yields and additional parameters characterizing the implosion are summarized and compared with measurements in Table II. This table shows that the values of ρR_{hot}^{siml} implied by secondary protons and neutrons are smaller and larger than the value of ρR_{hot}^{int}, respectively. The hot-spot model was used to obtain values of ρR_{hot} using $\langle T_i \rangle_{Y1n}$ keV for the temperature and assuming the density of the D plasma was 2 g/cc.

Table II. Measured and calculated values of implosion characteristics for OMEGA implosion 27443. Values ρR_{hot} were calculated assuming a 2 +/- 1 g/cc D plasma at $\langle T_i \rangle_{Y1n}$ +/- 0.5 keV. Results from simulation (right column) indicate that the $\rho R_{hot,2p}$ underestimates and $\rho R_{hot,2n}$ overestimates the actual value.

Shot 27443	Measured	Simulated
Y_{1n}	(1.5 +/- 0.15) E+11	(1.6 +0.1 –0.25) E+11
Y_{2n}/Y_{1n}	(1.5 +/- 0.24) E-3	(1.4 +0.16 –0.12) E-3
Y_{2p}/Y_{1n}	(1.0 +/- 0.14) E-3	(1.0 +0.1 –0.15) E-3
$\langle E_{2p} \rangle$ (MeV)	13.1 +/- 0.1	13.07 +0.1 –0.11
$\langle T_i \rangle_{Y1n}$ (keV)	4.1 +/- 0.5	4.1 +0.2 –0.4
χ^2	...	0.5
T_{i0} (keV)	...	11 +0 –5.5
T_{iw} (μm)	...	20 +18 -0
T_{ip}	...	0.8 +1.2 -0
S_{r0} (μm)	...	54 +/- 2
S_w (μm)	...	16 +2 –6
S_p	...	1.2 +0 –0.2
ρR_{cold} (mg/cm^2)	...	42.3+3.9 –2.1
ρR_{hot} (mg/cm^2)	...	8.9 +1 –0.4
$\rho R_{hot,2n}$ (mg/cm^2)	12.8 +/- 1.9	11.6 +1.2 -1
$\rho R_{hot,2p}$ (mg/cm^2)	5.0 +/- 0.7	5.2 +0.5 –0.7

The simulated secondary proton spectrum is compared with the measured spectrum in Fig. 6c. The measured secondary proton spectrum is an average of three spectra simultaneously obtained at different angles from implosion 27443, and shows more downshift than spectra from the low ρR_{hot} implosions. The widths of the secondary proton and neutron spectra (Fig. 6d) are slightly narrower than in the previous case because the average energy of the primary particle, at the time it undergoes secondary fusion, is smaller.[12]

C. Cryogenic implosions

For cryogenic implosions, the interpretation of inferred values of ρR_{hot} is even more subtle, since there is a high-temperature, low-density fuel region and a low-temperature, high-density fuel region. If most of the secondary particles are produced only in the hot-fuel region, then Y_2/Y_{1n} can be used to infer ρR_{hot}. On the other hand, if secondary particles are mainly produced in the inner part of the cold fuel region, the inferred ρR is larger than ρR_{hot}, but smaller than ρR_{total}. (Even the more penetrating T cannot traverse the entire cold fuel region since the range of T in a 8 g/cc, 1 keV D plasma is ~ 15 mg/cm^2, and we usually calculate $\rho R_{total} > 40$ mg/cm^2 from the downshift of the average secondary proton energy for cryogenic implosions). Fig. 1 shows that values of ρR_{hot} implied by measured Y_{2n}/Y_{1n} are always larger than values from measured Y_{2p}/Y_{1n} for those implosions (values were inferred assuming a $\langle T_i \rangle_{Y1n}$ keV, 3 g/cc D plasma).

Radial profiles of temperature and density calculated for implosion 28900 (89-μm D_2 ice layer inside of 5.1-μm CH shell) are shown in Fig. 7a, and simulated and measured spectra are shown in Figs. 7c and 7d. As indicated in Fig. 7d, the secondary-neutron spectrum is much narrower than the secondary-neutron spectra from Figs. 5d and 6d (Fig. A.2) because the primary T are, on average, less energetic when they fuse with thermal D.[12] Measurements of secondary-neutron spectra from more recent cryogenic implosions also show the same characteristics.

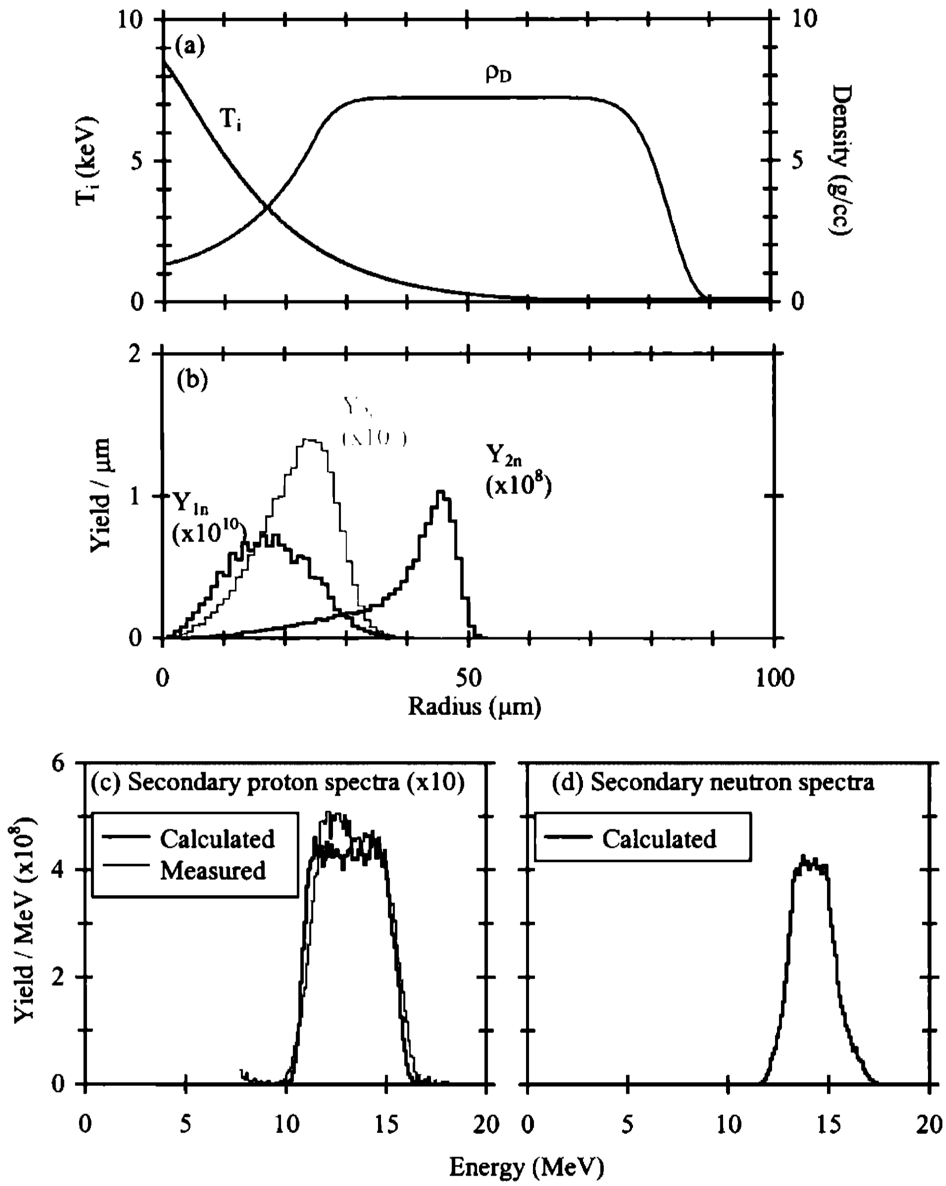

FIG. 7. (a) Simulated profile of shot 28900 (cryogenic capsule with a 5.1 μm CD shell and 89 μm D_2 ice layer) which gives the best fit to the measurement. 31 % of the total mass remains. (b) Radial distributions of the birth points of primary and secondary particles show that most of the secondary protons are produced in the hot-fuel region, while secondary neutrons are mainly produced in the cold fuel region. (c) Measured and simulated secondary proton spectra. (d) Simulated secondary neutron spectrum is narrower than the spectra in Figs. 5d and 6d because primary T are less energetic at the time they undergo secondary reactions; ρR of cold fuel is large enough to stop primary T (Fig. 7.b), and the cross section increases as T loses energy (Fig. 3a). Important implosion characteristics are summarized in Table III, while other fits are illustrated in Fig. A.5.

The radial distributions of the primary and secondary birth positions shown in Fig. 7b indicate that secondary protons and neutrons are born mainly in the hot and cold fuel regions, respectively. Therefore, the ρR obtained from secondary protons gives an estimate of ρR_{hot}, while the secondary neutron yield provides a lower limit on ρR_{total}. In this type of implosion, effects of mix or exchange of hot and cold fuel play significant roles in determining the radial distribution of secondary birth positions.

Simulated values of yields and other important implosion characteristics are compared with experimental results in Table III. The secondary-neutron, hot-spot-model-inferred ρR^{siml} is close to $\rho R_{total}{}^{int}$, but this does not mean that the hot-spot model describes the implosion accurately. The agreement is an accidental consequence of using the wrong temperature, $\langle T_i \rangle_{Y1n}$, which samples the hotter central region rather than the cooler fuel region where most of the secondary neutrons are produced.

This implosion has also been analyzed using a combination of x-ray and neutron measurements, without the use of secondary proton data. These results are discussed in Ref. 37. While the best-fit profiles were somewhat different, they agree within the uncertainties of the two simulation techniques.

Table III. Measured and calculated values of implosion characteristics for OMEGA implosion 28900. $\rho R_{total} = \int \rho_D dr$, integrated radially over the entire simulated profiles. ρR_{hot} is defined as the ρR that includes 90% of primary production. Values of ρR_{hot} were calculated assuming a 3.0 +/- 1.5 g/cc D plasma at $\langle T_i \rangle_{Y1n}$ +/- 0.5 keV. Results from the simulation (right column) suggest that value of $\rho R_{hot,2p}$ provides a good estimate of ρR_{hot}. Secondary neutron implied ρR_{hot} is similar to ρR_{total}, but this is because the value of the temperature used to infer ρR_{hot} is too large. If the temperature of the cold fuel region (1 keV instead of 3.6 keV) were used, a much smaller and physical value of ρR_{hot} would be implied.

Shot 28900	Measured	Simulated
Y_{1n}	(1.2 +/- 0.12) E+11	(1.3 +0.12 –0.14) E+11
Y_{2n}/Y_{1n}	(9.4 +/- 1.4) E-3	(9.1 +1.0 –1.1) E-3
Y_{2p}/Y_{1n}	(1.8 +/- 0.26) E-3	(1.6 +0.0 –0.2) E-3
$\langle E_{2p} \rangle$ (MeV)	13.31 +/- 0.10	13.28 +0.15 –0.11
$\langle T_i \rangle_{Y1n}$ (keV)	3.6 +/- 0.5	3.5 +0.6 -0.3
χ^2	...	0.6
T_{i0} (keV)	...	8.5 +9.5 –2.5
T_{iw} (μm)	...	18 +10 –8
T_{ip}	...	1.2 +0.6 -0.4
S_{r0} (μm)	...	52 +22 –2
S_w (μm)	...	32 +16 –12
S_p	...	9 +≥1 –7.5
ρR_{total} (mg/cm^2)	...	48.2 +3.2 -6.0
ρR_{hot} (mg/cm^2)	...	7.9 +0.2 –1.7
$\rho R_{hot,2n}$ (mg/cm^2)	49.8 +5.0 –6.9	48.0 +4.9 –4.0
$\rho R_{hot,2p}$ (mg/cm^2)	9.3 +1.9 –1.5	7.8 +0.5 –0.6

VI. Conclusions

The hot-spot and uniform models have been used to infer the areal density of the hot-fuel region (ρR_{hot}) of D_2 implosions, but disagreements between the values of ρR_{hot} inferred from secondary proton and neutron yields have often been observed, indicating limitations in these models. Results from direct-drive experiments at the OMEGA laser system and Monte-Carlo simulations provided a deeper understanding of the relationship between ρR, the capsule structure, and secondary particle production. Experiments show that values of ρR_{hot} inferred from the ratios of secondary proton and neutron to primary neutron yields (Y_{2p}/Y_{1n} and Y_{2n}/Y_{1n}) using the hot-spot model agree well for low ρR_{hot} implosions (thin-glass shell capsules), and simulations indicate that they give a good estimate of the actual value of ρR_{hot}. The results from implosions of D_2-filled thin-glass shells also show reasonably good agreement with results from implosions of similar capsules filled with DT gas. For thick-plastic-shell capsule implosions, where the ρR_{hot} of an implosion becomes sufficiently large, Y_{2p}/Y_{1n} underestimates ρR_{hot} since the primary ^3He are ranged out before sampling the entire hot-fuel region. In addition, fuel-shell mix increases the rate of energy loss of ^3He and causes Y_{2p}/Y_{1n} to further underestimate ρR_{hot}. The fuel-shell mix also causes Y_{2n}/Y_{1n} to overestimate ρR_{hot} by slowing down the primary T, thereby increasing the secondary DT fusion reaction cross section. As a result, values of ρR_{hot} for medium ρR_{hot} capsules inferred from Y_{2p}/Y_{1n} and Y_{2n}/Y_{1n} using the hot-spot model should be interpreted as estimates of the lower and upper limits on the actual ρR_{hot}, respectively. For cryogenic capsules, secondary protons are produced mainly in the hot-fuel region, and the proton-implied value of ρR provides a good estimate of the hot-fuel ρR. In contrast, secondary neutrons are mostly produced in the inner part of the cold fuel region, and the neutron-implied ρR gives a lower limit on the total ρR when calculated correctly using the secondary-neutron-birth-point average temperature and density. Naive use of the simple hot-spot or uniform model, with a burn-averaged temperature, often results in inaccurate inference of ρR_{hot}. More thorough analysis, such as the use of complete data sets and simulations for determining the secondary birth positions and the effects of mix, as presented herein, or the use of detailed analysis of secondary neutron spectra both from experiments and simulations[10], is required in order to obtain a realistic estimate of ρR_{hot}.

Acknowledgement

This work described here was performed in part at the LLE National Laser Users' Facility (NLUF), and was supported in part by the US DoE (grant DE-FG03-03SF22691), US DoE DP/NNSA (Cooperative Agreement DE-FG03-03NA00058), LLE (subcontract 412160-001G), and LLNL (subcontract B504974).

Appendix A: Additional figures

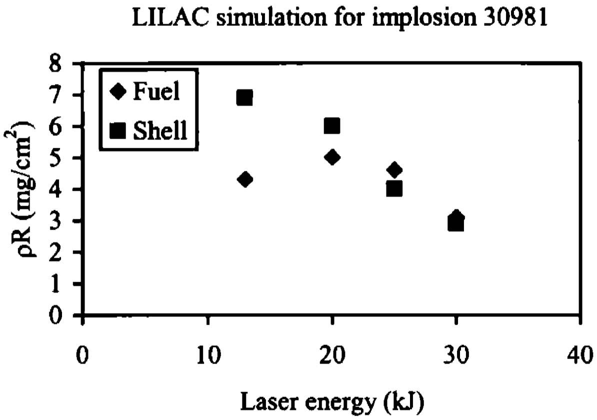

FIG. A.1. 1D clean LILAC simulations for low ρR implosion 30981 indicate hot-fuel ρR starts to decrease as the capsule is significantly overdriven. This trend agrees with measurements where ρR_{hot} are lower for full-laser energy (~23 kJ) driven thin-glass shell capusles than for low laser energy (~12 kJ) driven capsules (Fig. 1).

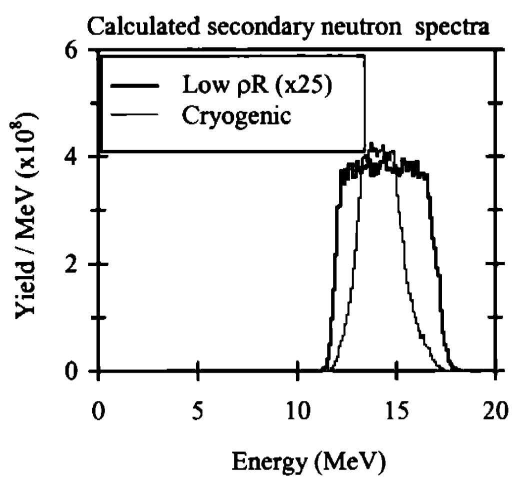

FIG. A.2. The simulated secondary neutron spectrum is narrower than the spectra in Figs. 5d and 6d because the primary T are less energetic at the time they undergo secondary reactions; ρR of cold fuel is large enough to stop primary T (Fig. 7.b), and the cross section increases as T loses energy (Fig. 3a). Note that detailed analysis of secondary neutron spectra was used to study areal density in Ref. 10.

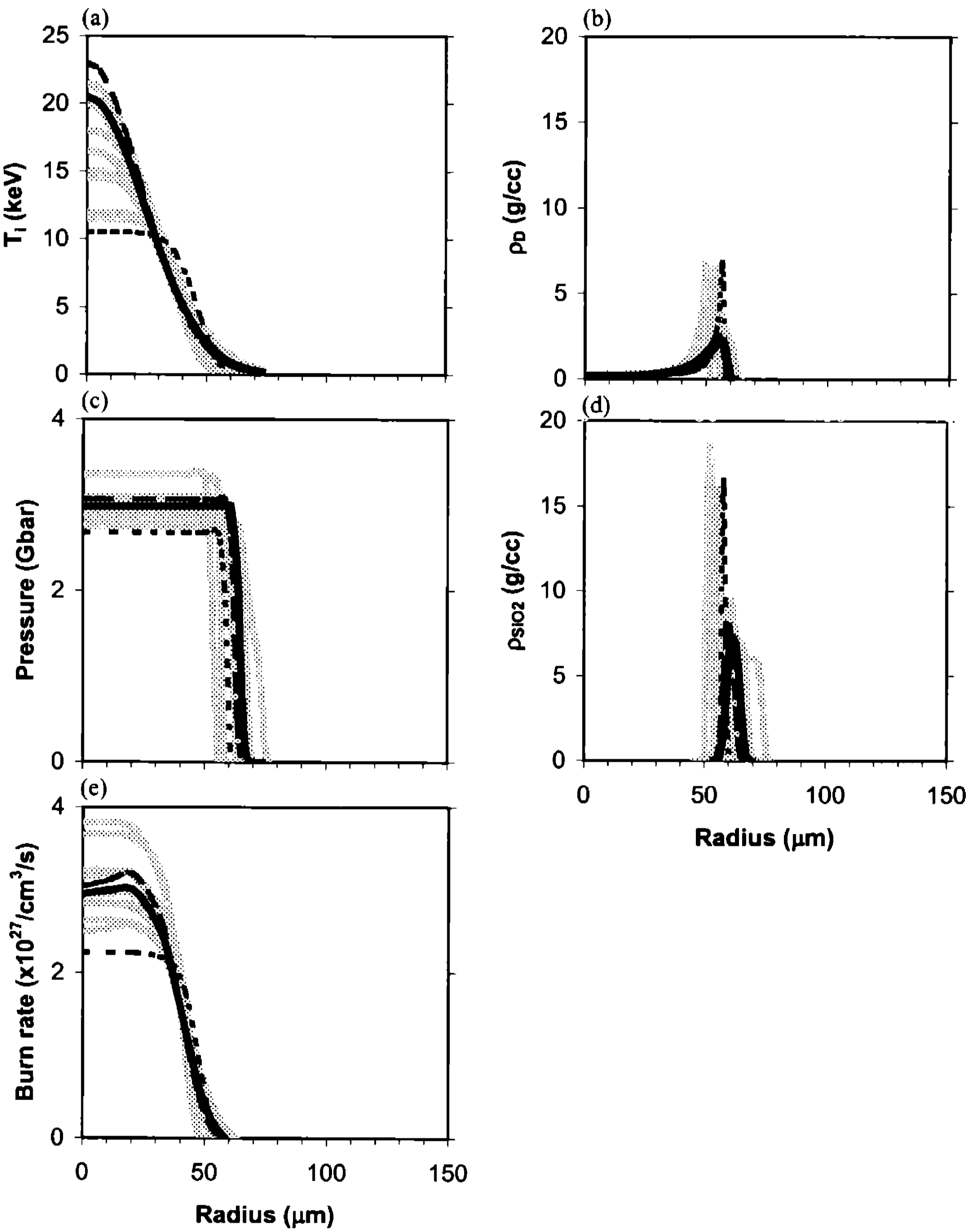

FIG. A.3 Samples of temperature, density, pressure, and burn profiles which produced fits to the data which were not as good as the best fit for implosion 30981. Bold lines represent the best-fit profiles; dashed and dotted lines represent the fits having the highest and lowest peak temperature, respectively, in the group of fits for which the total χ^2 is within one of its minimum value.

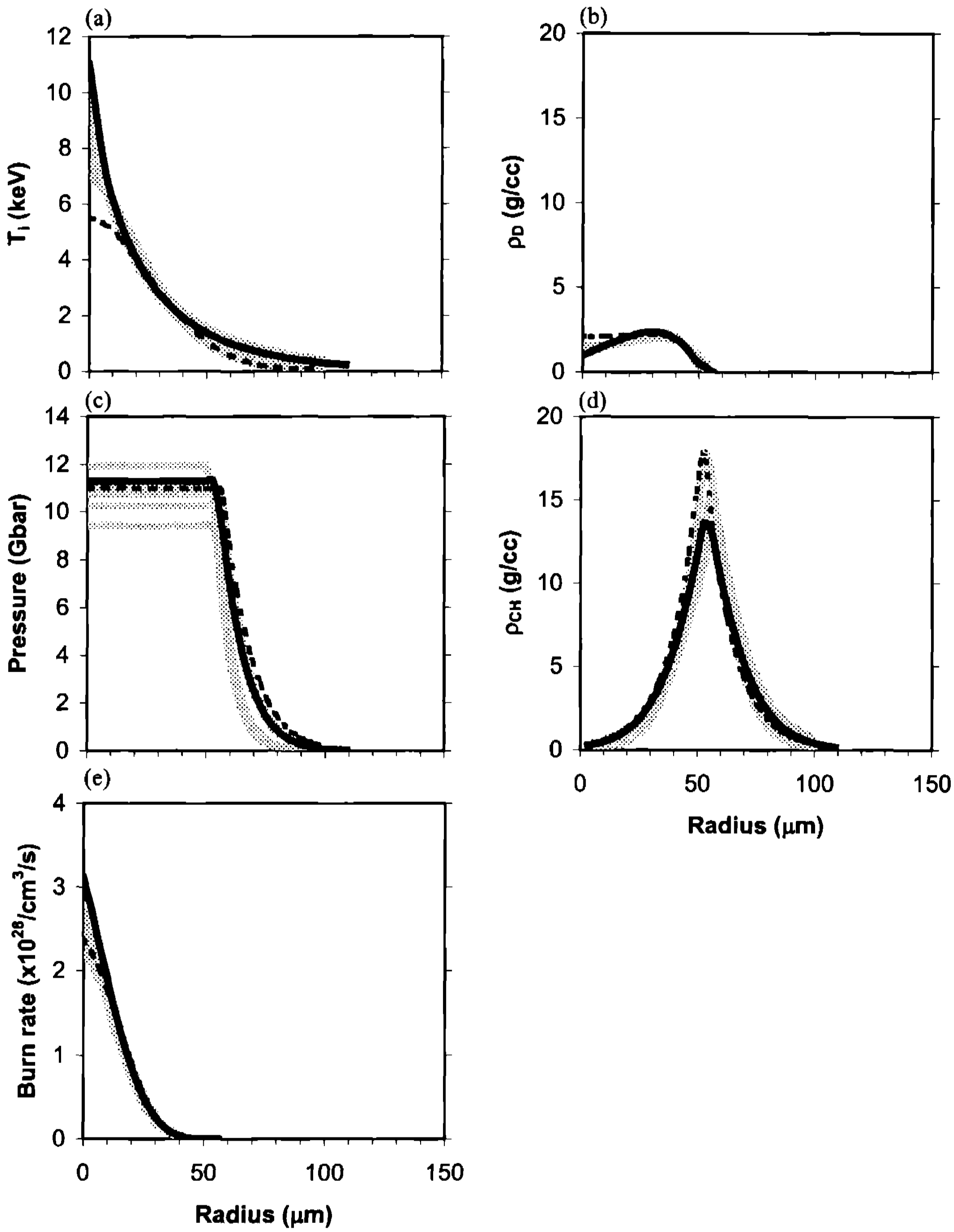

FIG. A.4 Samples of temperature, density, pressure, and burn profiles which produced fits to the data which were not as good as the best fit for implosion 27443 (as described in the caption of Figure A.3). The width of the burn profile is narrower than the width for implosion 30981, indicating more compression.

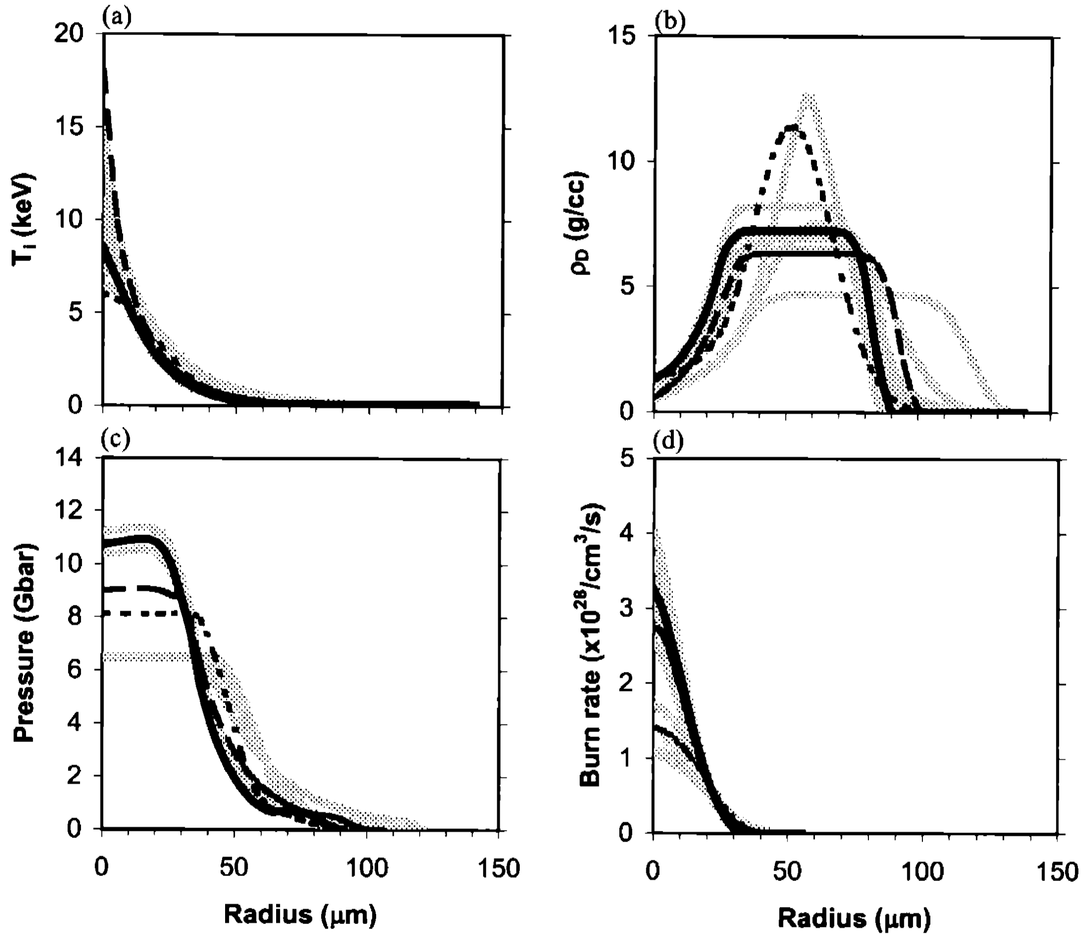

FIG. A.5 Samples of temperature, density, pressure, and burn profiles which produced fits to the data which were not as good as the best fit for implosion 28900 (as described in the caption of Figure A.3). The width of the burn profile is narrower than the width for implosion 30981, indicating more compression.

References

[1]S. W. Haan, S. Pollanine, J. D. Lindl *et al.*, Phys. Plasmas **2**, 2480 (1995).

[2]J. D. Lindl, R. L. McCrory, and E. M. Campbell, Phys. Today **45**, 32 (1992).

[3]J. D. Lindl, Phys. Plasmas **2**, 3933 (1995).

[4]H. D. Campbell and F. H. Southworth, in *Proceedings of the First Topical Meeting on the Technology of Controlled Nuclear Fusion* (American Nuclear Society, LaGrange Park, IL, 1974), p. 75.

[5]E. G. Gamalii, S. Yu, Gus'kov, O. N. Krokhin, and V. B. Rusanov, JETP Lett. **21**, 70 (1975).

[6]S. Skupsky and S. Kacenjar, J. Appl. Phys. **52**, 2608 (1981).

[7]T. E. Blue and D. B. Harris, Nucl. Sci. Eng. **77**, 463 (1981).

[8]T. E. Blue, J. W. Blue, J. S. Durham, D. B. Harris, A. S. Hnesh, and J. J. Reyes, J. Appl. Phys. **54**, 615 (1983).

[9]H. Azechi, N. Miyanaga, R. O. Stapf *et al.*, Appl. Phys. Lett. **49**, 555 (1986).

[10]M. D. Cable and S. P. Hatchett, J. Appl. Phys. **62**, 2233 (1987).

[11]H. Azechi, M. D. Cable, and R O. Stapf, Laser Part. Beams **9**, 119 (1991).

[12]F. H. Séguin, C. K. Li, J. A. Frenje *et al.*, Phys. Plasmas **9**, 2725 (2002).

[13]Peter Amendt, R. E. Turner, and O. L. Landen, Phys. Rev. Lett. **89**, 165001 (2002).

[14]T. C. Sangster, J. A. Delettrez, R. Epstein *et al.*, Phys. Plasmas **10**, 1937 (2003).

[15]C. Stoeckl, C. Chiritescu, J. A. Delettrez *et al.*, Phys. Plasmas **9**, 2195 (2002).

[16]R. E. Turner, P. A. Amendt, O. L. Landen *et al.*, Bull. Am. Phys. Soc. 47, 328 (2002).

[17]T. R. Boehly, D. L. Brown, R. S. Craxton *et al.*, Opt. Commun. **133**, 495 (1997).

[18]S. Glasstone and R. H. Lovberg, *Controlled Thermonuclear Reactions: An Introduction to Theory and Experiment* (Van Nostrand, Princeton, NJ, 1960).

[19]C. K. Li and R. D. Petrasso, Phys. Rev. Lett. **70,** 3059 (1993).

[20]P. B. Radha, J. Delettrez, R. Epstein *et al.*, Phys. Plasmas **9,** 2208 (2002).

[21]C. K. Li, F. H. Séguin, J. A. Frenje *et al.*, Phys. Rev. Lett. **89,** 165002 (2002).

[22]S. P. Regan, J. A. Delettrez, F. J. Marshall *et al.*, Phys. Rev. Lett. **89,** 085003 (2002).

[23]Y. Lin, T. J. Kessler, and G. N. Lawrence, Opt. Lett. **20**, 764 (1995).

[24]T. R. Boehly, V. A. Smalyuk, D. D. Meyerhofer *et al.*, J. Appl. Phys. **85**, 3444 (1999).

[25]S. Skupsky, R. W. Short, T. Kessler *et al.*, J. Appl. Phys. **66**, 3456 (1989).

[26]Short laser pulses (< 1 ns) imploding thin-glass shell capsules prevent significant nuclear production while the laser is on. This is important if ρR_{total} is to be studied, because the capsule can be charged to a significant potential relative to the target chamber wall due to laser-plasma interactions. The potential can cause an upshift of measured proton energies,[35,38,39] making it difficult to determine how much energy the protons lost while leaving the capsule (necessary for calculating ρR_{total}). The potential decays away rapidly after the laser is turned off, so it does not affect measurements of protons from implosions in which the nuclear burn occurs after the pulse (such as those involving thick-plastic-shell or cryogenic capsules[35]). This affects only the study of ρR_{total}; measurements of yields are unaffected by capsule potentials.

[27]F. H. Séguin, J. A. Frenje, C. K. Li *et al.*, Rev. Sci. Instrum. **74,** 975 (2003).

[28]M. A. Russotto and R. L. Kremens, Rev. Sci. Instrum. **61,** 3125 (1990).

[29]R. A. Lerche, D. W. Phillion, and G. L. Tietbohl, Rev. Sci. Instrum. **66,** 933 (1995).

[30]V. Yu. Glebov, C. Stoeckl, S. Roberts *et al.*, Bull. Am. Phys. Soc. 48, 342 (2003).

[31]Primary-neutron-yield-weighted-average ion temperature is calculated by two methods, each yielding a virtually identical temperature. First, the product of the temperature and the primary neutron birth rate per unit length at each radius is integrated and divided by the primary neutron

yield. Second, the primary neutron spectrum is calculated, and the width of the spectrum was used to obtain an ion temperature.

[32]J. D. Lindl, *Inertial Confinement Fusion* (Springer-Verlag, New York, 1998).

[33]M. D. Rosen and J. H. Nuckolls, Phys. Fluids 22, 1393 (1979).

[34]M. J. Canavan, *et al.*, to be submitted to Rev. Sci. Instrum. (2004); herein the laser energy was ~30 kJ for these DT implosions.

[35]C. K. Li, F. H. Séguin, D. G. Hicks *et al.*, Phys. Plasmas **8**, 4902 (2001).

[36]Radha *et al.*,[20] Li *et al.*,[21] and Regan *et al.*[22] reported ~ 1 μm, ~ 0.5 μm, and ~ 0.4 μm of the initial shell layer mixed into the fuel, respectively.

[37]V. A. Smalyuk, J. A. Dellettrez, S. B. Dumanis *et al.*, "Hot-Core Characterization of the Cryogenic D_2 Target at Peak Neutron Production in Direct-Drive Spherical Implosion," submitted to Phys. Rev. Lett.

[38]D. G. Hicks, C. K. Li, F. H. Séguin *et al.*, Phys. Plasmas **8**, 606 (2001).

[39]D. G. Hicks, C. K. Li, F. H. Séguin *et al.*, Phys. Plasmas **7**, 5106 (2000).

3. An unsolved problem and future work

I. Energy losses of primary particles

For thin-glass capsule implosions, we obtain some primary charged particle spectra in addition to secondary proton spectra, since the imploding capsule does not have enough ρR_{tot} to completely stop primary particles. However, the energy loss of the primary particles (ΔE) is smaller than or comparable to the ΔE of the secondary protons. Calculations according to Ref. 8 predict a larger ΔE for primary particles than secondary protons for temperatures and densities of interest, because their energy is much smaller than that of secondary particles. We held discussions and performed calculations, but, so far, we have not reached a conclusion. Examples of this problem can be seen in spectra from implosions 30981, 30982, and 30983 in Appnedix D.

II. Improvements to the Monte-Carlo program

There are three obvious directions that could be taken in generalizing and improving the analysis procedures described in this thesis. The first involves enhancements of the Monte-Carlo program, the second involves incorporation of additional data constraints into the fit procedures, and the third involves improvements in the rigor of the statistical analysis.

At least two changes could be explored for the Monte-Carlo program. The first is to incorporate asymmetries into capsule structures; this is important because we often have evidence of significant asymmetries in the data sets (see Appendix D). The second is to investigate whether the normalization technique described in Section 2-IV introduces any errors in the shapes of secondary spectra, and whether improvements are worth pursuing in this area.

For comparing simulations with data, use could be made of experimental constraints that were not imposed in the work described here. For example, we made use of the yields and mean energies of secondary protons, but we didn't compare the detailed shapes of the measured and simulated spectra as part of the quantitative goodness-of-fit procedure. In addition, other diagnostic measurements provide relevant information. X-ray data provide additional constraints on temperature and density profiles. The neutron temporal diagnostic, the proton temporal diagnostic, and time-resolved x-ray measurements provide information about time dependence that could be modeled by using the Monte-Carlo program to simulate successive time slices.

Finally, it would be interesting to explore more complete approaches to quantifying the statistical analysis of data-simulation comparisons. One approach would be to use the "bootstrap" method to evaluate goodness of fit and uncertainties in best-fit parameters. A set of artificial data sets is generated from an actual data set. In each artificial data set, each "measurement" is assigned a value gotten by adding to the actual measured number an amount determined randomly from the Gaussian distribution implied by the measurement uncertainty. For each data set, a new set of "best-fit" model parameters is calculated, and the distribution of values of these parameters generated by a large number of "data sets" is used to study the probability distributions of the inferred parameters.

Appendix B: Details of Monte-Carlo code

A Monte-Carlo code was developed to understand the effects of fuel-shell mix and density and temperature profiles on secondary yields, as explained in Section 2-IV. This program produces spectra of primary, secondary, and knock-on particles (fuel and shell ions elastically scattered by DT neutrons) according to density and temperature profiles specified by the user. The profiles are assumed to be static throughout the burn duration and to be spherically symmetric. A flow chart of the code is shown in Figure B.1, and details of the program are explained in the following sections.

B.1 Input parameters

When modeling any real inertial confinement fusion experiment, it is critical to conserve the fuel mass and to know how much shell mass remains. In order to calculate the initial mass, the program prompts the user for the initial capsule conditions (Figures B.2 and B.3). It requires the user to specify the type of gas, fill pressure, shell material, shell thickness, and capsule diameter. In addition, for cryogenic capsules, the user must specify the ice layer thickness. The program calculates the initial mass of the fuel and shell and displays them on the user interface.

There are two ways to specify the burn-averaged density and temperature profiles. In the multi-ramp model, an imploded capsule is modeled by a central sphere and several shells (or zones) surrounding it (Figure B.2). Within each zone, the density of fuel and shell materials and the temperature can be constant or vary linearly. The program requires the user to specify the radius of the sphere and the thickness of the zones, as well as the density and temperature at the center of the sphere and at the inner and outer edges of each zone. Up to eight shells can be used to specify the density and temperature profiles of the implosion.

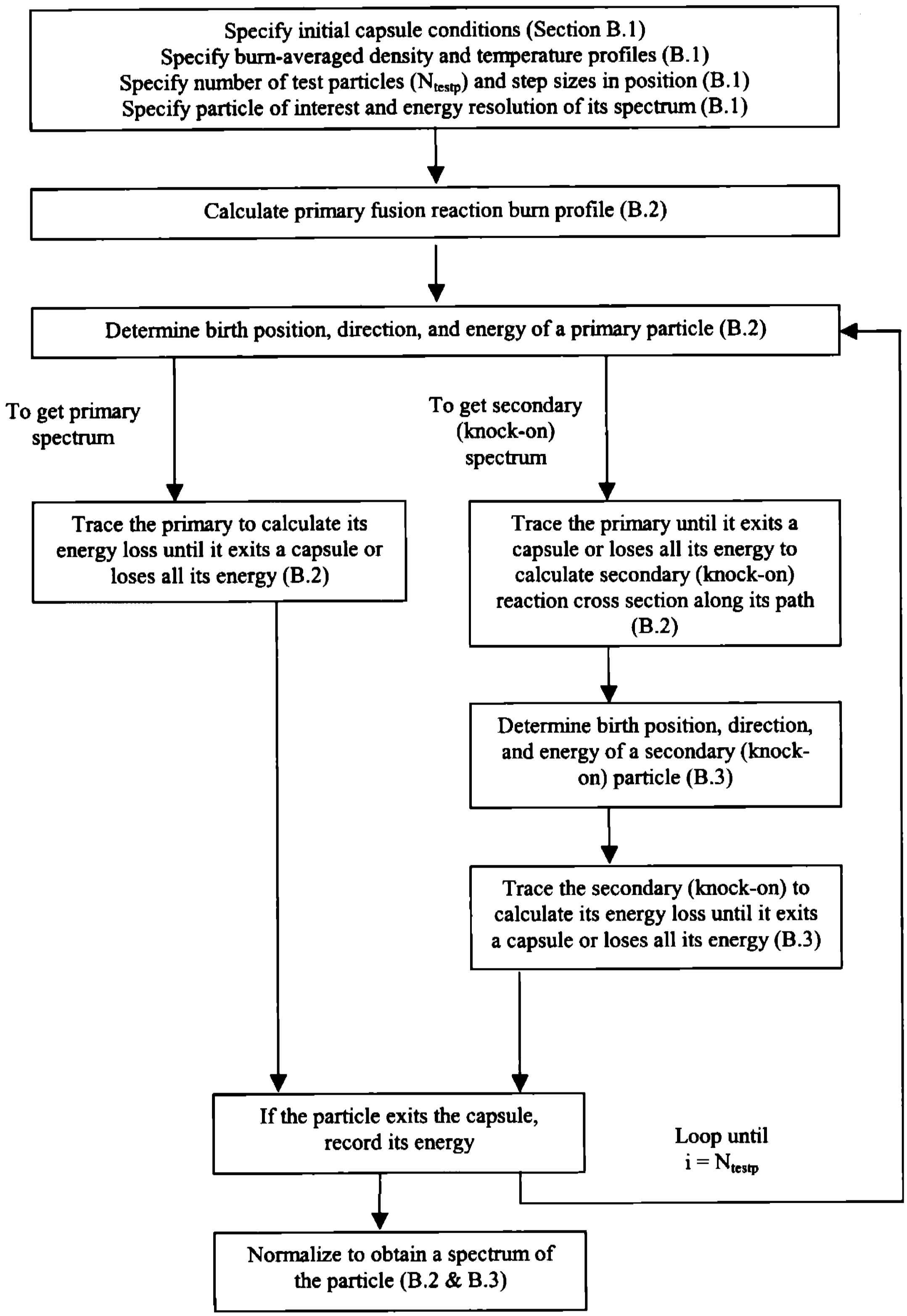

Figure B.1 Flow chart of the Monte-Carlo code

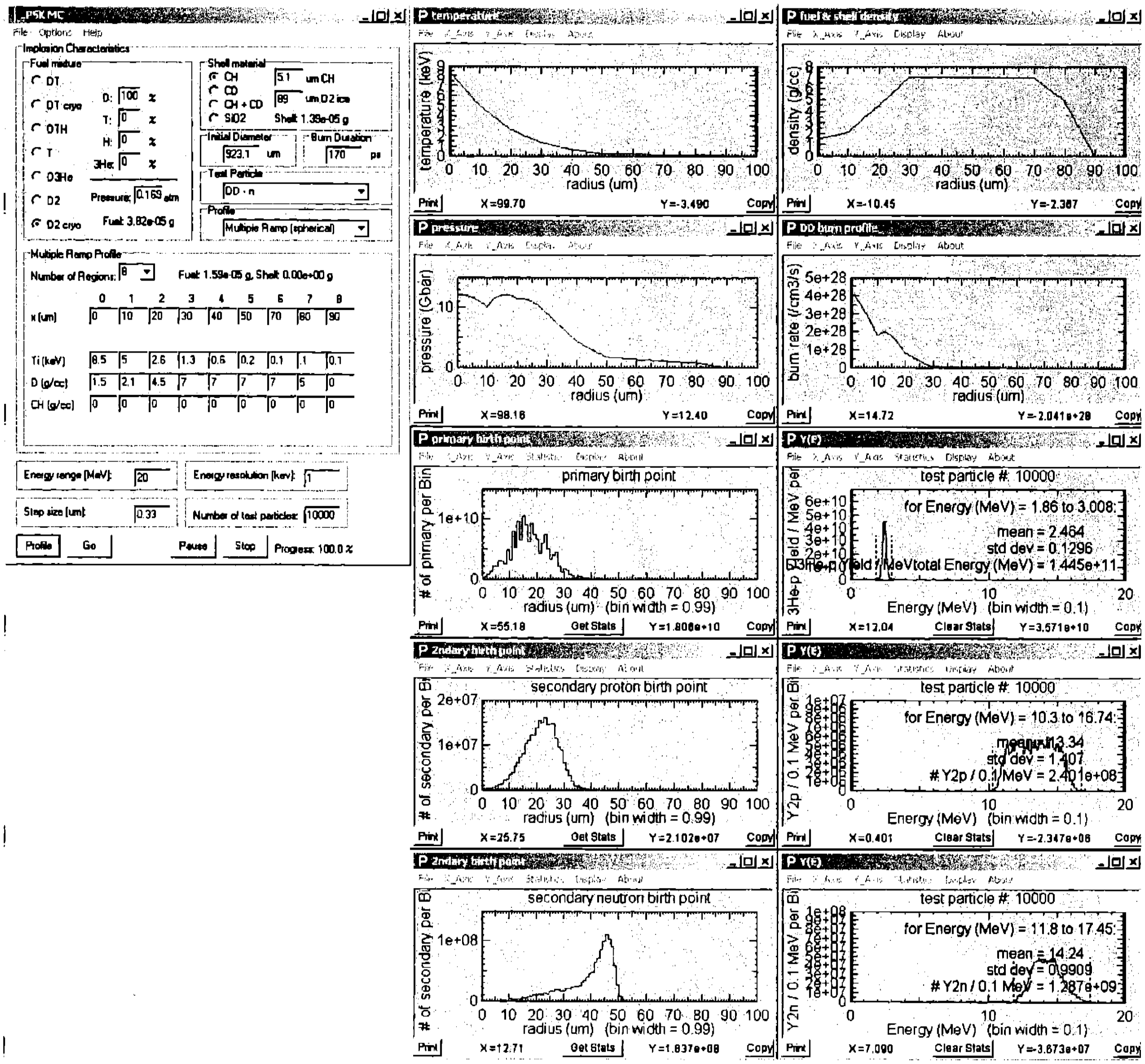

Figure B.2 User interface for the multi-ramp model. The radius of the sphere and the thickness of each zone, as well as the density and temperature at the center of the sphere and at the inner and outer edges of each zone, need to be specified for up to eight zones. The program plots profiles, birth points and spectra next to the user interface.

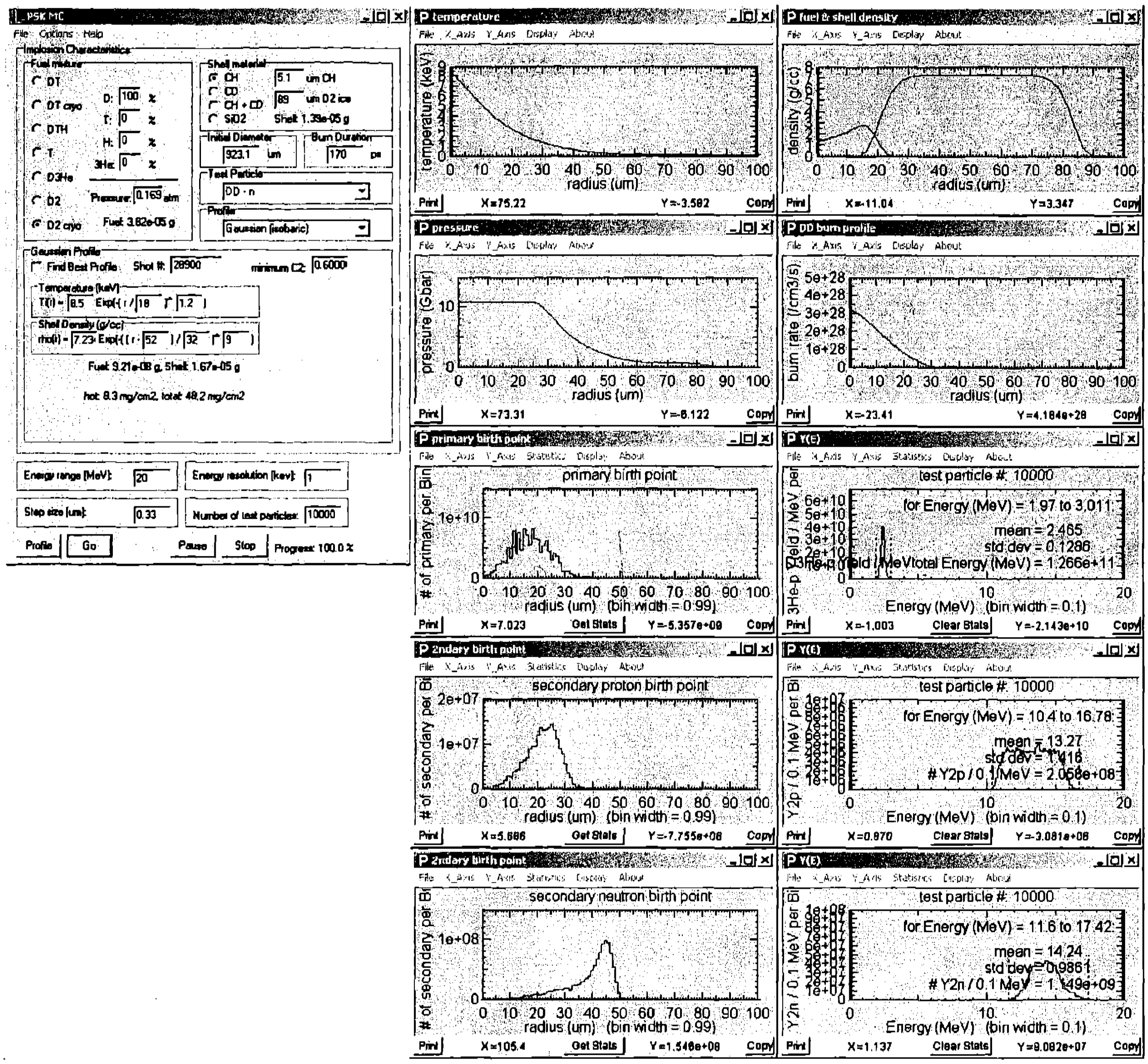

Figure B.3 User interface for the Gaussian model.

In the Gaussian model, the temperature and shell density profiles [$T_i(r)$ and $\rho_{cold}(r)$] are specified using Gaussian functions,

$$T_i(r) = T_{i0} \exp\left[-\left(\frac{r}{\sigma_{Ti}}\right)^{p_{Ti}}\right], \text{ and} \qquad (B.1)$$

$$\rho_{\text{cold}}(\mathrm{r}) = \rho_{\text{c0}} \exp\left[-\left(\frac{\mathrm{r}-\mathrm{r}_{\text{c0}}}{\sigma_{\text{c}}}\right)^{\mathrm{p_c}}\right], \tag{B.2}$$

where T_{i0}, σ_{Ti}, p_{Ti}, r_{c0}, σ_c, and p_c are variables specified by the user (Figure B.3). For cryogenic implosions, the plastic shell surrounding the ice layer is assumed to be ablated completely, and the density of the cold fuel is expressed using $\rho_{cold}(r)$. The pressure within the shell (or cold fuel) is calculated using $T_i(r)$ and $\rho_{cold}(r)$, and the position of peak shell pressure is determined. The density of the hot fuel [$\rho_{hot}(r)$] is calculated, assuming that the hot fuel region (inside the peak shell pressure) is isobaric. To fully conserve the hot fuel mass, ρ_{c0} is adjusted accordingly. Once the hot and cold density and temperature profiles are determined, they are plotted next to the user interface (Figure B.2) along with the pressure profile. The amount of mass remaining in the profile, as well as the ρR, is calculated and shown on the user interface (Figure B.2).

The user selects a fusion product (test particle): primary, secondary, or knock-on. The full-width-half-maximum of the primary neutron production rate (burn width or t_B) is used to calculate the primary yield (Y_1). This value is obtained from the neutron temporal diagnostic (NTD) [9]. Other parameters to be specified by the user include an upper limit on the energy range (E_{max}) and the energy resolution (dE) of the resulting spectrum, the distance between successive calculations (dr), and the number of test particles (N_{testp}). For computational reasons, $N_{testp} \sim 10^4$ particles (instead of $Y_1 > 10^{10}$) is used to obtain a spectrum, which is then normalized to determine the final spectrum.

B.2 Primary particle

The radial burn profile (fusion reaction rate per unit volume) of the primary fusion reaction can be calculated using density and temperature profiles. For a fusion reaction A + B $\rightarrow$ C + D, the burn profile [$R_1(r)$] is given by,

$$R_1(r) = n_A(r) n_B(r) < \sigma v >_{AB} (r) \tag{B.3}$$

where n_A and n_B are number densities of reacting particles A and B, respectively, and $<\sigma v>_{AB}$ is the rate coefficient averaged over the velocity distribution of both species. $<\sigma v>$ is a function of ion temperature and is calculated according to Ref. 5 and shown in Figure 1.1. For the DD fusion reaction, R_1 is given by,

$$R_1(r) = \frac{1}{2} n_D(r)^2 < \sigma v >_{DD} (r) \tag{B.4}$$

Then the primary yield (Y_1) is calculated by integrating R_1 over the volume of the compressed capsule and multiplying by the burn width (t_B),

$$Y_1 = t_B \int R(r)\, dV . \tag{B.5}$$

Since the radial burn profile is effectively the probability of a primary fusion reaction at each radius, the birth position of primary particles (r_{1birth}) is randomly generated using the Monte-Carlo technique: the radial profile is integrated over the radius and normalized to one. Then a random number between zero and one is used to select the radial position of primary fusion reaction. The polar (θ_1) and azimuthal (ϕ_1) angles of a primary birth position as well as the direction of a primary particle ($\vec{v}_1$), which is defined by two angles (θ_{v1} and ϕ_{v1}), are also determined by random numbers, since a primary particle is produced isotropically in the spherically symmetric capsule.

The energy of the primary particle is determined according to Ref. 10, assuming that the velocity of the reacting ions is a three-dimensional Maxwellian distribution of temperature $T_i(r_{1birth})$. The energy distribution of fusion product C is then given by a Gaussian,

$$f(E_c) = \frac{\langle E_c \rangle}{\sqrt{2\pi}\,\sigma_{Ec}} \exp\left[-\frac{(E - \langle E_c \rangle)^2}{2\sigma_{Ec}^{\;2}} \right], \tag{B.6}$$

where $\langle E_c \rangle$ is the mean energy of fusion product C and σ_{Ec} is the standard deviation of the Gaussian. $\langle E_c \rangle$ is given by,

$$\langle E_c \rangle = \frac{1}{2} m_c \langle V^2 \rangle + \frac{m_D}{m_c + m_D} (Q + \langle K \rangle), \tag{B.7}$$

where $\langle V^2 \rangle$ and $\langle K \rangle$ are the center-of-mass velocity and relative kinetic energy of the reacting particles averaged over the Maxwellian distribution and given by,

$$\langle V^2 \rangle = \frac{3T_i}{m_A + m_B}, \tag{B.8}$$

and

$$\langle K \rangle \approx \left(\frac{\pi^2 e^4 m}{2\hbar^2} \right)^{1/3} T_i^{2/3} + \frac{5}{6} T_i, \tag{B.9}$$

where m is the reduced mass of the reacting particles. Q is the nuclear energy release of the reaction. σ_{Ec} is given approximately as,

$$\sigma_{Ec} \approx \frac{2 m_C m_D}{(m_A + m_B)(m_C + m_D)} Q T_i . \tag{B.10}$$

Once the birth position, direction, and energy of the primary particle are determined, it is followed until it either escapes the capsule or loses all its energy. The energy loss of the primary particle is calculated according to Ref. 8 along its path, and a simulated primary particle spectrum [$N_1(E)$] is obtained ($\int_0^{Emax} N_1(E)dE = N_{testp}$.) The primary spectrum [$Y_1(E)$] is obtained by normalizing $N_1(E)$ by,

$$Y_1(E) = \frac{Y_1}{N_{testp}} N_1(E). \qquad \text{(B.11)}$$

B.3 Secondary and knock-on particles

For computational purposes, each primary particle is assumed to produce a secondary particle. As explained in the previous section, each primary particle is followed, and its energy loss is calculated along its path. The secondary fusion reaction cross section (σ_{sec}) is a function of the primary particle energy and is calculated according to Ref. 11. The probability of a secondary fusion reaction per unit length [$R_2(r)$] is obtained by,

$$R_2 = n_D(r)\sigma_{sec}(r), \qquad \text{(B.12)}$$

where n_D is number density of D. R_2 is then integrated and normalized to one so that a random number between zero and one can be used to determine the birth position of secondary particles.

B.3.1 Secondary particle energy and direction

The direction of a secondary particle $(\vec{v}_2)$ is calculated by,

$$\vec{v}_2 = \vec{V}_{CM} + \vec{u}_2, \qquad \text{(B.13)}$$

where $\vec{V}_{CM}$ is the center of mass (CM) velocity, and $\vec{u}_2$ is the velocity of the secondary particle in the CM system. $\vec{V}_{CM}$ is calculated using the velocities of primary particles and thermal D, and $|\vec{u}_2|$ is calculated using energy conservation:

$$|\vec{u}_2| = \left[\frac{2}{m_C + m_D}(Q+K)\left(\frac{m_D}{m_C}\right)\right]^{1/2} \tag{B.14}$$

and the direction of $\vec{u}_2$ is determined using random numbers, since the distribution of the angle between $\vec{V}_{CM}$ and $\vec{u}_2$ is isotropic. The energy of the secondary particle is calculated using $\vec{v}_2$.

The secondary particle is followed until it either exits the imploding capsule or loses all its energy. If the particle escapes, the energy is recorded, and a spectrum of particles per unit energy dN_2/dE is obtained. Since only a small fraction of the primary particles actually undergo secondary reactions, the secondary yield and spectrum need to be normalized according to $Y_2 = \langle P_2 \rangle Y_1$ and $dY_2/dE \approx \langle P_2 \rangle Y_1 (dN_2/dE)/N_2$; $\langle P_2 \rangle \equiv \langle \int n_D(l) \sigma_{sec}(l) dl \rangle$ is the probability of primary-to-secondary conversion, calculated in the program as the primary-yield-weighted mean value of the line integral of the D number density (n_D) times the secondary fusion cross section (σ_{sec}) for all possible primary particle trajectories.

B.3.2 Knock-on particle energy and direction

The program also calculates the spectra of knock-on particles (fuel or shell particles elastically scattered by primary neutrons), which are of great interest for DT-filled capsule implosions. As is the case of secondary particles in D_2-filled capsules, each primary DT neutron is assumed to elastically scatter a particle. Each neutron is followed, and the probability of an elastic scattering per unit length [$R_{ko}(r)$] is obtained by,

$$R_{ko} = n(r)\sigma_{ko}, \tag{B.15}$$

where n is number density of the elastically scattered particle, and σ_{ko} is the total scattering cross section. Since DT neutrons are assumed to scatter only once, σ_{ko} is constant. R_{ko} is then integrated and normalized to one, so that a random number between zero and one can be used to determine the birth position of knock-on (KO) particles.

The energy of the KO particle (E_2) is calculated first. The differential cross section for elastic scattering of DT neutrons off protons, deuterons, or tritons (Figure B.4) is integrated and normalized to one, then a random number is used to select the energy of the knock-on particle.

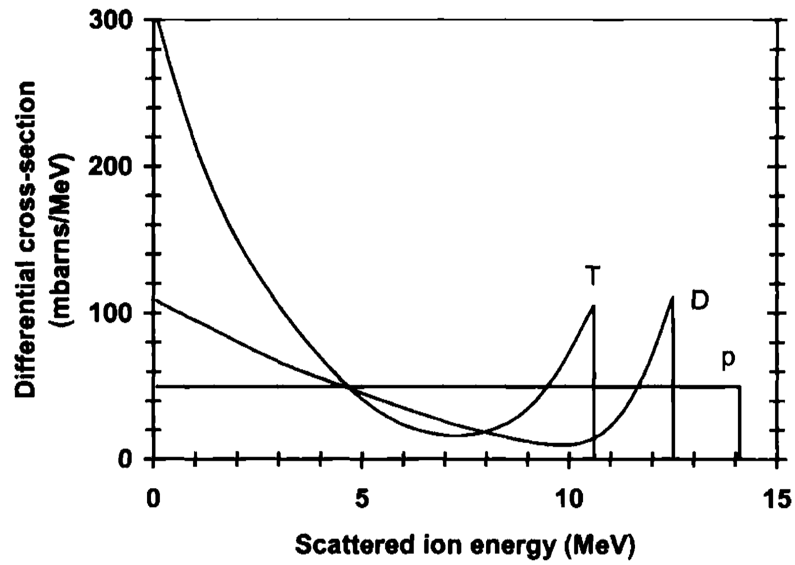

Figure B.4 Differential cross section of elastic scattering of DT neutron off D, T, and p.

The angle between the primary neutron velocity ($\vec{v}_1$) and the direction of the knock-on particle in the DT neutron frame (θ') is given by,

$$\cos\theta' = \left[\frac{(A+1)^2}{4A}\frac{E_2}{E_1}\right]^{1/2}. \tag{B.16}$$

The distribution of the angle around $\vec{v}_1$ (φ') is isotropic, so a random number is used to determine the value of φ'. Figure B.5 shows the relationships between $\vec{v}_1$, θ', and φ'. Since these angles are with respect to $\vec{v}_1$, a rotation matrix is used to obtain the direction of the KO particle in the coordinate system of the imploding capsule. After the direction and energy of the knock-on particle is determined, the same processes are used to obtain the spectrum of knock-on particles, as were used for the secondary particles.

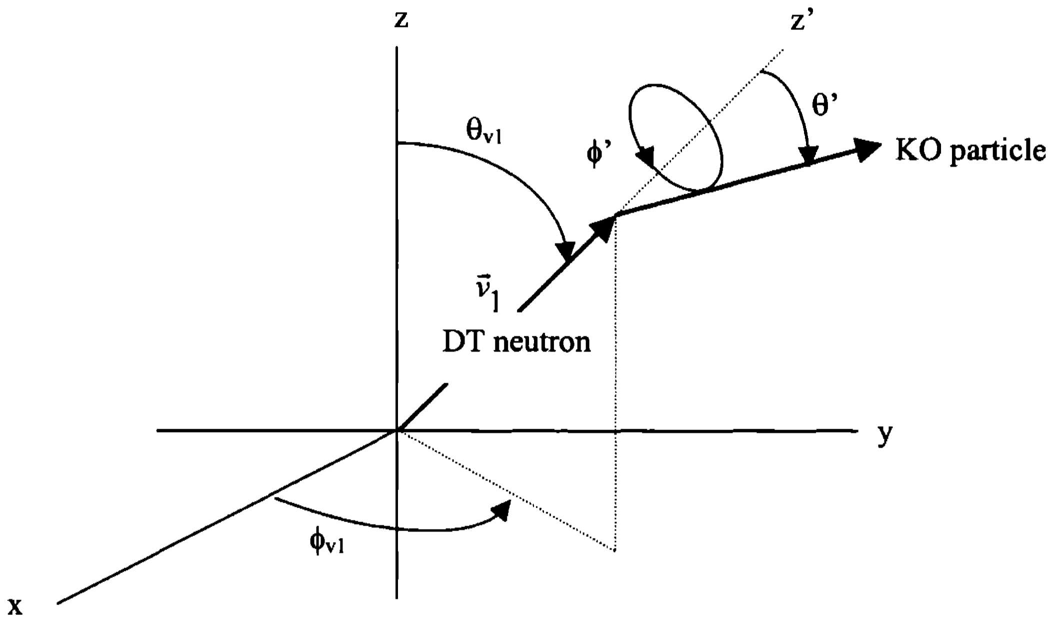

Figure B.5 Relationships between directions of DT neutron and knock-on particles. .

B.4 Ion temperature

There are two methods to calculate the primary-neutron-yield-weighted temperature ($\langle T_i \rangle_{Y1n}$). One way is to integrate the product of the ion temperature and primary reaction rate per unit length (dY_{1n}/dr) over the radius and divide by the primary yield.

$$\langle T_i \rangle_{Y1n} = \frac{\int T_i(r) \frac{dY_{1n}}{dr}(r) dr}{Y_{1n}} \tag{B.17}$$

Another way is to use the Full-Width-Half-Maximum of the primary neutron spectrum. For the neutron branch of the DD fusion reaction, the FWHM is related to the ion temperature by

$$\mathrm{FWHM} = 82.5\sqrt{T_i}\,, \tag{B.18}$$

where FWHM and T_i are in keV [12]. Ion temperatures obtained from the two methods are compared and shown to be virtually identical.

B.5 Best-fit profile

The temperature [$T_i(r)$] and density [$\rho(r)$] profiles are adjusted to find the best fit between the measured and calculated values of Y_{1n}, Y_{2n}/Y_{1n}, Y_{2p}/Y_{1n}, secondary proton mean energy ($\langle E_{2p}\rangle$), and $\langle T_i\rangle_{Y1n}$. The range and the grid size of the six parameters (T_{i0}, σ_{Ti}, p_{Ti}, r_{c0}, σ_c, and p_c) of the Gaussian profiles (equations B.1 and B.2) are defined by the user. The χ^2 for each fitting parameter is calculated as follows:

$$\chi^2_{Y_{1n}} = \frac{\left(Y_{1n}^{meas} - Y_{1n}^{sim}\right)^2}{\Delta Y_{1n}^2} \qquad \text{(B.19)}$$

where Y_{1n}^{meas} and Y_{1n}^{sim} are the measured and simulated values of Y_{1n}, respectively, and

$$\Delta Y_{1n} = \sqrt{\left(\frac{\delta Y_{1n}^{meas}}{Y_{1n}^{meas}}\right)^2 + \left(\frac{\delta t_B}{t_B}\right)^2}\; Y_{1n}^{meas} \qquad \text{(B.20)}$$

where δY_{1n}^{meas} is the absolute error on the measured Y_{1n}, and t_B and δt_B are the measured burn duration and its error, respectively. Since t_B is used to calculate Y_{1n}, it is necessary to include δt_B in the error of Y_{1n}.

$$\chi^2_{Y_2/Y_{1n}} = \frac{\left[Y_2/Y_{1n}{}^{meas} - Y_2/Y_{1n}{}^{sim}\right]^2}{\Delta\left(Y_2^{meas}/Y_{1n}^{meas}\right)^2} \qquad \text{(B.21)}$$

where $Y_2/Y_{1n}{}^{meas}$ and $Y_2/Y_{1n}{}^{sim}$ are the measured and simulated ratios of secondary to primary yields, respectively, and

$$\Delta\left(Y_2^{meas}/Y_{1n}^{meas}\right) = \sqrt{\left(\frac{\Delta Y_{1n}}{Y_{1n}^{meas}}\right)^2 + \left(\frac{\delta Y_2^{meas}}{Y_2^{meas}}\right)^2}\;\left(\frac{Y_2^{meas}}{Y_{1n}^{meas}}\right) \qquad \text{(B.22)}$$

where $\delta Y_2^{measured}$ is the absolute error on the measured Y_2. The same equation is used for Y_{2p}/Y_{1n} and Y_{2n}/Y_{1n}.

$$\chi^2_{E_{2p}} = \frac{\left(E_{2p}^{meas} - E_{2p}^{sim}\right)^2}{\delta E_{2p}^2} \tag{B.23}$$

where E_{2p}^{meas} and E_{2p}^{sim} are the measured and simulated values of the average secondary proton energy, respectively, and δE_{2p} is the error on E_{2p}^{meas}, which is typically 0.10 – 0.15 MeV.

$$\chi^2_{T_i} = \frac{\left(T_i^{meas} - T_i^{sim}\right)^2}{\delta T_i^2} \tag{B.24}$$

where T_i^{meas} and T_i^{sim} are the measured and simulated values of the primary-neutron-yield-averaged temperature, and δT_i is the error on T_i^{meas}, which is typically 0.5 keV.

The total χ^2 is a sum of the five individual χ^2 for each measurable (Y_{1n}, Y_{2n}/Y_{1n}, Y_{2p}/Y_{1n}, $\langle E_{2p}\rangle$, and $\langle T_i\rangle_{Y1n}$). The program first calculates Y_{1n} and $\langle T_i\rangle_{Y1n}$ from the burn profile, then goes through the Monte-Carlo process for the secondary proton spectrum (Y_{2p} and $\langle E_{2p}\rangle$ are obtained) and the secondary neutron spectrum (Y_{2n} is obtained) as explained in Section B.3. Therefore, after each measurable is calculated, its χ^2 is calculated and added to the total χ^2. Once the total χ^2 becomes significantly larger compared to the minimum value of χ^2, the program skips the remaining calculations for that profile and begins a new calculation for the next profile. If the total χ^2 of a particular profile is within some range of minimum χ^2, the values of yields, energy and temperature along with the parameters specifying the profiles are recorded in a file. If the total χ^2 of a profile is smaller than the minimum χ^2, it becomes the new minimum. Although multiple local minima exist within the parameter space, for all simulations there is one clearly defined region with the smallest values of χ^2.

Appendix C: Details of simulated results

In this section, details of the results of simulations of three types of OMEGA implosions are presented. Figure C.1 shows the range of parameters for which total χ^2 is within one of the minimum χ^2 for the low ρR implosion 30981. Results for the medium ρR implosion 27443 and the cryogenic implosion 28900 are shown in Figures C.2 and C.3, respectively.

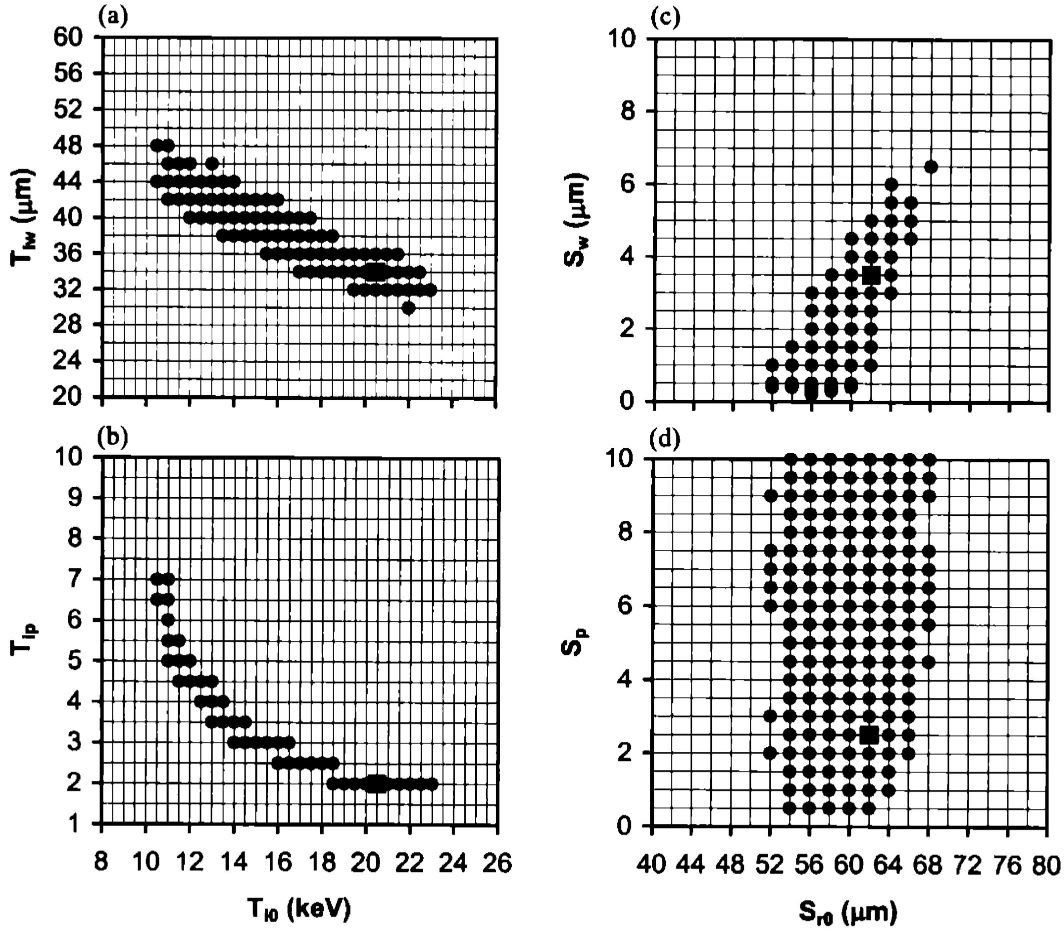

Figure C.1 Range of parameters which produced reasonably good fits to the data for implosion 30981. Large square points represent the best-fit parameters, while other points represent parameters for which total χ^2 were within one of the minimum value. (a) Peak ion temperature (T_{i0}) and 1/e radius of ion temperature Gaussian (T_{iw}), (b) T_{i0} and power of exponent of ion temperature Gaussian (T_{ip}), and (c) position of peak shell density (S_{r0}) and 1/e radius of shell density Gaussian (S_w) show strong correlations. (d) Since S_w is small, nuclear production is insensitive to the power of the exponent of shell density Gaussian (S_p). $S_p > 10$ was not explored since the shape of Gaussian does not show any significant change. Ranges of burn-averaged profiles are shown in Fig. A.4.

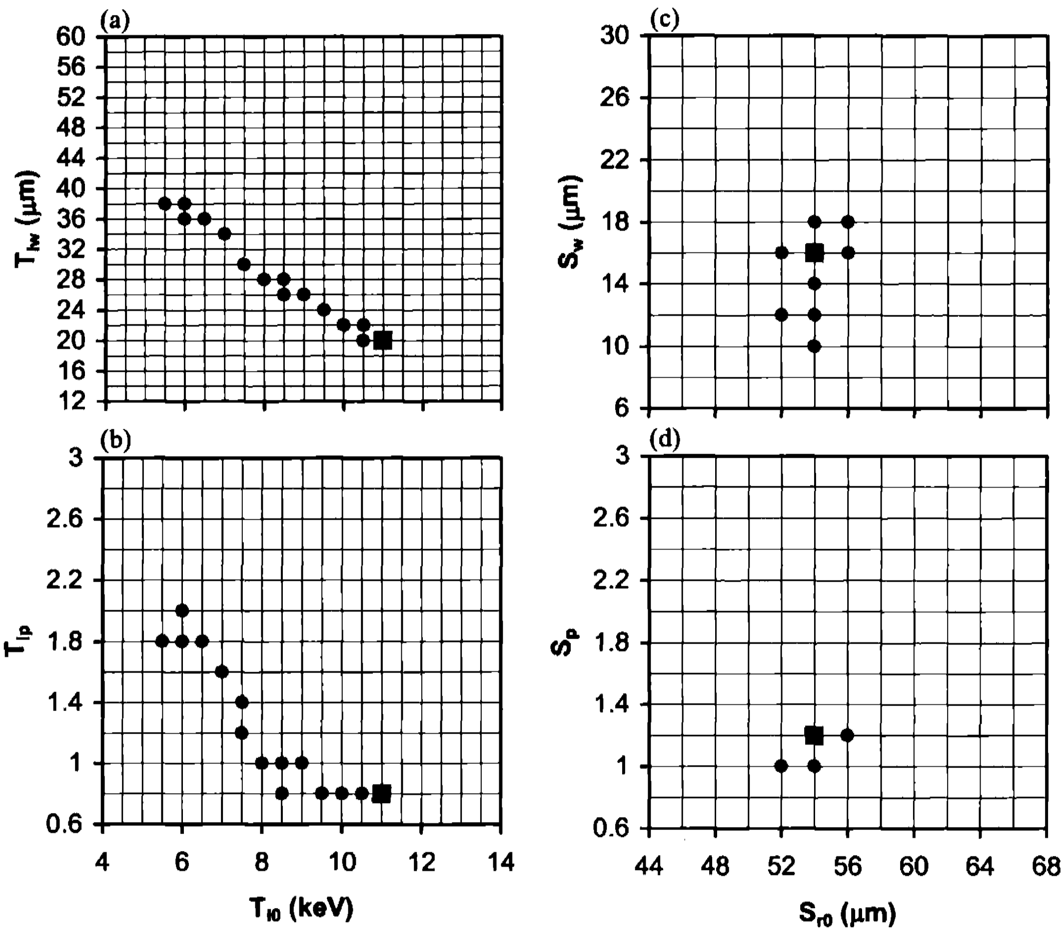

Figure C.2 Range of parameters which produced reasonably good fits to the data for implosion 27443. (a) T_{i0} and T_{iw}, and (b) T_{i0} and T_{ip} show strong correlations. (c and d) S_{r0}, S_w, and S_p are tightly constrained because the amount of mix has a significant impact on secondary yields. (d) Super-Gaussian shell profile is required to mix enough shell material into the fuel to match secondary yields. Range of acceptable profiles are shown in Fig. A.5.

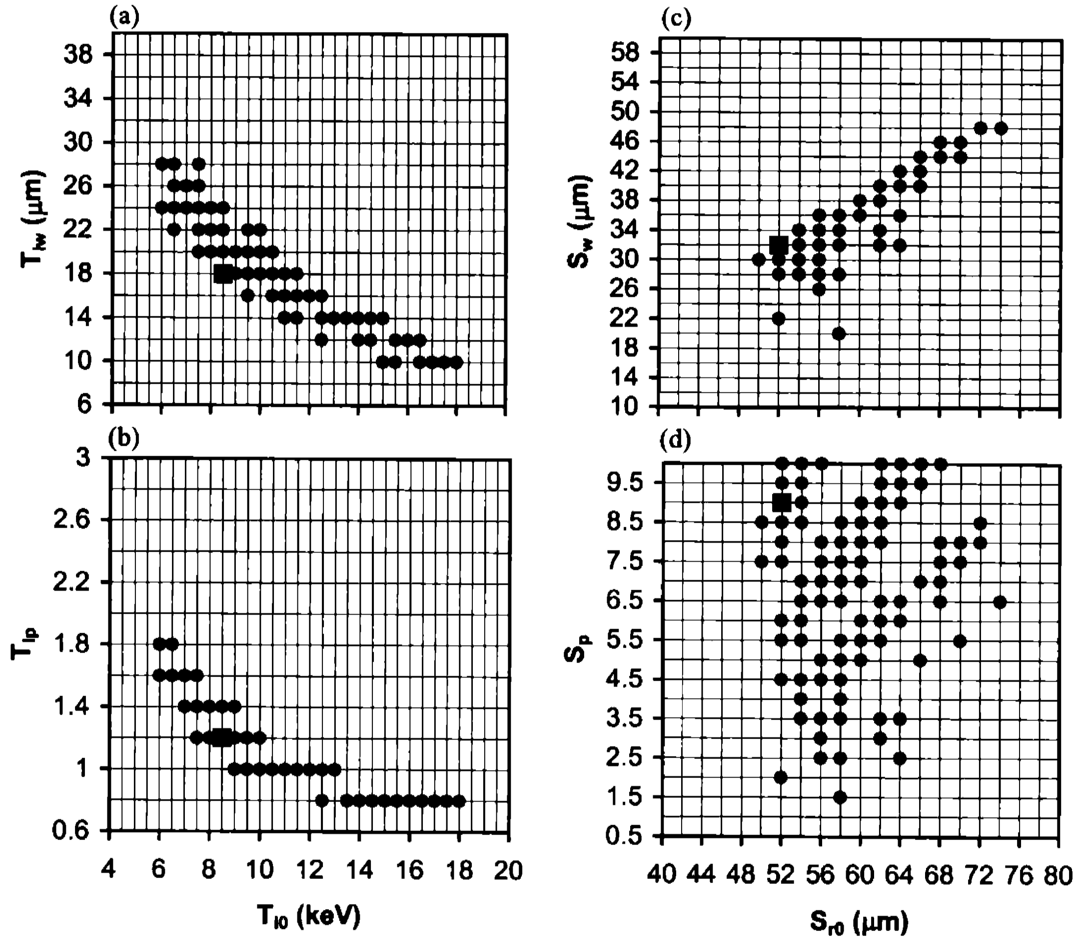

Figure C.3 Range of parameters which produced reasonably good fits to the data for implosion 28900. (a) T_{i0} and T_{iw}, (b) T_{i0} and T_{ip}, and (c) S_{r0} and S_w show strong correlations. Range of acceptable profiles are shown in Fig. A.6.

Appendix D: Compilation of experimental data

Shot information and spectra from various types of D_2 implosions have been compiled for reference purposes. Figs. D.1 and D.2 show the spread of secondary proton energy and yield, respectively. Experimental conditions and measured data are summarized in Table D.1, which is followed by a set of spectra from magnet-based charged-particle spectrometers (CPS1 and CPS2) and wedge-range-filter proton spectrometers (WRFs) for each implosion. Definition of relevant variables is listed prior to the table and the compilation of spectra.

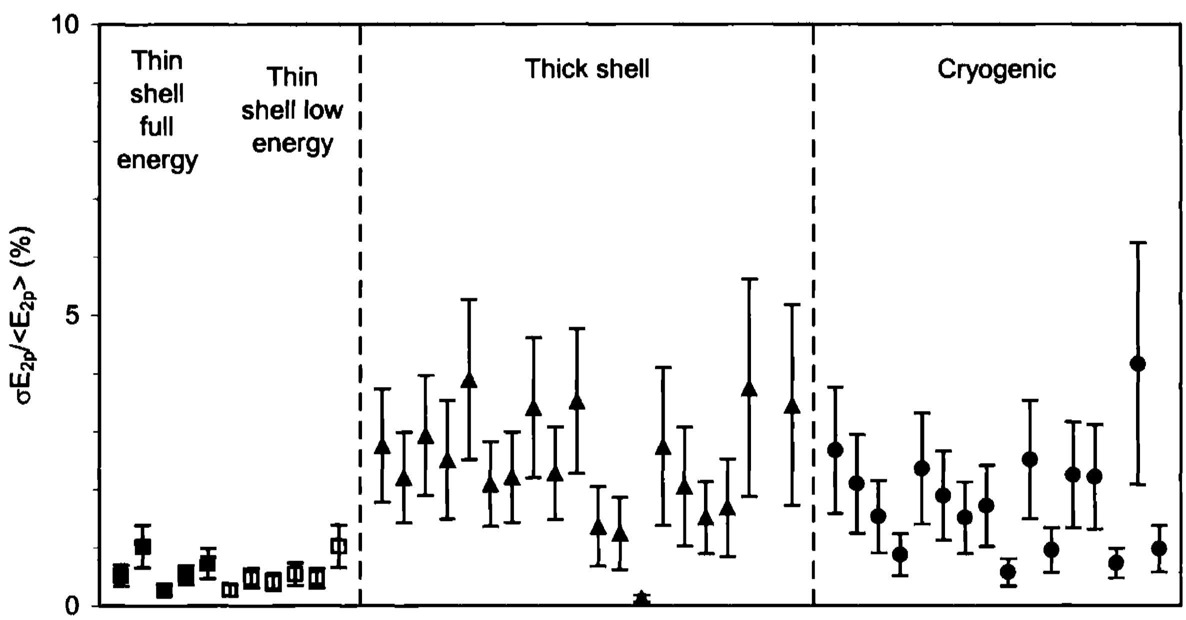

Figure D.1 Relative scatter in measured average secondary proton energy for each shot. The energy spread is small for thin shell implosions because most of shell material is ablated away. For thick shell and cryogenic implosions a significant amount of shell (cold fuel) remains, and the amount of secondary proton energy loss depends heavily on the direction of secondary protons and the amount of shell material remaining in that direction.

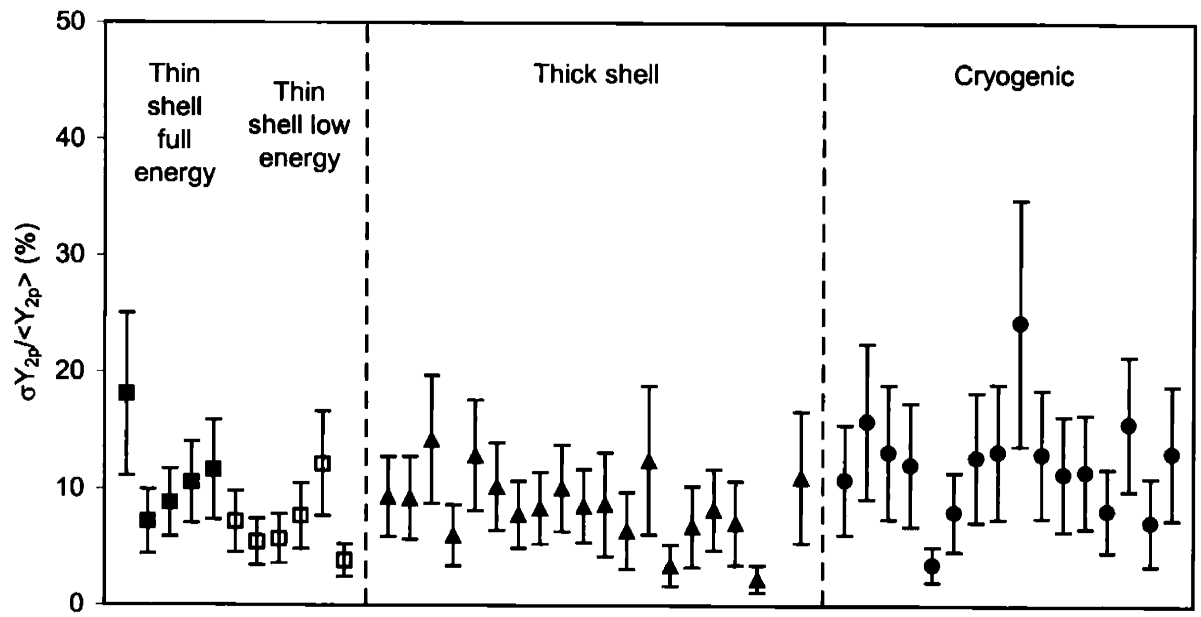

Figure D.2 Relative scatter in measured secondary proton yield for each shot. Yield measurements for thin-shell capsules irradiated with ~23 kJ laser energy, in which nuclear production begins during the laser pulse (while there is a potential difference between the capsule and the target chamber wall), and other types of implosions, in which nuclear production begins after the laser is off, have a similar amount of scatter. This indicates that the potential does not affect charged particle yield measurements.

Definitions of variables:

Shot #:	shot number
Target:	fill(pressure in atm)shell[thickness in μm] diameter in μm
Pulse Shape:	nominal pulse shape SG1018: 1 ns square pulse SG0801: 800 ps pulse*
Laser energy:	measured laser energy delivered to target in kJ
Bang time:	measured time in ps when primary neutron production is at its peak ($t = 0$ occurs when laser is turned on)
Burn width:	measured full-width-half-maximum of primary neutron production rate curve in ps
Y_{1n}:	measured primary neutron yield and its absolute uncertainty and its statistical and absolute errors
Y_{2n}:	measured secondary neutron yield and its absolute uncertainty and its statistical and absolute errors
$\langle T_i \rangle_{Y1n}$:	measured primary-neutron-yield-averaged ion temperature in keV
$\rho R_{hot,n}^{exp1}$:	hot-fuel ρR inferred from Y_{2n}/Y_{1n} using the hot-spot model assuming a $\langle T_i \rangle_{Y1n}$ plasma and its error in mg/cm^2**
$\langle T_i \rangle_{Y2n}$:	calculated secondary-neutron-yield-averaged ion temperature for the type of implosion in keV
$\rho R_{hot,n}^{exp2}$:	hot-fuel ρR inferred from Y_{2n}/Y_{1n} using the hot-spot model assuming a $\langle T_i \rangle_{Y2n}$ plasma and its error in mg/cm^2**
$\langle Y_{2p} \rangle$:	measured average secondary proton yield and its absolute error
σ_{Y2p}:	standard deviation of secondary proton measurements for each implosion
$\sigma(\sigma_{Y2p})$:	standard error in secondary proton measurements
$\rho R_{hot,p}^{exp1}$:	hot-fuel ρR inferred from Y_{2p}/Y_{1n} using the hot-spot model assuming a $\langle T_i \rangle_{Y1n}$ plasma and its error in mg/cm^2**
$\langle T_i \rangle_{Y2p}$:	calculated secondary-proton-yield-averaged ion temperature for the type of implosion in keV
$\rho R_{hot,p}^{exp2}$:	hot-fuel ρR inferred from Y_{2p}/Y_{1n} using the hot-spot model assuming a $\langle T_i \rangle_{Y2p}$ plasma and its error in mg/cm^2**
$\langle E_{2p} \rangle$:	measured average secondary proton energy and its error in MeV
σ_{E2p}:	standard deviation of average secondary proton energy for each implosion
$\sigma(\sigma_{E2p})$:	standard error in secondary proton energy measurements

* pulses with asterisks maintained the pulse shape but were truncated to ~ 650 ps

** D densities of 1.2 +/- 1, 2 +/- 1, and 3 +/- 1.5 g/cc were assumed for thin-glass, thick-plastic, and cryogenic implosions, respectively

Shot	Target	Pulse shape	Laser energy (kJ)	Bang time (ps)	Bang width (ps)	Y_{1n}	statistical error	absolute error	Y_{2n}
Thin									
27817	D_2(15)SiO_2[2.1] 904.2 μm	SG1018	21.5	N/A	N/A	2.0E+11	9.48E+08	4.0E+10	3.5E+07
27819	D_2(15) SiO_2[2.1] 924.2 μm	SG1018	21.7	830	120	2.1E+11	9.54E+08	4.1E+10	2.5E+07
29831	D_2(15) SiO_2[3.3] 925 μm	SG1018	22.9	N/A	N/A	4.5E+11	1.12E+09	9.0E+10	1.6E+08
29833	D_2(15) SiO_2[2.6] 912 μm	SG1018	22.7	900	160	4.1E+11	1.11E+09	8.2E+10	1.2E+08
30979	D_2(14.7) SiO_2[2.9] 911 μm	SG0801	20.5	900	160	3.9E+11	1.02E+09	7.8E+10	9.0E+07
30980	D_2(14.7) SiO_2[2.9] 931 μm	SG0801	13.2	1050	170	2.9E+11	1.04E+09	5.7E+10	1.5E+08
30981	D_2(14.7) SiO_2[3.1] 927 μm	SG0801	13.1	1090	160	1.5E+11	8.52E+08	1.5E+10	7.9E+07
30982	D_2(14.7) SiO_2[3.0] 915 μm	SG0801	12.9	1070	160	1.7E+11	8.80E+08	1.7E+10	7.3E+07
30983	D_2(14.7) SiO_2[2.9] 912 μm	SG0801	11.5	1060	170	1.7E+11	8.83E+08	1.7E+10	6.3E+07
30984	D_2(14.7) SiO_2[2.4] 927 μm	SG0801	11.1	920	160	2.3E+11	9.88E+08	4.6E+10	5.2E+07
30985	D_2(14.7) SiO_2[2.3] 909 μm	SG0801	11.0	970	170	2.0E+11	9.50E+08	4.0E+10	6.2E+07
Thick									
27443	D_2(15) CH[19.4] 934.8 μm	SG1018	22.0	1870	150	1.5E+11	8.40E+08	1.5E+10	2.3E+08
27444	D_2(15) CH[19.4] 935.4 μm	SG1018	21.8	1870	160	1.1E+11	7.06E+08	1.1E+10	1.1E+08
27445	D_2(15) CH[19.2] 939.4 μm	SG1018	22.2	1860	170	7.7E+10	6.02E+08	7.7E+09	7.1E+07
27446	D_2(15) CH[19.3] 939.6 μm	SG1018	21.6	1850	170	5.1E+10	4.92E+08	5.1E+09	4.4E+07
27447	D_2(15) CH[19.3] 930.6 μm	SG1018	21.6	1840	160	1.4E+11	8.23E+08	1.4E+10	2.9E+08
27448	D_2(15) CH[19.2] 930.4 μm	SG1018	21.6	1790	160	1.4E+11	8.05E+08	1.4E+10	2.0E+08
27449	D_2(15) CH[19.3] 939.6 μm	SG1018	22.3	1810	160	1.6E+11	8.73E+08	1.6E+10	2.3E+08
27450	D_2(15) CH[19.3] 933.6 μm	SG1018	22.1	1810	160	1.0E+11	6.97E+08	1.0E+10	1.3E+08
27454	D_2(15) CH[19.4] 942.8 μm	SG1018	22.2	1870	160	1.4E+11	8.23E+08	1.4E+10	2.3E+08
27455	D_2(15) CH[19.3] 940.6 μm	SG1018	21.7	1860	140	1.1E+11	7.22E+08	1.1E+10	1.4E+08
30621	D_2(15) CH[19.4] 937.8 μm	SG1018	N/A	1890	170	1.5E+11	8.25E+08	1.5E+10	2.5E+08
30626	D_2(15) CH[19.1] 948.2 μm	SG1018	22.5	1900	140	1.9E+11	9.36E+08	2.9E+10	3.8E+08
30627	D_2(15) CH[19.4] 941.8 μm	SG1018	22.5	1890	160	1.8E+11	9.18E+08	2.8E+10	4.3E+08
30628	D_2(15) CH[19.3] 945.6 μm	SG1018	22.5	1880	160	2.0E+11	9.47E+08	3.0E+10	4.1E+08
30629	D_2(15) CH[20.6] 945.2 μm	SG1018	22.9	1950	180	1.5E+11	8.46E+08	1.5E+10	3.1E+08
32130	D_2(15) CH[19.1] 878.2 μm	SG1018	24.2	1720	145	2.4E+11	9.93E+08	3.5E+10	4.1E+08
32227	D_2(15) CH[19.1] 880.2 μm	SG1018	24.6	1714	208	2.1E+11	9.66E+08	3.2E+10	4.0E+08
32276	D_2(15) CH[19.3] 876.6 μm	SG1018	23.1	1708	164	1.6E+11	8.60E+08	1.6E+10	3.0E+08
32851	D_2(15) CH[19.4] 877.8 μm	SG1018	22.8	1733	168	1.7E+11	8.86E+08	1.7E+10	2.6E+08
Cryo									
28199	DDcryo	SG1018	21.7	1620	330	1.1E+10	1.83E+08	1.1E+09	9.5E+07
28900	DDcryo layer[89.0] CH[5.1] 918 μm	SG1018	23.3	1620	170	1.2E+11	7.64E+08	1.2E+10	1.2E+09
31279	DDcryo	SG1018	23.1	1830	750	1.1E+10	1.82E+08	1.1E+09	6.5E+07
31281	DDcryo	SG1018	23.0	1780	290	2.1E+10	3.13E+08	2.1E+09	2.0E+08
32129	DDcryo	SG1018	24.1	1650	244	6.2E+10	5.40E+08	6.2E+09	7.0E+08
32223	DDcryo	SG1018	24.4	1560	300	1.2E+11	7.49E+08	1.2E+10	1.2E+09
32225	DDcryo	SG1018	25.0	1256	313	3.2E+10	3.90E+08	3.2E+09	1.1E+08
32272	DDcryo	SG1018	23.2	1660	300	2.8E+10	3.61E+08	2.8E+09	4.2E+08
32273	DDcryo	SG1018	23.2	1705	131	2.8E+10	3.65E+08	2.8E+09	2.9E+08
32845	DDcryo	SG1018	26.5	1617	243	8.8E+10	6.41E+08	8.8E+09	9.2E+08
33412	DDcryo	SG1018	21.5	1250	550	3.3E+10	3.92E+08	3.3E+09	7.5E+07
33413	DDcryo	SG1018	22.0	1614	204	6.7E+10	5.63E+08	6.7E+09	7.2E+08
33415	DDcryo	SG1018	23.1	1641	251	4.2E+10	4.46E+08	4.2E+09	2.4E+08
33599	DDcryo	SG1018	22.7	1654	191	6.5E+10	5.52E+08	6.5E+09	6.9E+08
33603	DDcryo	SG1018	22.8	1672	179	3.9E+10	4.27E+08	3.9E+09	3.5E+08

Table D.1 Experimental conditions and measured data. Definition of variables is listed in the previous page.

Shot	statistical error	absolute error	Y_{2n}/Y_{1n}	Y_{2n}/Y_{1n} error	$<T_i>_{Y1n}$ (keV)	$\rho R_{hot,n}^{exp1}$ (mg/cm^2)	+ error	- error	$<T_i>_{Y2n}$ (keV)	$\rho R_{hot,n}^{exp2}$ (mg/cm^2)	+ error	- error
Thin												
[redacted]												
27819	5.69E+06	6.2E+06	1.2E-04	3.9E-05	10.7	1.1	0.4	0.5	4.0	1.1	0.4	0.5
[redacted]												
29833	1.26E+07	1.7E+07	3.0E-04	7.3E-05	7	2.7	0.7	0.9	4.0	2.7	0.7	0.9
[redacted]												
30980	1.41E+07	2.1E+07	5.3E-04	1.3E-04	6.2	4.8	1.1	1.6	4.0	4.7	1.1	1.6
[redacted]												
30982	9.04E+06	1.2E+07	4.4E-04	8.2E-05	6.6	3.9	0.7	1.0	4.0	3.9	0.7	1.0
[redacted]												
30984	7.66E+06	9.2E+06	2.2E-04	6.0E-05	6.3	2.0	0.5	0.8	4.0	2.0	0.5	0.8
[redacted]												
Thick												
[redacted]												
27444	1.19E+07	1.6E+07	1.0E-03	1.8E-04	4.7	9.0	1.5	2.1	2.5	8.5	1.3	1.9
[redacted]												
27446	7.55E+06	8.7E+06	8.5E-04	1.9E-04	4	7.5	1.6	2.2	2.5	7.2	1.4	2.1
[redacted]												
27448	1.60E+07	2.5E+07	1.4E-03	2.3E-04	3.8	11.7	1.7	2.5	2.5	11.1	1.5	2.2
[redacted]												
27450	1.30E+07	1.8E+07	1.3E-03	2.2E-04	4.3	10.9	1.7	2.5	2.5	10.2	1.5	2.2
[redacted]												
27455	1.37E+07	2.0E+07	1.3E-03	2.2E-04	5.1	10.9	1.7	2.5	2.5	10.2	1.5	2.2
[redacted]												
30626	2.23E+07	4.4E+07	2.0E-03	3.7E-04	4.1	16.1	2.7	3.8	2.5	14.8	2.2	3.3
[redacted]												
30628	2.31E+07	4.7E+07	2.1E-03	3.9E-04	4	16.6	2.7	3.9	2.5	15.2	2.3	3.3
[redacted]												
32130	2.29E+07	4.7E+07	1.7E-03	3.2E-04	4.1	14.2	2.4	3.4	2.5	13.2	2.0	3.0
[redacted]												
32276	1.97E+07	3.6E+07	1.9E-03	2.9E-04	4.4	15.5	2.1	3.1	2.5	14.1	1.8	2.6
[redacted]												
Cryo												
[redacted]												
28900	3.17E+07	1.2E+08	9.4E-03	1.4E-03	3.6	49.8	5.0	6.9	1.0	20.2	7.8	6.5
[redacted]												
31281	1.61E+07	2.6E+07	9.5E-03	1.6E-03	2.8	43.4	5.4	7.1	1.0	20.2	7.8	6.6
[redacted]												
32223	3.91E+07	1.2E+08	9.9E-03	1.4E-03	3.9	53.3	5.2	7.2	1.0	20.5	8.0	6.8
[redacted]												
32272	2.33E+07	4.8E+07	1.5E-02	2.3E-03	2.4	47.2	7.5	8.7	1.0	12.1		
[redacted]												
32845	3.45E+07	9.8E+07	1.0E-02	1.5E-03	4.2	57.0	5.5	7.7	1.0	20.9	8.1	7.2
[redacted]												
33413	3.06E+07	7.8E+07	1.1E-02	1.6E-03	3.2	49.8	5.5	7.2	1.0	21.0	8.1	7.3
[redacted]												
33599	2.99E+07	7.5E+07	1.1E-02	1.6E-03	2.9	46.6	5.6	7.1	1.0	20.9	8.1	7.2
[redacted]												

Table D.1

Shot	$\langle Y_{2p} \rangle$	absolute error	σY_{2p}	$\sigma(\sigma Y_{2p})$	$\sigma Y_{2p}/\langle Y_{2p} \rangle$ (%)	error	Y_{2p}/Y_{1n}	Y_{2p}/Y_{1n} error	$\rho R_{hot,p}^{exp1}$ (mg/cm^2)	+ error	- error	$\langle T_i \rangle_{Y2p}$ (keV)
Thin												
27817	**2.9E+07**	**4.4E+06**	**5.3E+06**	**1.9E+06**	**18.1**	**6.9**	**1.5E-04**	**3.7E-05**	**0.8**	**0.2**	**0.3**	**4.0**
27819	2.6E+07	3.9E+06	1.9E+06	6.6E+05	7.2	2.8	1.3E-04	3.2E-05	0.8	0.2	0.2	4.0
29831	**2.7E+08**	**2.7E+07**	**2.4E+07**	**7.6E+06**	**8.8**	**2.9**	**6.1E-04**	**1.4E-04**	**3.2**	**0.7**	**1.0**	**4.0**
29833	1.1E+08	1.1E+07	1.1E+07	3.5E+06	10.6	3.5	2.6E-04	5.8E-05	1.4	0.3	0.4	4.0
30979	**1.3E+08**	**1.3E+07**	**1.5E+07**	**5.3E+06**	**11.6**	**4.3**	**3.3E-04**	**7.4E-05**	**1.8**	**0.4**	**0.6**	**4.0**
30980	2.2E+08	2.2E+07	1.6E+07	5.5E+06	7.2	2.6	7.6E-04	1.7E-04	4.0	0.9	1.2	4.0
30981	**1.2E+08**	**1.2E+07**	**6.7E+06**	**2.4E+06**	**5.5**	**2.0**	**7.9E-04**	**1.1E-04**	**4.3**	**0.6**	**0.8**	**4.0**
30982	1.1E+08	1.1E+07	6.1E+06	2.1E+06	5.7	2.1	6.3E-04	8.9E-05	3.4	0.5	0.7	4.0
30983	**1.2E+08**	**1.2E+07**	**9.4E+06**	**3.3E+06**	**7.7**	**2.8**	**7.2E-04**	**1.0E-04**	**3.8**	**0.5**	**0.7**	**4.0**
30984	1.4E+08	1.4E+07	1.6E+07	5.8E+06	12.1	4.5	5.8E-04	1.3E-04	3.1	0.7	1.0	4.0
30985	**1.1E+08**	**1.1E+07**	**4.0E+06**	**1.4E+06**	**3.8**	**1.4**	**5.2E-04**	**1.2E-04**	**2.8**	**0.6**	**0.9**	**4.0**
Thick												
27443	**1.5E+08**	**1.5E+07**	**1.4E+07**	**4.9E+06**	**9.3**	**3.4**	**1.0E-03**	**1.4E-04**	**5.0**	**0.7**	**1.0**	**3.0**
27444	6.8E+07	1.0E+07	6.3E+06	2.2E+06	9.2	3.5	6.4E-04	1.2E-04	3.3	0.6	0.8	3.0
27445	**5.2E+07**	**7.8E+06**	**7.4E+06**	**2.6E+06**	**14.2**	**5.5**	**6.7E-04**	**1.2E-04**	**3.4**	**0.6**	**0.8**	**3.0**
27446	2.7E+07	4.1E+06	1.6E+06	6.7E+05	6.0	2.6	5.3E-04	9.5E-05	2.7	0.5	0.7	3.0
27447	**1.7E+08**	**1.7E+07**	**2.2E+07**	**7.7E+06**	**12.9**	**4.7**	**1.2E-03**	**1.7E-04**	**5.9**	**0.8**	**1.2**	**3.0**
27448	1.9E+08	1.9E+07	1.9E+07	6.9E+06	10.2	3.8	1.3E-03	1.9E-04	7.2		1.4	3.0
27449	**1.6E+08**	**1.6E+07**	**1.3E+07**	**4.4E+06**	**7.8**	**2.9**	**9.7E-04**	**1.4E-04**	**4.9**	**0.7**	**0.9**	**3.0**
27450	8.9E+07	8.9E+06	7.5E+06	2.6E+06	8.4	3.1	8.6E-04	1.2E-04	4.4	0.6	0.8	3.0
27454	**1.8E+08**	**1.8E+07**	**1.8E+07**	**6.4E+06**	**10.1**	**3.7**	**1.3E-03**	**1.8E-04**	**6.2**	**1.0**	**0.9**	**3.0**
27455	1.0E+08	1.0E+07	8.6E+06	3.0E+06	8.6	3.1	8.8E-04	1.2E-04	4.5		3.3	3.0
30621	**2.3E+08**	**2.3E+07**	**2.0E+07**	**1.0E+07**	**8.7**	**4.4**	**1.6E-03**	**2.2E-04**	**7.4**	**1.2**	**1.1**	**3.0**
30626	4.1E+08	4.1E+07	2.6E+07	1.3E+07	6.5	3.3	2.1E-03	3.8E-04	11.1	3.4	2.3	3.0
30627	**3.7E+08**	**3.7E+07**	**4.6E+07**	**2.3E+07**	**12.5**	**6.4**	**2.0E-03**	**3.6E-04**	**10.7**	**4.3**	**2.4**	**3.0**
30628	4.4E+08	4.4E+07	1.5E+07	7.6E+06	3.5	1.8	2.2E-03	3.9E-04	11.6	4.5	2.6	3.0
30629	**3.7E+08**	**3.7E+07**	**2.5E+07**	**1.3E+07**	**6.8**	**3.5**	**2.4E-03**	**3.4E-04**	**13.9**		**3.3**	**3.0**
32130	5.7E+08	5.7E+07	4.7E+07	1.9E+07	8.3	3.5	2.4E-03	4.4E-04	13.4		3.3	3.0
32227	**4.3E+08**	**4.3E+07**	**3.1E+07**	**1.5E+07**	**7.1**	**3.6**	**2.0E-03**	**3.6E-04**	**10.3**	**2.7**	**2.1**	**3.0**
32276	2.5E+08	2.5E+07	5.8E+06	2.9E+06	2.3	1.2	1.6E-03	2.2E-04	7.8	1.2	1.1	3.0
32851	**3.2E+08**	**3.2E+07**	**3.5E+07**	**1.8E+07**	**11.0**	**5.6**	**1.9E-03**	**2.7E-04**	**9.5**	**1.6**	**1.4**	**3.0**
Cryo												
28199	**1.6E+07**	**2.4E+06**	**1.7E+06**	**7.1E+05**	**10.8**	**4.7**	**1.5E-03**	**2.7E-04**	**7.5**	**1.9**	**1.5**	**2.5**
28900	2.3E+08	2.3E+07	3.6E+07	1.5E+07	15.8	6.6	1.8E-03	2.6E-04	9.3	1.9	1.5	2.5
31279	**1.2E+07**	**1.8E+06**	**1.6E+06**	**6.5E+05**	**13.2**	**5.7**	**1.1E-03**	**2.0E-04**	**5.6**	**1.0**	**1.4**	**2.5**
31281	3.5E+07	5.3E+06	4.2E+06	1.7E+06	12.1	5.3	1.7E-03	3.0E-04	9.4		2.6	2.5
32129	**1.4E+08**	**1.4E+07**	**5.0E+06**	**2.0E+06**	**3.6**	**1.5**	**2.3E-03**	**3.2E-04**	**13.0**		**3.0**	**2.5**
32223	3.1E+08	3.1E+07	2.5E+07	1.0E+07	8.1	3.4	2.6E-03	3.7E-04	16.3		4.8	2.5
32225	**3.7E+07**	**5.6E+06**	**4.7E+06**	**1.9E+06**	**12.7**	**5.5**	**1.1E-03**	**2.1E-04**	**5.7**			**2.5**
32272	3.7E+07	5.6E+06	4.9E+06	2.0E+06	13.2	5.8	1.3E-03	2.4E-04	7.0			
32273	**2.5E+07**	**3.8E+06**	**6.1E+06**	**2.5E+06**	**24.3**	**10.6**	**8.8E-04**	**1.6E-04**	**4.4**	**0.8**	**1.1**	**2.5**
32845	1.7E+08	1.7E+07	2.2E+07	9.1E+06	13.0	5.5	1.9E-03	2.7E-04	9.8	1.7	1.5	2.5
33412	**2.1E+07**	**3.2E+06**	**2.4E+06**	**9.7E+05**	**11.3**	**4.9**	**6.4E-04**	**1.2E-04**	**3.4**	**0.6**	**0.8**	**2.5**
33413	1.3E+08	1.3E+07	1.5E+07	6.1E+06	11.5	4.8	1.9E-03	2.7E-04	10.8		2.4	2.5
33415	**5.4E+07**	**8.1E+06**	**4.4E+06**	**1.8E+06**	**8.2**	**3.6**	**1.3E-03**	**2.3E-04**	**6.4**	**1.2**	**1.6**	**2.5**
33599	1.4E+08	1.4E+07	2.2E+07	7.7E+06	15.6	5.7	2.2E-03	3.1E-04	9.2			2.5
33603	**7.7E+07**	**1.2E+07**	**5.6E+06**	**2.8E+06**	**7.2**	**3.8**	**2.0E-03**	**3.6E-04**	**11.4**		**2.8**	**2.5**

Table D.1

Shot	$\rho R_{hot,p}^{exp2}$ (mg/cm^2)	+ error	- error	$\langle E_{2p} \rangle$ (MeV)	+/- error	σE_{2p}	$\sigma(\sigma E_{2p})$	$\sigma E_{2p}/\langle E_{2p} \rangle$ (%)	error
Thin									
[illegible]	[illegible]	[illegible]	[illegible]	[illegible]	[illegible]	[illegible]	[illegible]	[illegible]	0.2
27819	0.7	0.2	0.3	15.28	0.15	0.16	0.06	1.0E+00	0.4
[illegible]	[illegible]	[illegible]	[illegible]	[illegible]	[illegible]	[illegible]	0.01	2.7E-01	0.1
29833	1.4	0.3	0.4	15.09	0.10	0.08	0.03	5.3E-01	0.2
[illegible]	[illegible]	[illegible]	[illegible]	[illegible]	0.10	[illegible]	0.04	7.3E-01	0.3
30980	3.9	0.8	1.2	14.68	0.10	0.04	0.01	2.7E-01	0.1
[illegible]	[illegible]	[illegible]	[illegible]	[illegible]	[illegible]	[illegible]	0.02	[illegible]	0.2
30982	3.2	0.4	0.6	14.64	0.10	0.06	0.02	4.1E-01	0.1
[illegible]	[illegible]	[illegible]	[illegible]	[illegible]	0.10	[illegible]	0.03	[illegible]	0.2
30984	3.0	0.6	0.9	14.72	0.10	0.07	0.02	4.8E-01	0.2
[illegible]	[illegible]	[illegible]	[illegible]	[illegible]	0.10	[illegible]	[illegible]	1.0E+00	0.4
Thick									
[illegible]	[illegible]	[illegible]	[illegible]	[illegible]	0.10	[illegible]	0.13	[illegible]	1.0
27444	3.2	0.6	0.8	13.55	0.10	0.30	0.11	2.2E+00	0.8
[illegible]	[illegible]	[illegible]	[illegible]	[illegible]	0.10	0.40	0.14	[illegible]	1.0
27446	2.7	0.5	0.6	13.79	0.10	0.35	0.14	2.5E+00	1.0
[illegible]	[illegible]	[illegible]	[illegible]	[illegible]	0.10	[illegible]	0.18	[illegible]	1.4
27448	6.7	1.3	1.0	13.10	0.10	0.27	0.10	2.1E+00	0.7
[illegible]	[illegible]	[illegible]	[illegible]	[illegible]	[illegible]	[illegible]	0.10	2.2E+00	[illegible]
27450	4.3	0.6	0.8	13.51	0.10	0.46	0.16	3.4E+00	1.2
[illegible]	[illegible]	[illegible]	[illegible]	[illegible]	[illegible]	[illegible]	0.11	[illegible]	[illegible]
27455	4.3	0.6	0.9	13.19	0.10	0.46	0.16	3.5E+00	1.2
[illegible]	[illegible]	[illegible]	[illegible]	[illegible]	[illegible]	[illegible]	[illegible]	[illegible]	0.7
30626	7.8			12.78	0.10	0.16	0.08	1.2E+00	0.6
[illegible]	[illegible]			[illegible]	0.10	[illegible]	0.01	1.2E-01	0.1
30628	8.8			12.81	0.10	0.35	0.18	2.7E+00	1.4
[illegible]	[illegible]			[illegible]	0.10	[illegible]	0.13	2.1E+00	1.0
32130	15.2			12.74	0.10	0.19	0.08	1.5E+00	0.6
[illegible]	[illegible]			[illegible]	0.10	0.22	0.11	1.7E+00	[illegible]
32276	8.2	2.9	1.5	12.57	0.10	0.47	0.24	3.7E+00	1.9
[illegible]	[illegible]	[illegible]	[illegible]	[illegible]	0.10	[illegible]	0.22	[illegible]	1.7
Cryo									
[illegible]	[illegible]		[illegible]	[illegible]	0.10	[illegible]	0.15	2.7E+00	1.1
28900	7.5			13.31	0.10	0.28	0.11	2.1E+00	0.9
[illegible]	[illegible]	[illegible]	[illegible]	[illegible]	0.10	0.21	0.09	[illegible]	[illegible]
31281	4.3			13.84	0.10	0.12	0.05	8.7E-01	0.4
[illegible]	[illegible]			[illegible]	0.10	[illegible]	0.13	2.4E+00	1.0
32223	12.6			13.62	0.10	0.26	0.10	1.9E+00	0.8
[illegible]	[illegible]			[illegible]	[illegible]	[illegible]	[illegible]	[illegible]	[illegible]
32272				13.76	0.10	0.24	0.10	1.7E+00	0.7
[illegible]	[illegible]	[illegible]	[illegible]	[illegible]	[illegible]	[illegible]	0.03	[illegible]	0.2
32845	11.9			13.76	0.10	0.35	0.14	2.5E+00	1.0
[illegible]	[illegible]	[illegible]	[illegible]	[illegible]	[illegible]	[illegible]	[illegible]	[illegible]	[illegible]
33413	10.8			13.66	0.10	0.31	0.13	2.2E+00	0.9
[illegible]	[illegible]	[illegible]	[illegible]	[illegible]	0.10	[illegible]	0.13	2.2E+00	0.9
33599	12.6			13.61	0.10	0.10	0.03	7.2E-01	0.3
[illegible]	[illegible]			[illegible]	0.10	[illegible]	0.29	[illegible]	2.1

Table D.1

Definitions:

Shot #:	shot number
Target:	fill(pressure in atm)shell[thickness in μm] diameter in μm
On-Target Energy:	energy delivered to target in kJ
Pulse Shape:	nominal pulse shape SG1018: 1 ns square pulse SG0801: 800 ps pulse*
Y_{1n}:	primary neutron yield and its absolute error
$\langle T_i \rangle_{Y1n}$:	primary-neutron-yield-averaged ion temperature in keV
Bang Time:	time in ps when primary neutron production is at its peak (t = 0 when laser is turned on)
Burn Width:	full-width-half-maximum of primary neutron production rate curve in ps
Y_{2n}:	secondary neutron yield and its absolute error
$\langle Y_{2p} \rangle$:	average secondary proton yield over all WRFs and its absolute error
$\rho R_{hot,2p,hot\text{-}spot}$:	hot-fuel areal density inferred from Y_{2p}/Y_{1n} using the hot-spot model**
$\rho R_{hot,2n,hot\text{-}spot}$:	hot-fuel areal density inferred from Y_{2n}/Y_{1n} using the hot-spot model**
$\rho R_{hot,2p,uniform}$:	hot-fuel areal density inferred from Y_{2p}/Y_{1n} using the uniform model**
$\rho R_{hot,2n,uniform}$:	hot-fuel areal density inferred from Y_{2n}/Y_{1n} using the uniform model**
$\langle E_{2p} \rangle$:	average secondary proton energy over all WRFs and its absolute error
ρR_{total}:	total areal density inferred from secondary proton energy downshift***

Charged-particle-spectrometer (CPS) data

Port:	CPS-1 or CPS-2 (width of collimator in mm)
Particle detected:	particle type detected on CPS
Yield:	yield of charged particle
Yield (Gaussian):	yield of charged particle under best-fit Gaussian to the spectrum
$\langle E \rangle$:	average energy of particle
$\langle E \rangle$ (Gaussian):	average energy of particle under best-fit Gaussian to the spectrum
σ (Gaussian):	standard deviation of Gaussian fit
$\langle T_i \rangle$:	ion temperature determined using standard deviation of spectrum

Wedge-range-filter (WRF) spectrometer data

Port:	position of WRF in OMEGA chamber (TIM 1-6 and KO 1-3) and its distance from target chamber center in cm
Y_{2p}:	yield of secondary protons****
$\langle E \rangle$:	average energy of secondary protons in MeV*****

* pulses with asterisk maintained the pulse shape but were truncated to ~ 650 ps
** ion temperature of $\langle T_i \rangle_{Y1n}$ +/- 0.5 keV and D densities of 1.2 +/- 1, 2 +/- 1, and 3 +/- 1.5 g/cc were assumed for thin-glass, thick-plastic, and cryogenic implosions, respectively

*** ion temperature of 1 keV, and SiO_2, CH, and cold D densities of 5, 10, and 7 g/cc were assumed for thin-glass, thick-plastic, and cryogenic implosions, respectively. For implosions in which nuclear production began during the laser pulse, is not calculated because secondary proton energy was upshifted by unknown amount due to charging of capsule.
**** error on each WRF yield measurement is a percentage of the total yield (10 – 15% depending on statistics)
***** error on each WRF energy measurement is 0.1 – 0.15 MeV depending on statistics

Summary of thin shell implosions

Shot #	Target	On-Target Energy (kJ)	Pulse Shape	Y_{1n} ($x10^{11}$)	$<T_i>_{Y1n}$ (keV)	Bang Time (ps)	Burn Width (ps)
27817	$D_2(15)$ $SiO_2[2.1]$ 904.2 um	21.5	SSD: SG1018	2.0 ± 0.4	8.4 ± 0.5	Not Available	Not Available

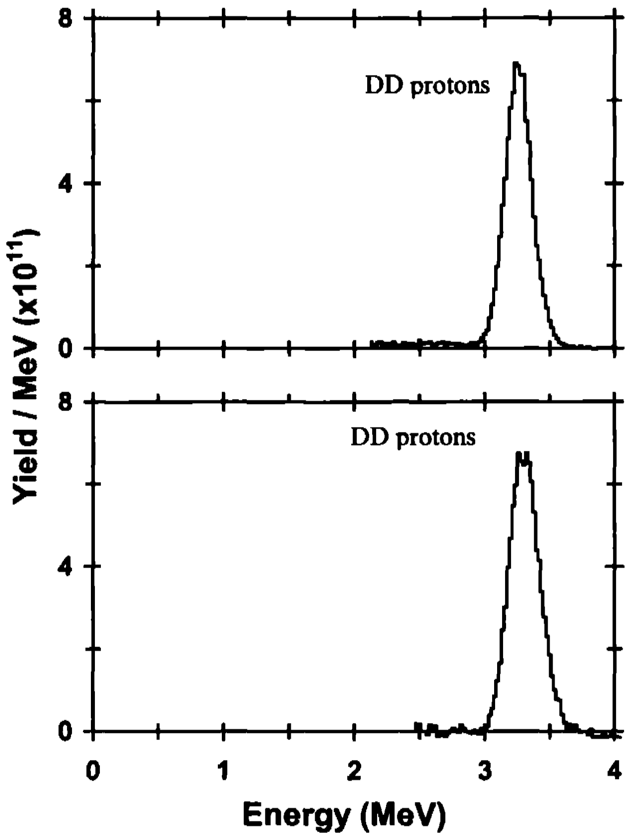

CPS-1 (1mm slit)

DD protons

Yield (Gaussian):	(1.8 ± 0.2) $x10^{11}$
<E> (Gaussian):	3.26 ± 0.02 MeV
σ (Gaussian):	0.10
$<T_i>$:	6.3 keV

CPS-2 (1mm slit)

DD protons

Yield (Gaussian):	(2.0 ± 0.2) $x10^{11}$
<E> (Gaussian):	3.31 ± 0.02 MeV
σ (Gaussian):	0.12
$<T_i>$:	9.2 keV

Note:

Shot #	$\langle Y_{2p}\rangle$ $(x10^7)$	Y_{2n} $(x10^7)$	$\rho R_{hot, 2p,}$ hot-spot (mg/cm^2)	$\rho R_{hot, 2n,}$ hot-spot (mg/cm^2)	$\rho R_{hot, 2p,}$ uniform (mg/cm^2)	$\rho R_{hot, 2n,}$ uniform (mg/cm^2)	$\langle E_{2p}\rangle$ (MeV)	ρR_{total} (mg/cm^2)
27817	2.9 +/- 0.4	3.5 +/- 0.8	0.8 + 0.2 - 0.3	1.6 + 0.5 - 0.7	1.1 + 0.3 - 0.4	2.1 + 0.6 - 0.9	15.25 +/- 0.15	N/A

Secondary proton spectra from WRF

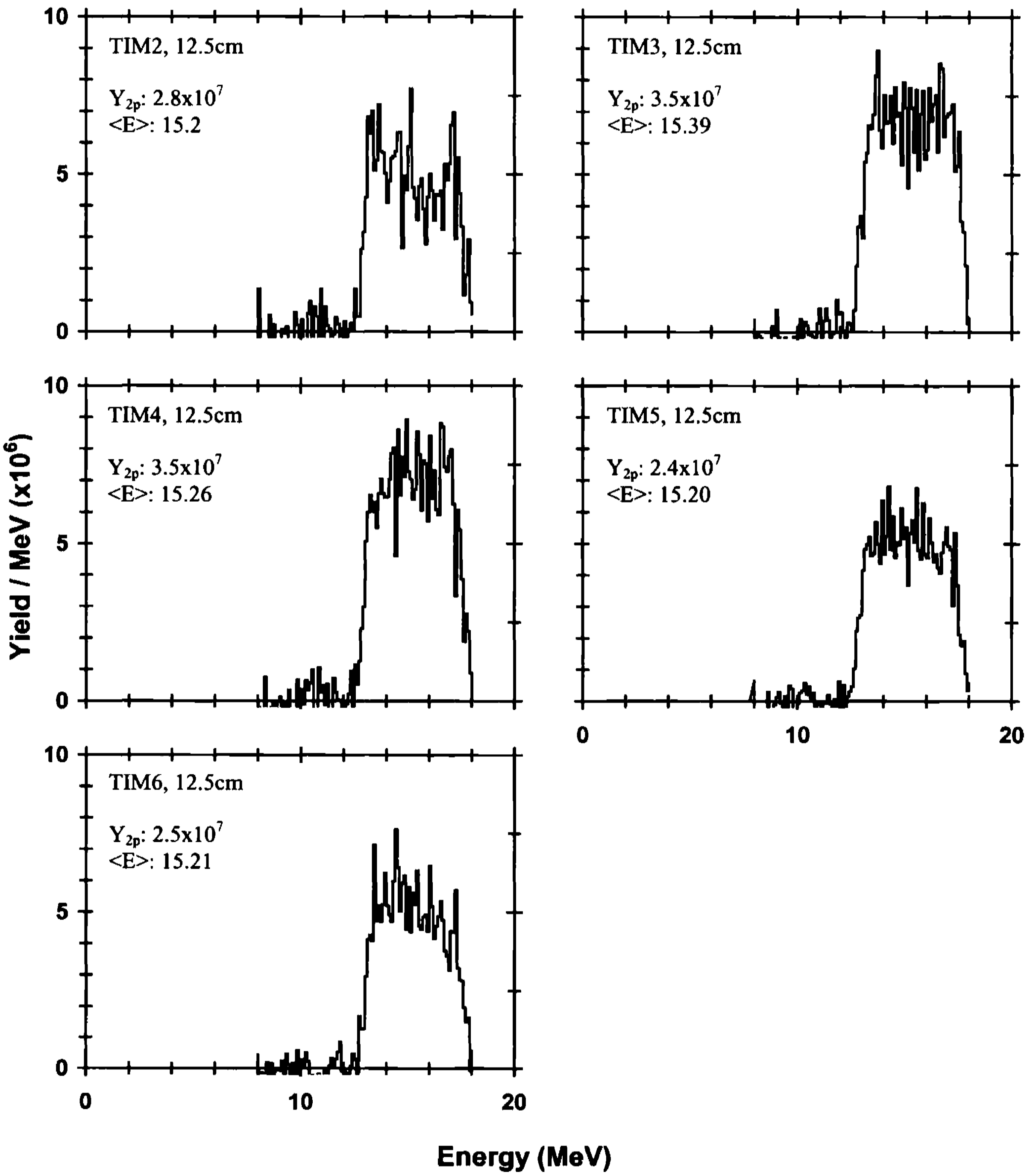

Shot #	Target	On-Target Energy (kJ)	Pulse Shape	Y_{1n} ($x10^{11}$)	$<T_i>_{Y1n}$ (keV)	Bang Time (ps)	Burn Width (ps)
27819	D_2(15) SiO_2[2.1] 924.2	21.7	SSD: SG1018	2.1 +/- 0.4	10.7 +/- 0.5	830 +/- 50	120 +/- 25

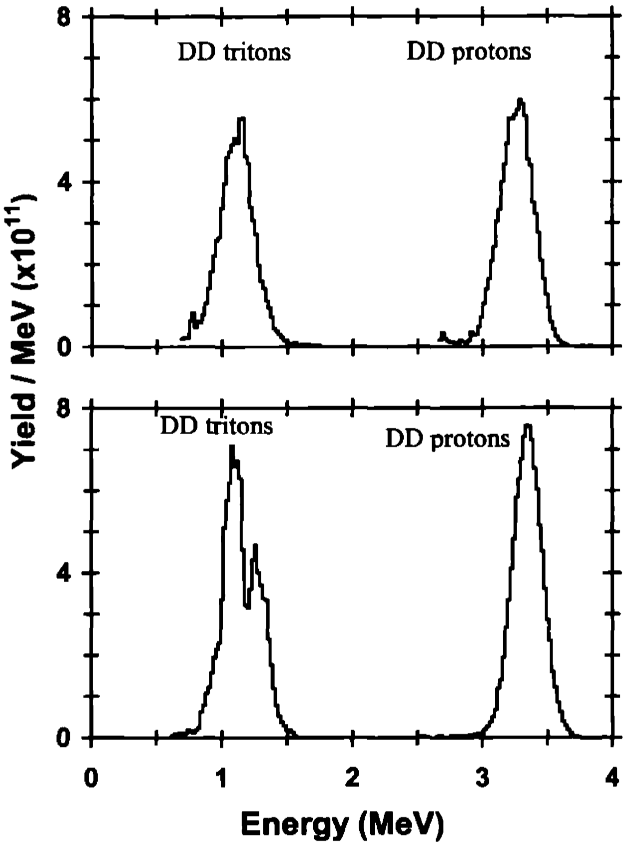

CPS-1 (1mm slit)

DD protons

Yield (Gaussian):	$(1.9 \pm 0.2) \times 10^{11}$
<E> (Gaussian):	3.27 ± 0.02 MeV
σ (Gaussian):	0.13
$<T_i>$:	11.2 keV

DD tritons

Yield (Gaussian):	$(1.7 \pm 0.2) \times 10^{11}$
<E> (Gaussian):	1.11 ± 0.02 MeV
σ (Gaussian):	0.13
$<T_i>$:	11.0 keV

CPS-2 (1mm slit)

DD protons

Yield (Gaussian):	$(2.1 \pm 0.2) \times 10^{11}$
<E> (Gaussian):	3.34 ± 0.02 MeV
σ (Gaussian):	0.11
$<T_i>$:	7.7 keV

DD tritons

Yield:	$(2.1 \pm 0.2) \times 10^{11}$
<E>:	1.15 ± 0.02 MeV
Standard deviation:	0.14

Note:

Shot #	$<Y_{2p}>$ (x107)	Y_{2n} ($x10^7$)	$\rho R_{hot, 2p,}$ hot-spot (mg/cm^2)	$\rho R_{hot, 2n,}$ hot-spot (mg/cm^2)	$\rho R_{hot, 2p,}$ uniform (mg/cm^2)	$\rho R_{hot, 2n,}$ uniform (mg/cm^2)	$<E_{2p}>$ (MeV)	ρR_{total} (mg/cm^2)
27819	2.6 +/- 0.4	2.5 +/- 0.6	0.7 + 0.2 - 0.2	1.1 + 0.4 - 0.5	0.9 + 0.2 - 0.3	1.4 + 0.5 - 0.6	15.28 +/- 0.15	N/A

Secondary proton spectra from WRF

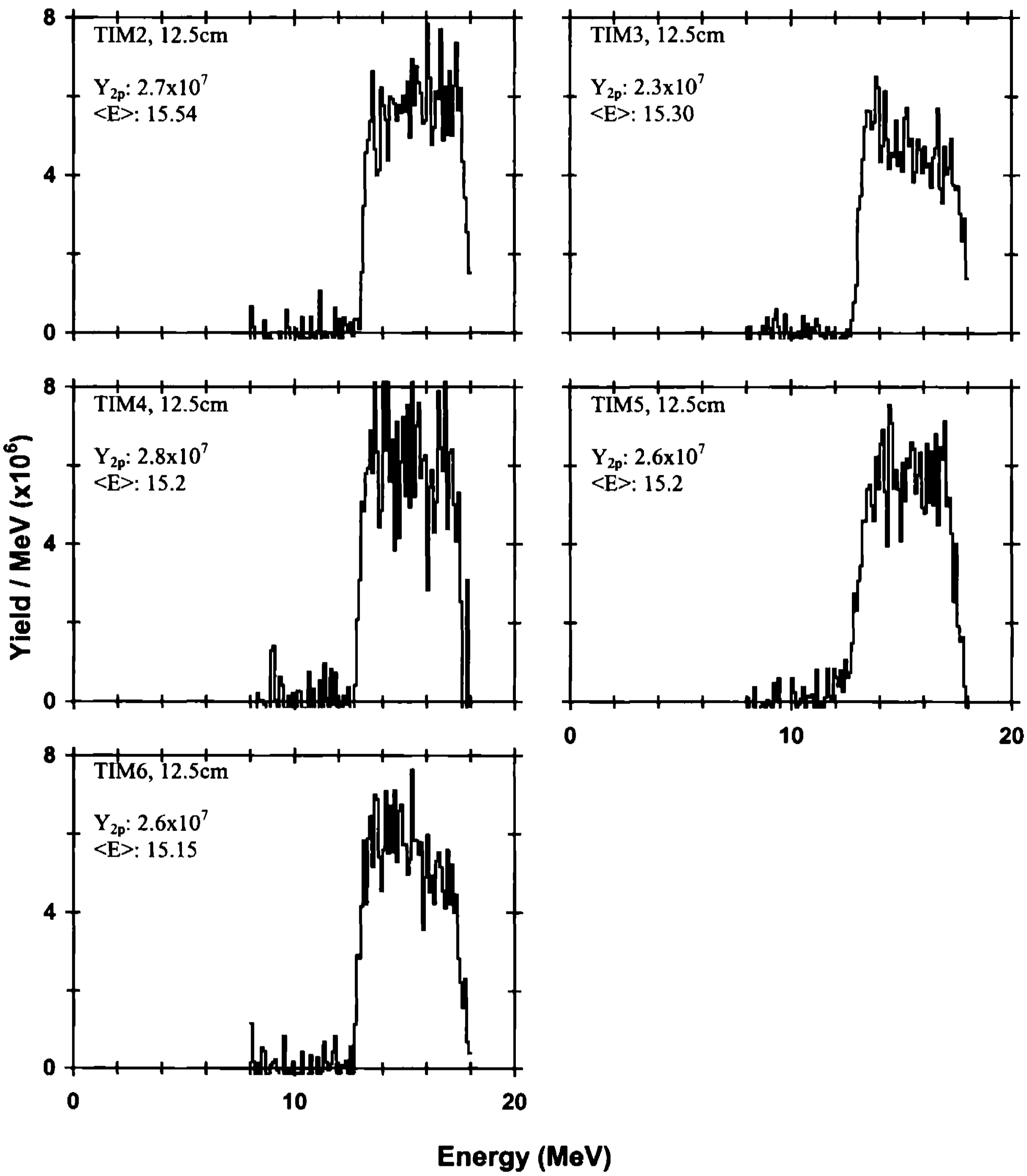

Shot #	Target	On-Target Energy (kJ)	Pulse Shape	Y_{1n} ($x10^{11}$)	$<T_i>_{Y1n}$ (keV)	Bang Time (ps)	Burn Width (ps)
29831	D_2(15) SiO_2[3.3] 925 μm	22.9	SSD: SG1018	4.5 +/- 0.9	6.1 +/- 0.5	Not Available	Not Available

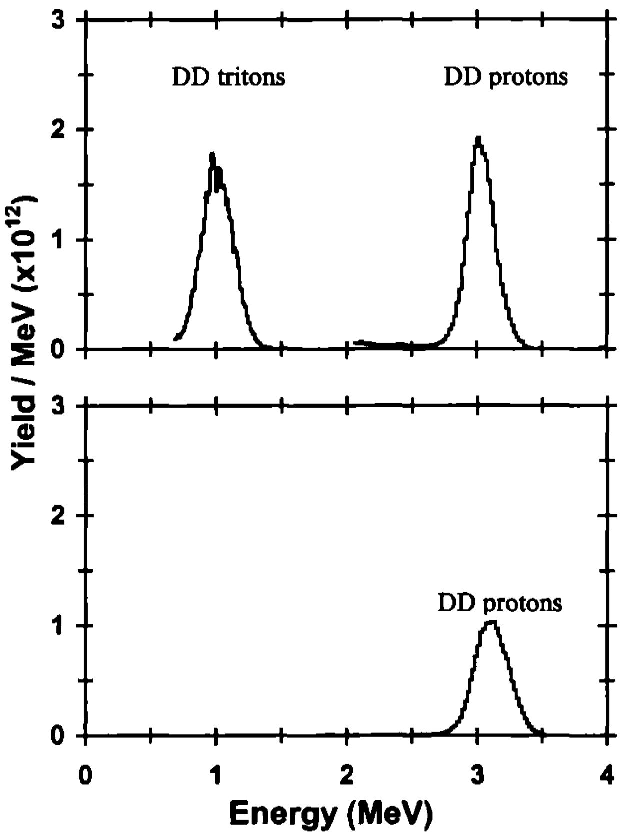

CPS-1 (1mm slit)

DD protons	
Yield (Gaussian):	(5.0 ± 0.5) x10^{11}
<E> (Gaussian):	3.03 ± 0.02 MeV
σ (Gaussian):	0.11
$<T_i>$:	7.7 keV
DD tritons	
Yield (Gaussian):	(5.0 ± 0.5) x10^{11}
<E> (Gaussian):	1.01 ± 0.02 MeV
σ (Gaussian):	0.12
$<T_i>$:	9.5 keV

CPS-2 (1mm slit)

DD protons	
Yield (Gaussian):	3.4 x10^{11}
<E> (Gaussian):	3.11 MeV
σ (Gaussian):	0.13
$<T_i>$:	10.9 keV

Note: DD proton yield from CPS-2 is lower than yield from CPS-1 because of track overlap problem.

Shot #	$\langle Y_{2p} \rangle$ ($x10^8$)	Y_{2n} ($x10^8$)	$\rho R_{hot,\,2p,\,hot\text{-}spot}$ (mg/cm^2)	$\rho R_{hot,\,2n,\,hot\text{-}spot}$ (mg/cm^2)	$\rho R_{hot,\,2p,\,uniform}$ (mg/cm^2)	$\rho R_{hot,\,2n,\,uniform}$ (mg/cm^2)	$\langle E_{2p} \rangle$ (MeV)	ρR_{total} (mg/cm^2)
29831	2.7 +/- 0.3	1.6 +/- 0.2	5.3 + 0.7 - 1.0	5.3 + 0.7 - 1.0	7.0 + 1.0 - 1.4	7.0 + 1.0 - 1.4	14.85 +/- 0.1	N/A

Secondary proton spectra from WRF

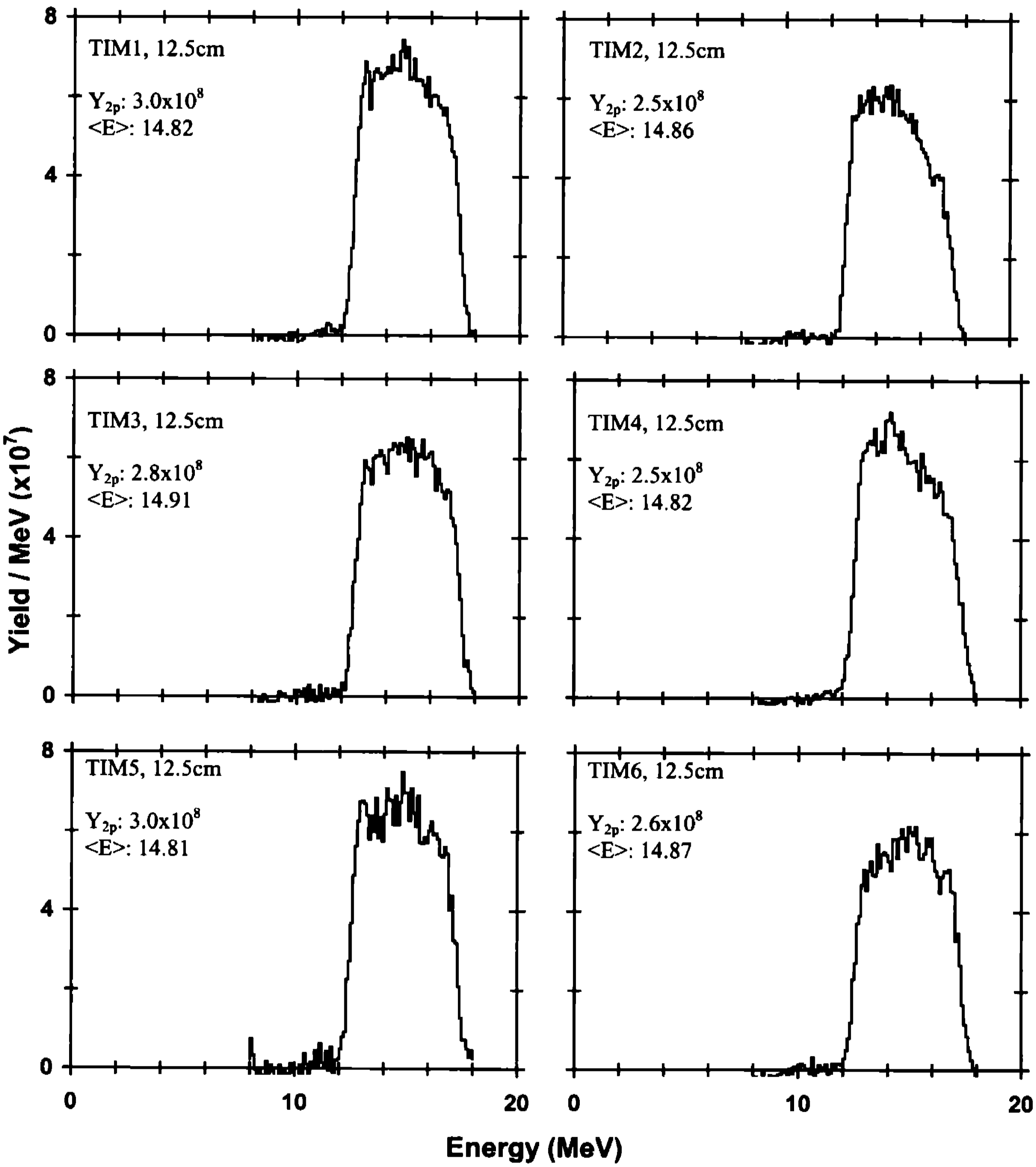

Shot #	Target	On-Target Energy (kJ)	Pulse Shape	Y_{1n} ($x10^{11}$)	$<T_i>_{Y1n}$ (keV)	Bang Time (ps)	Burn Width (ps)
29833	D_2(15) SiO_2[2.6] 912 μm	22.7	SSD: SG1018	4.1 +/- 0.8	7.0 +/- 0.5	900 +/- 50	160 +/- 25

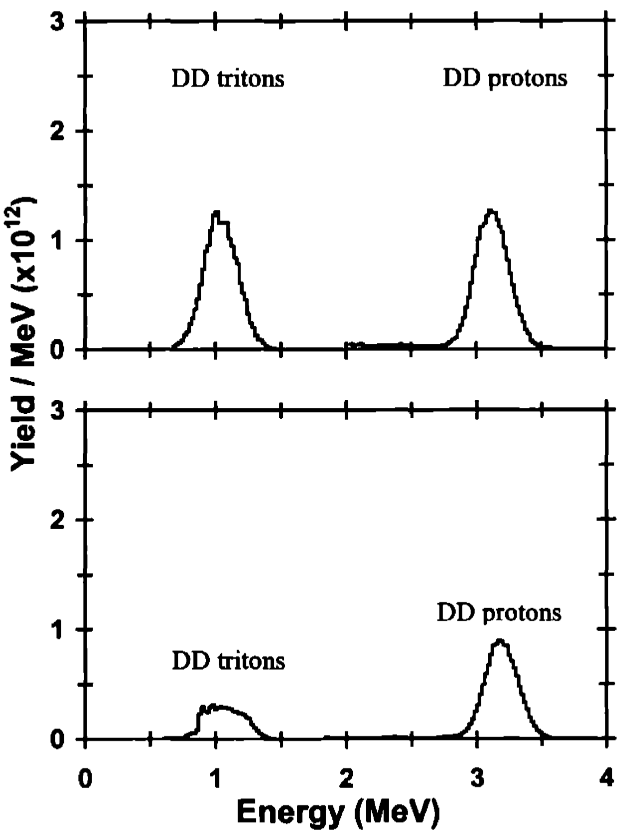

CPS-1 (1mm slit)

DD protons

Yield (Gaussian):	(4.2 ± 0.4) x10^{11}
<E> (Gaussian):	3.12 ± 0.02 MeV
σ (Gaussian):	0.13
$<T_i>$:	10.9 keV

DD tritons

Yield (Gaussian):	(3.9 ± 0.4) x10^{11}
<E> (Gaussian):	1.04 ± 0.02 MeV
σ (Gaussian):	0.13
$<T_i>$:	11.0 keV

CPS-2 (1mm slit)

DD protons

Yield (Gaussian):	2.8x10^{11}
<E> (Gaussian):	3.10 MeV
σ (Gaussian):	0.13
$<T_i>$:	

DD tritons

Yield :	1.2 x10^{11}
<E>:	1.07 MeV
standard deviation:	0.14

Note: DD proton and triton yields from CPS-2 is lower than yields from CPS-1 because of track overlap problem.

Shot #	$\langle Y_{2p} \rangle$ ($x10^8$)	Y_{2n} ($x10^8$)	$\rho R_{hot,\,2p,}$ hot-spot (mg/cm^2)	$\rho R_{hot,\,2n,}$ hot-spot (mg/cm^2)	$\rho R_{hot,\,2p,}$ uniform (mg/cm^2)	$\rho R_{hot,\,2n,}$ uniform (mg/cm^2)	$\langle E_{2p} \rangle$ (MeV)	ρR_{total} (mg/cm^2)
29833	1.1 +/- 0.1	1.2 +/- 0.2	2.2 + 0.3 - 0.4	4.2 + 0.6 - 1.1	2.9 + 0.4 - 0.6	5.6 + 0.8 - 1.1	15.09 +/- 0.1	N/A

Secondary proton spectra from WRF

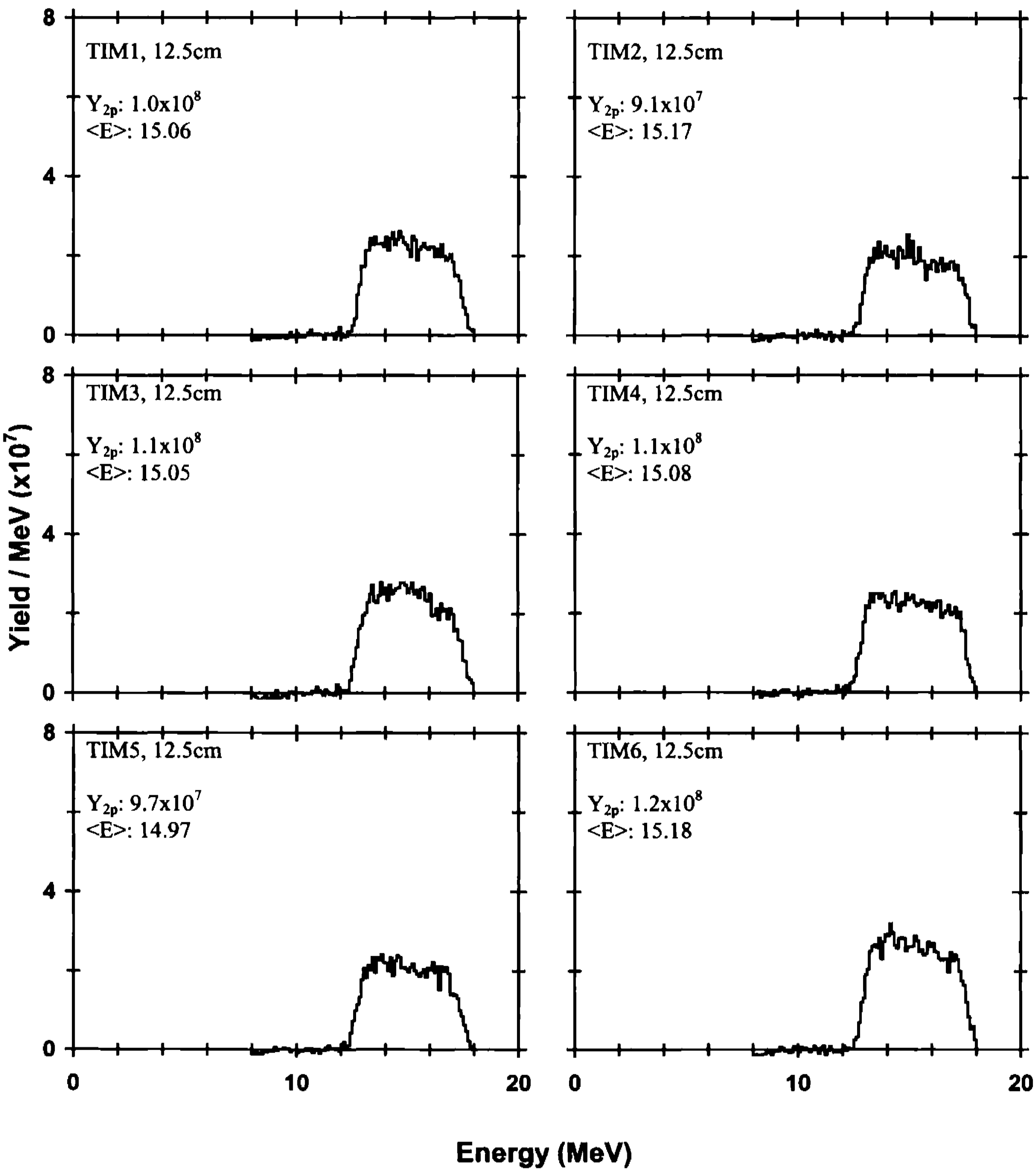

Shot #	Target	On-Target Energy (kJ)	Pulse Shape	Y_{1n} ($x10^{11}$)	$<T_i>_{Y1n}$ (keV)	Bang Time (ps)	Burn Width (ps)
30979	D_2(14.7) SiO_2[2.9] 911 μm	20.5	SSD: SG0801	3.9 +/- 0.8	8.3 +/- 0.5	900 +/- 50	160 +/- 25

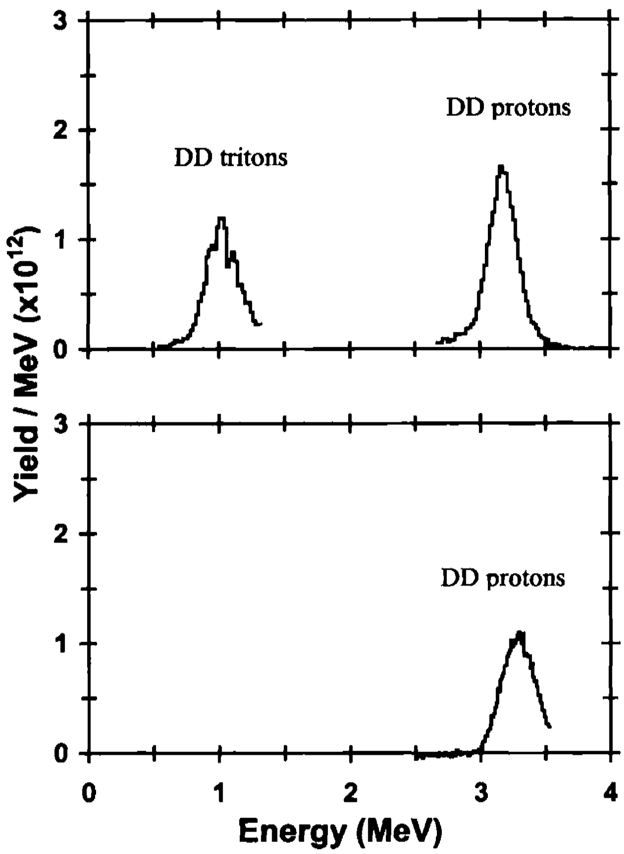

CPS-1 (1mm slit)

DD protons
Yield (Gaussian): (5.0 ± 0.5) $x10^{11}$
<E> (Gaussian): 3.03 ± 0.02 MeV
σ (Gaussian): 0.11
DD tritons
Yield: (5.0 ± 0.5) $x10^{11}$
<E>: 1.01 ± 0.02 MeV
standard deviation: 0.12

CPS-2 (1mm slit)

DD protons
Yield (Gaussian): 3.4 $x10^{11}$
<E> (Gaussian): 3.11 MeV
σ (Gaussian): 0.13

Note: DD proton yield from CPS-2 is lower than yield from CPS-1 because of track overlap problem.

Shot #	$\langle Y_{2p} \rangle$ ($x10^8$)	Y_{2n} ($x10^7$)	$\rho R_{hot,\,2p,}$ hot-spot (mg/cm^2)	$\rho R_{hot,\,2n,}$ hot-spot (mg/cm^2)	$\rho R_{hot,\,2p,}$ uniform (mg/cm^2)	$\rho R_{hot,\,2n,}$ uniform (mg/cm^2)	$\langle E_{2p} \rangle$ (MeV)	ρR_{total} (mg/cm^2)
30979	1.3 +/- 0.1	9.0 +/- 1.4	2.7 + 0.4 - 0.5	3.2 + 0.4 - 0.6	3.6 + 0.5 - 0.7	4.2 + 0.6 - 0.8	15.03 +/- 0.1	N/A

Secondary proton spectra from WRF

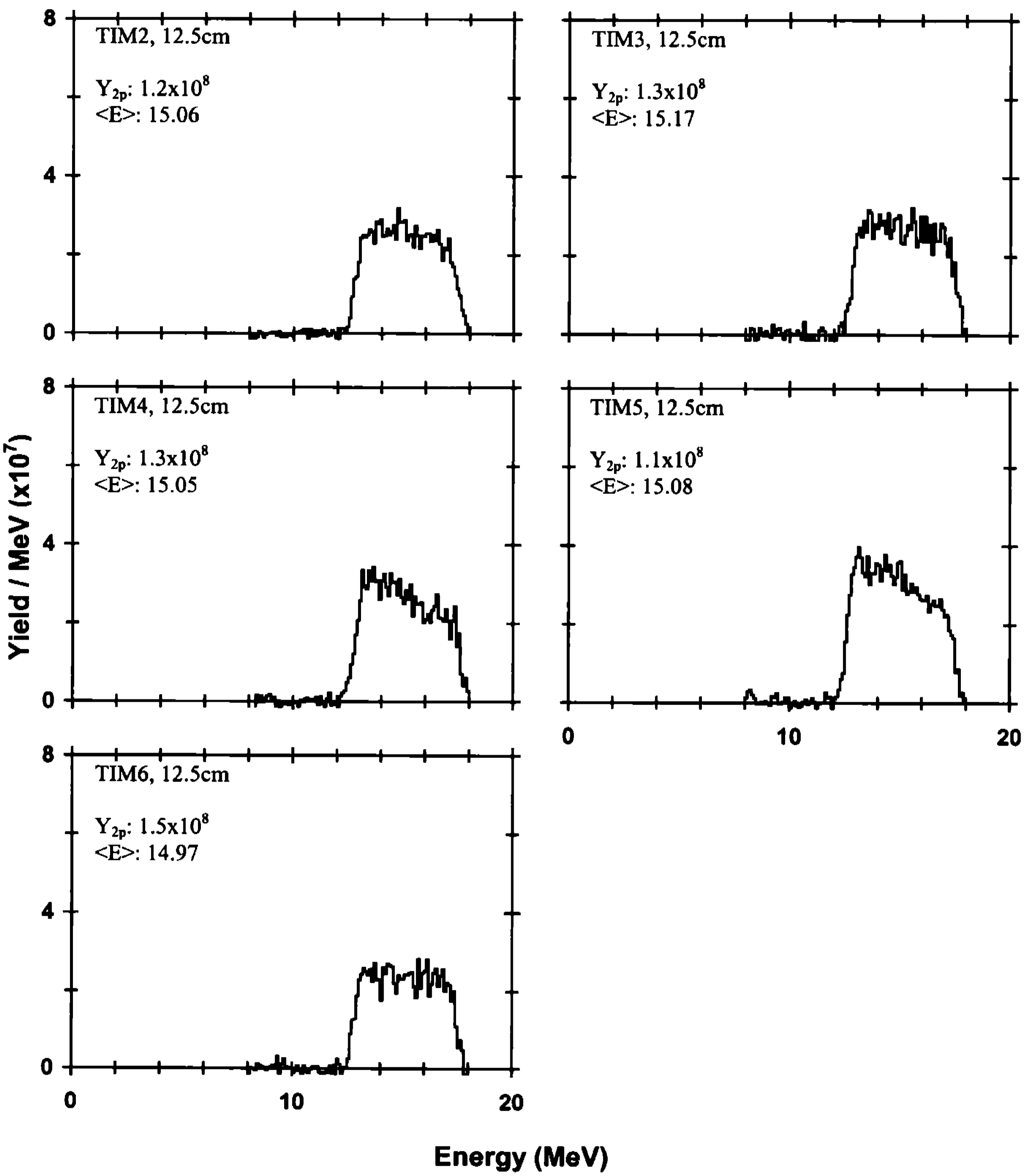

Shot #	Target	On-Target Energy (kJ)	Pulse Shape	Y_{1n} ($x10^{11}$)	$<T_i>_{Y1n}$ (keV)	Bang Time (ps)	Burn Width (ps)
30980	D_2(14.7) SiO_2[2.9] 931	13.2	SSD: SG0801	2.9 +/- 0.6	6.2 +/- 0.5	1050 +/- 50	170 +/- 25

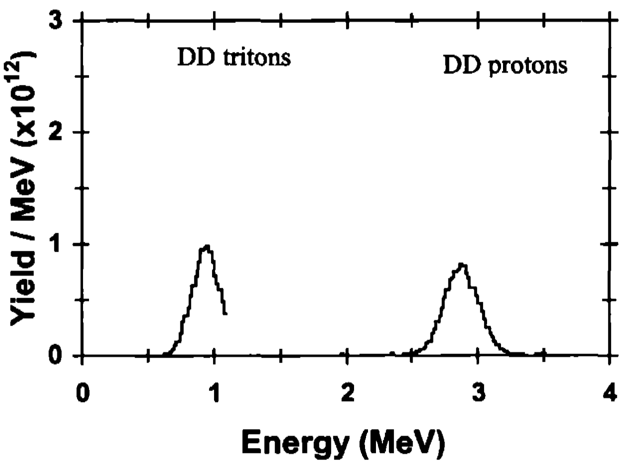

CPS-2 (0.5mm slit)

DD protons

Yield (Gaussian):	(2.6 ± 0.3) x10^{11}
<E> (Gaussian):	2.87 ± 0.02 MeV
σ (Gaussian):	0.14
$<T_i>$:	12.7 keV

DD tritons

Yield (Gaussian):	(2.5 ± 0.3) x10^{11}
<E> (Gaussian):	0.94 ± 0.02 MeV
σ (Gaussian):	0.1
$<T_i>$:	6.5 keV

Note: No CPS-1 data

Shot #	$\langle Y_{2p} \rangle$ ($x10^8$)	Y_{2n} ($x10^8$)	$\rho R_{hot,\ 2p,}$ hot-spot (mg/cm^2)	$\rho R_{hot,\ 2n,}$ hot-spot (mg/cm^2)	$\rho R_{hot,\ 2p,}$ uniform (mg/cm^2)	$\rho R_{hot,\ 2n,}$ uniform (mg/cm^2)	$\langle E_{2p} \rangle$ (MeV)	ρR_{total} (mg/cm^2)
30980	2.2 +/- 0.2	1.5 +/- 0.2	5.0 + 0.7 - 1.0	5.9 + 0.8 - 1.2	6.5 + 0.9 - 1.3	7.8 + 1.1 - 1.5	14.68 +/- 0.1	N/A

Secondary proton spectra from WRF

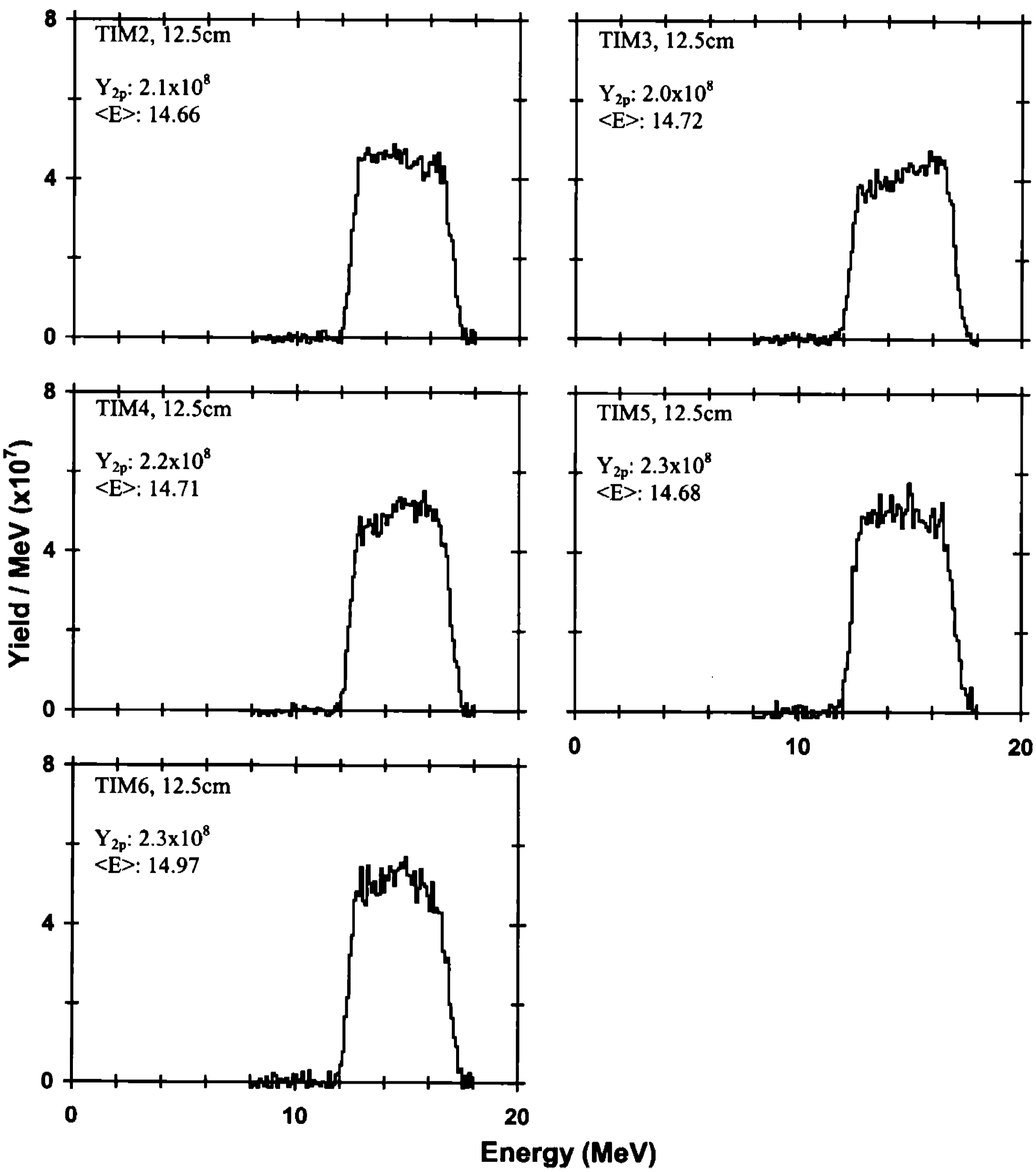

Shot #	Target	On-Target Energy (kJ)	Pulse Shape	Y_{1n} ($x10^{11}$)	$<T_i>_{Y1n}$ (keV)	Bang Time (ps)	Burn Width (ps)
30981	D_2(14.7) SiO_2[3.1] 927	13.1	SSD: SG0801	1.5 +/- 0.2	8.2 +/- 0.5	1090 +/- 50	160 +/- 25

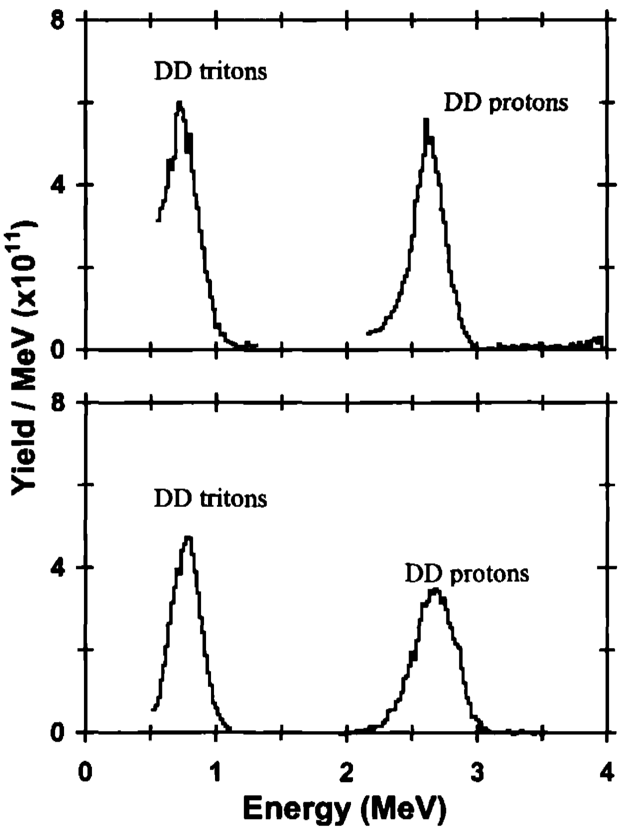

CPS-1 (1mm slit)

DD protons

Yield (Gaussian):	$(1.5 \pm 0.2) \times 10^{11}$
<E> (Gaussian):	2.63 ± 0.02 MeV
σ (Gaussian):	0.12
$<T_i>$:	9.2 keV

DD tritons

Yield (Gaussian):	$(1.9 \pm 0.2) \times 10^{11}$
<E> (Gaussian):	0.73 ± 0.02 MeV
σ (Gaussian):	0.14
$<T_i>$:	12.8 keV

CPS-2 (1mm slit)

DD protons

Yield (Gaussian):	$(1.4E \pm 0.1) \times 10^{11}$
<E> (Gaussian):	2.67 ± 0.02 MeV
σ (Gaussian):	0.16
$<T_i>$:	16.7 keV

DD tritons

Yield (Gaussian):	$(1.3 \pm 0.1) \times 10^{11}$
<E> (Gaussian):	0.77 ± 0.02 MeV
σ (Gaussian):	0.11
$<T_i>$:	7.9 keV

Shot #	$\langle Y_{2p} \rangle$ ($\times 10^8$)	Y_{2n} ($\times 10^7$)	$\rho R_{hot,\,2p,}$ hot-spot (mg/cm^2)	$\rho R_{hot,\,2n,}$ hot-spot (mg/cm^2)	$\rho R_{hot,\,2p,}$ uniform (mg/cm^2)	$\rho R_{hot,\,2n,}$ uniform (mg/cm^2)	$\langle E_{2p} \rangle$ (MeV)	ρR_{total} (mg/cm^2)
30981	1.2 +/- 0.1	7.9 +/- 1.3	4.3 + 0.6 - 0.8	4.6 + 0.6 - 0.9	5.6 + 0.8 - 1.1	6.1 + 0.8 - 1.2	14.57 +/- 0.1	12.9

Secondary proton spectra from WRF

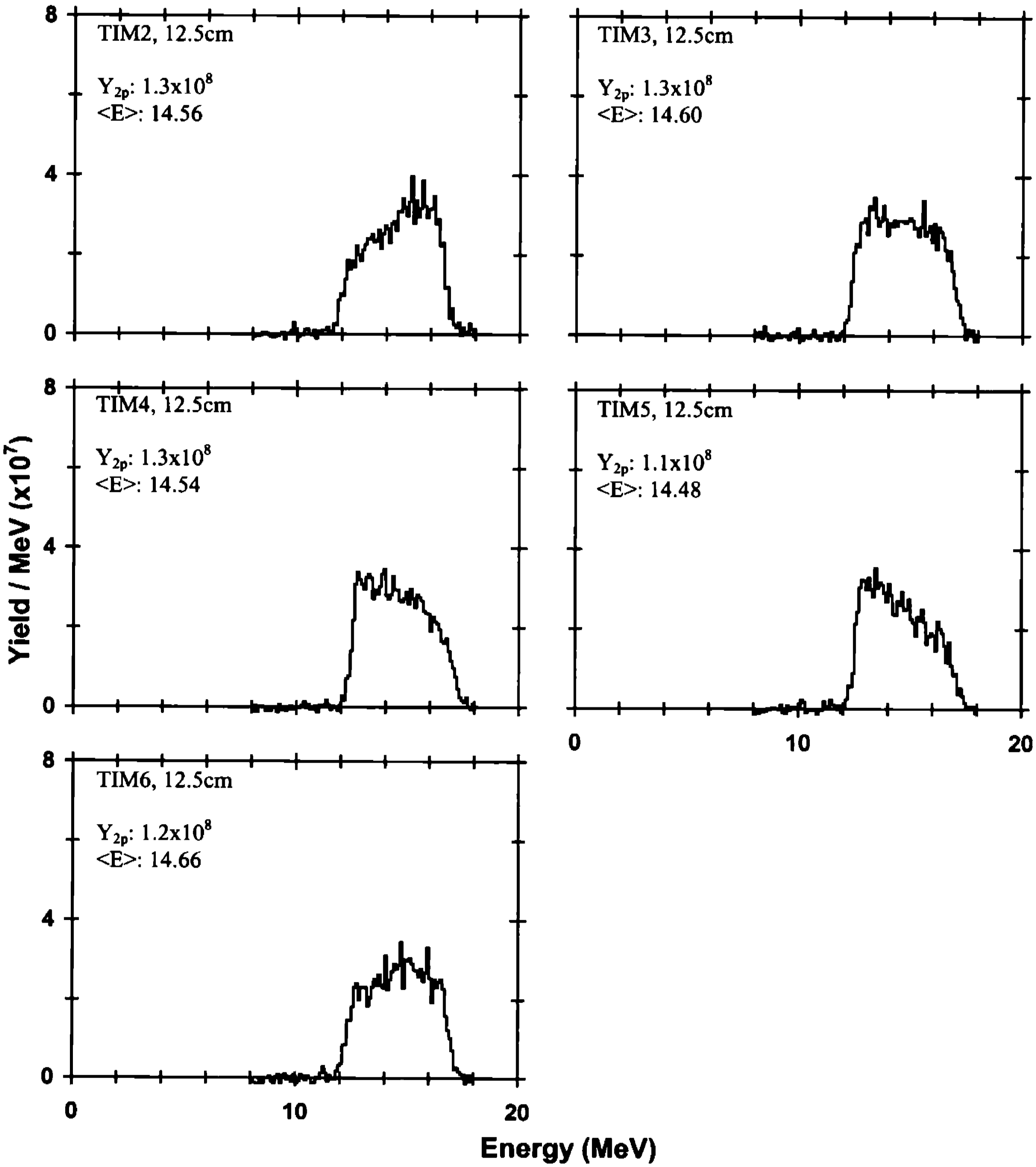

Shot #	Target	On-Target Energy (kJ)	Pulse Shape	Y_{1n} ($x10^{11}$)	$<T_i>_{Y1n}$ (keV)	Bang Time (ps)	Burn Width (ps)
30982	D_2(14.7) SiO_2[3.0] 915	12.9	SSD: SG0801	1.7 +/- 0.2	6.6 +/- 0.5	1070 +/- 50	160 +/- 25

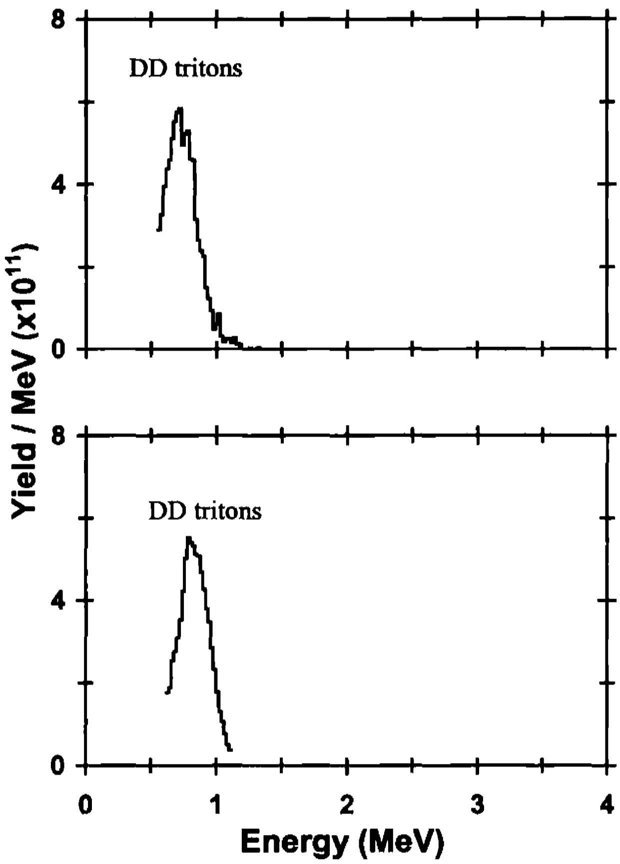

CPS-1 (0.5mm slit)

DD tritons

Yield (Gaussian):	(1.7 ± 0.2) x10^{11}
<E> (Gaussian):	0.72 ± 0.02 MeV
σ (Gaussian):	0.12
$<T_i>$:	9.4 keV

CPS-2 (0.5mm slit)

DD tritons

Yield (Gaussian):	(1.7 ± 0.2) x10^{11}
<E> (Gaussian):	0.83 ± 0.02 MeV
σ (Gaussian):	0.12
$<T_i>$:	9.4 keV

Note: Both CR-39 were etched for only two hours because track density is very high. DD proton tracks are too small to be scanned because of that.

Shot #	$<Y_{2p}>$ (x10^8)	Y_{2n} (x10^7)	$\rho R_{hot, 2p,}$ hot-spot (mg/cm^2)	$\rho R_{hot, 2n,}$ hot-spot (mg/cm^2)	$\rho R_{hot, 2p,}$ uniform (mg/cm^2)	$\rho R_{hot, 2n,}$ uniform (mg/cm^2)	$<E_{2p}>$ (MeV)	ρR_{total} (mg/cm^2)
30982	1.1 +/- 0.1	7.3 +/- 1.2	3.4 + 0.5 - 0.7	4.0 + 0.6 - 0.8	4.5 + 0.6 - 0.9	5.3 + 0.7 - 1.0	14.64 +/- 0.1	10.7

Secondary proton spectra from WRF

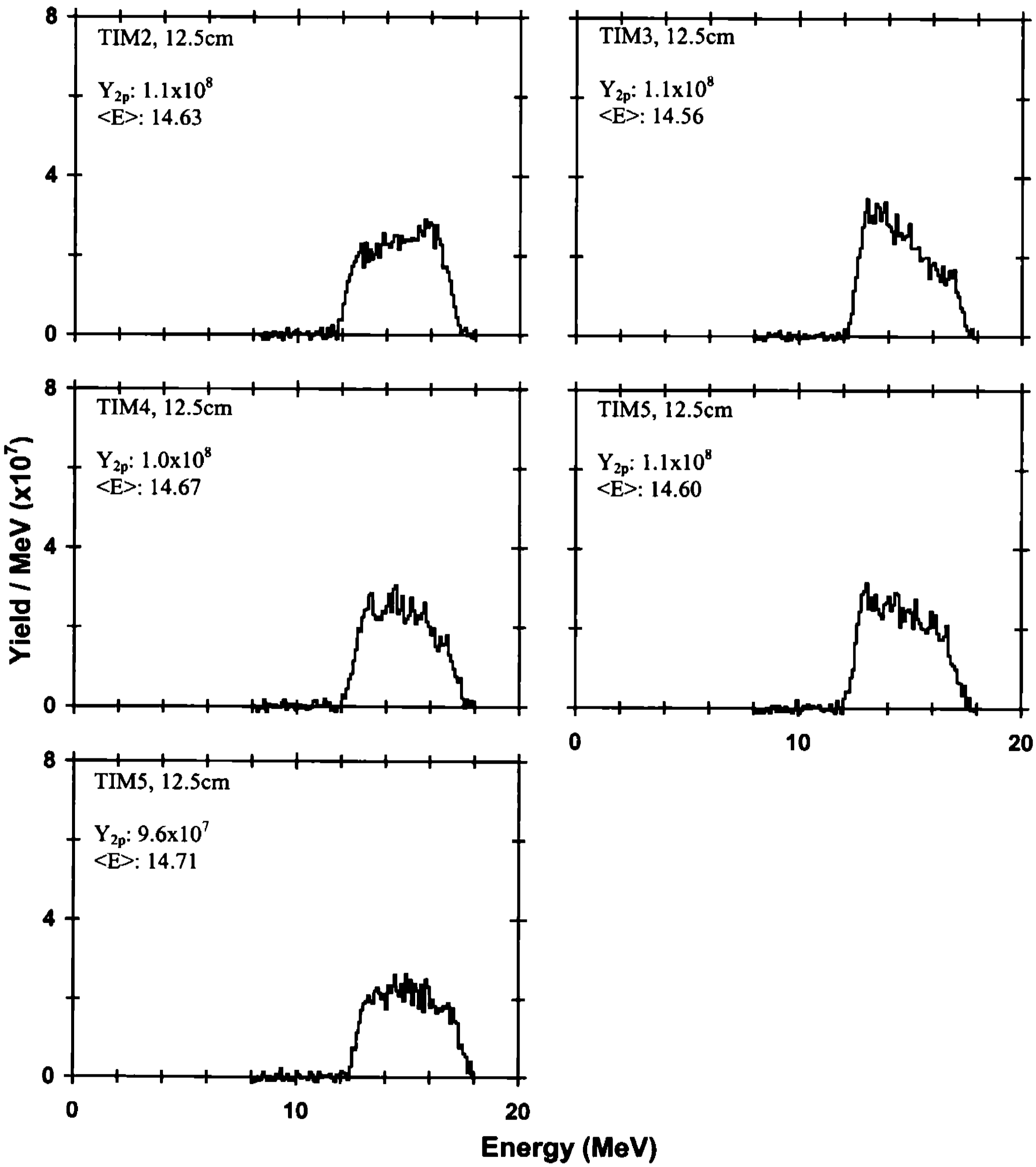

Shot #	Target	On-Target Energy (kJ)	Pulse Shape	Y_{1n} ($x10^{11}$)	$<T_i>_{Y1n}$ (keV)	Bang Time (ps)	Burn Width (ps)
30983	D_2(14.7) SiO_2[2.9] 912	11.5	SSD: SG0801	1.7 +/- 0.2	5.9 +/- 0.5	1060 +/- 50	170 +/- 25

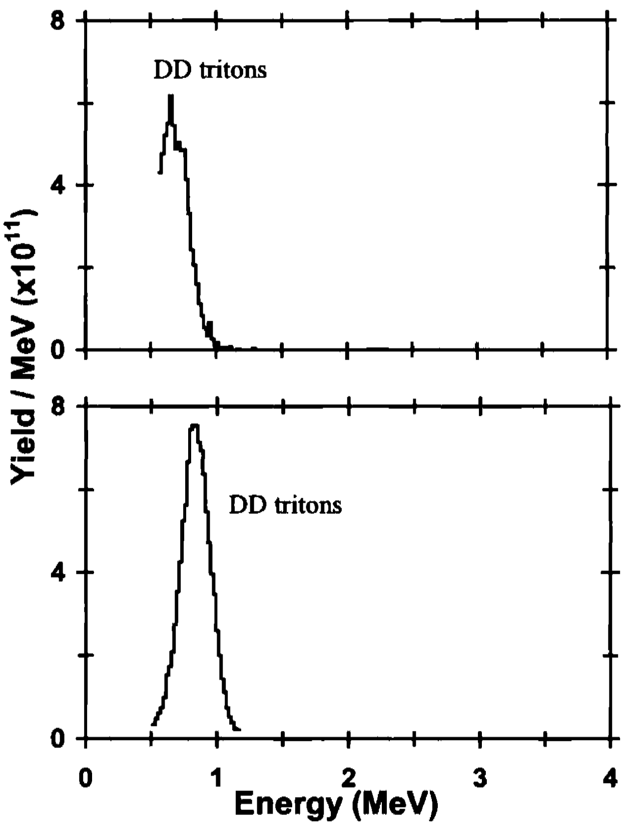

CPS-1 (0.5mm slit)

DD tritons

Yield (Gaussian):	(1.5 ± 0.2) x10^{11}
<E> (Gaussian):	0.68 ± 0.02 MeV
σ (Gaussian):	0.10
<Ti>:	6.5 keV

CPS-2 (0.5mm slit)

DD tritons

Yield (Gaussian):	(2.1 ± 0.2) x10^{11}
<E> (Gaussian):	0.84 ± 0.02 MeV
σ (Gaussian):	0.11
<Ti>:	7.9 keV

Note: Both CR-39 were etched for only two hours because track density is very high. DD proton tracks are too small to be scanned because of that.

Shot #	$\langle Y_{2p} \rangle$ ($x10^8$)	Y_{2n} ($x10^7$)	$\rho R_{hot, 2p,}$ hot-spot (mg/cm^2)	$\rho R_{hot, 2n,}$ hot-spot (mg/cm^2)	$\rho R_{hot, 2p,}$ uniform (mg/cm^2)	$\rho R_{hot, 2n,}$ uniform (mg/cm^2)	$\langle E_{2p} \rangle$ (MeV)	ρR_{total} (mg/cm^2)
30983	1.2 +/- 0.1	6.3 +/- 1.1	3.9 + 0.5 - 0.7	3.4 + 0.5 - 0.7	5.1 + 0.7 - 1.0	4.6 + 0.6 - 0.9	14.62 +/- 0.1	11.3

Secondary proton spectra from WRF

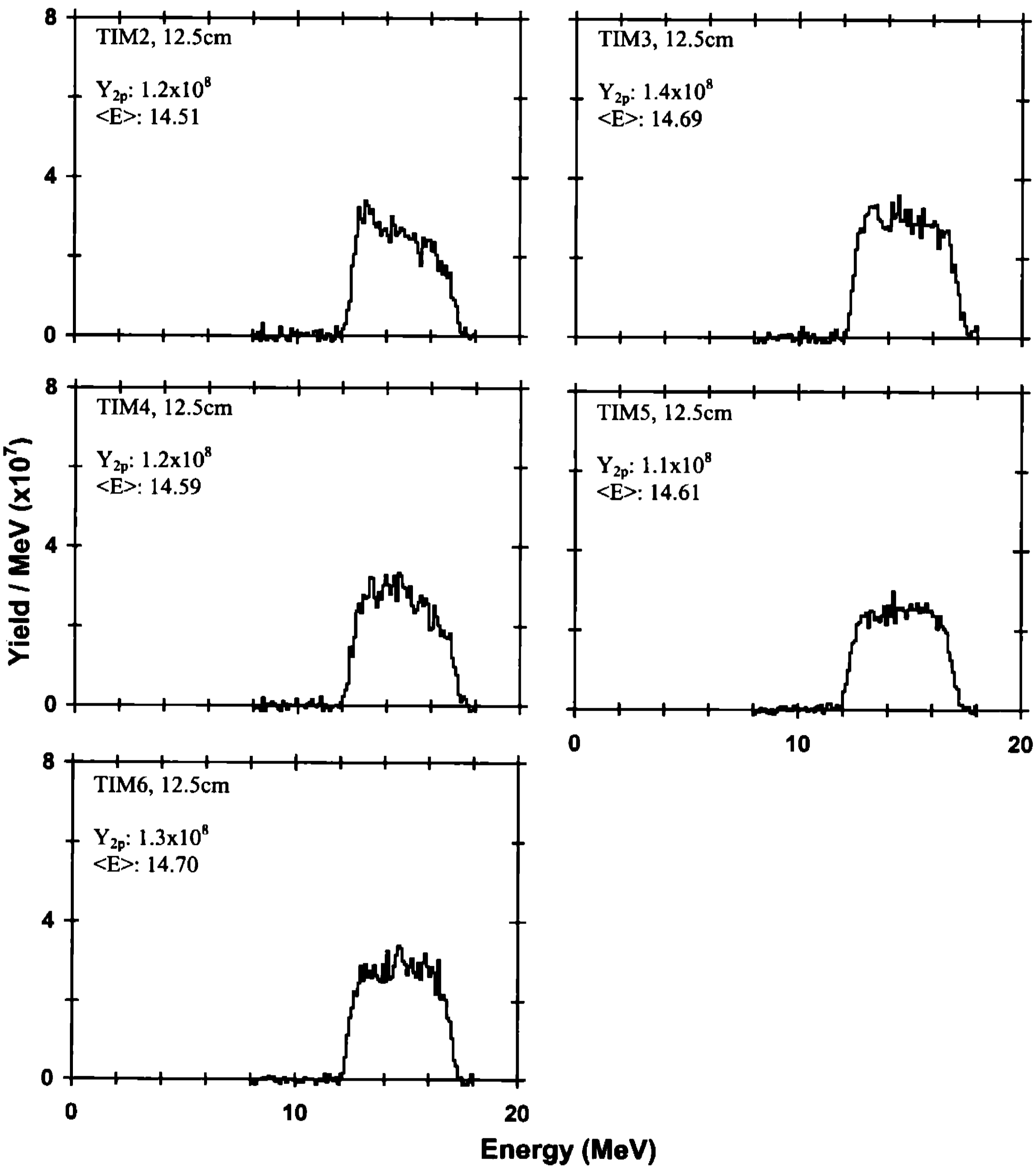

Shot #	Target	On-Target Energy (kJ)	Pulse Shape	Y_{1n} ($x10^{11}$)	$<T_i>_{Y1n}$ (keV)	Bang Time (ps)	Burn Width (ps)
30984	D_2(14.7) SiO_2[2.4] 927	11.1	SSD: SG0801	2.3 +/- 0.5	6.3 +/- 0.5	920 +/- 50	160 +/- 25

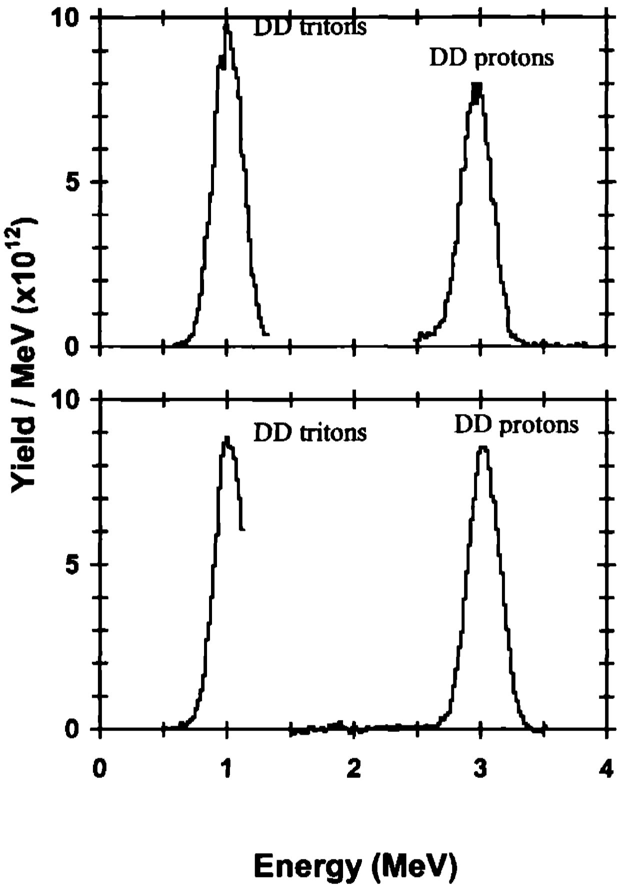

CPS-1 (1mm slit)

DD protons

Yield (Gaussian):	(2.9 ± 0.3) x10^{11}
<E> (Gaussian):	2.97 ± 0.02 MeV
σ (Gaussian):	0.13
$<T_i>$:	10.9 keV

DD tritons

Yield (Gaussian):	(2.7 ± 0.3) x10^{11}
<E> (Gaussian):	1.01 ± 0.02 MeV
σ (Gaussian):	0.11 ±
$<T_i>$:	7.9 keV

CPS-2 (1mm slit)

DD protons

Yield (Gaussian):	(2.7 ± 0.3) x10^{11}
<E> (Gaussian):	3.02 ± 0.02 MeV
σ (Gaussian):	0.12
$<T_i>$:	9.2 keV

DD tritons

Yield (Gaussian):	(2.5 ± 0.3) x10^{11}
<E> (Gaussian):	1.02 ± 0.02 MeV
σ (Gaussian):	0.11
$<T_i>$:	7.9 keV

Shot #	$<Y_{2p}>$ $(x10^8)$	Y_{2n} $(x10^7)$	$\rho R_{hot, 2p,}$ hot-spot (mg/cm^2)	$\rho R_{hot, 2n,}$ hot-spot (mg/cm^2)	$\rho R_{hot, 2p,}$ uniform (mg/cm^2)	$\rho R_{hot, 2n,}$ uniform (mg/cm^2)	$<E_{2p}>$ (MeV)	ρR_{total} (mg/cm^2)
30984	1.4 +/- 0.1	5.2 +/- 0.9	3.4 + 0.5 - 0.7	2.3 + 0.3 - 0.5	4.5 + 0.6 - 0.9	3.0 + 0.4 - 0.6	14.72 +/- 0.1	N/A

Secondary proton spectra from WRF

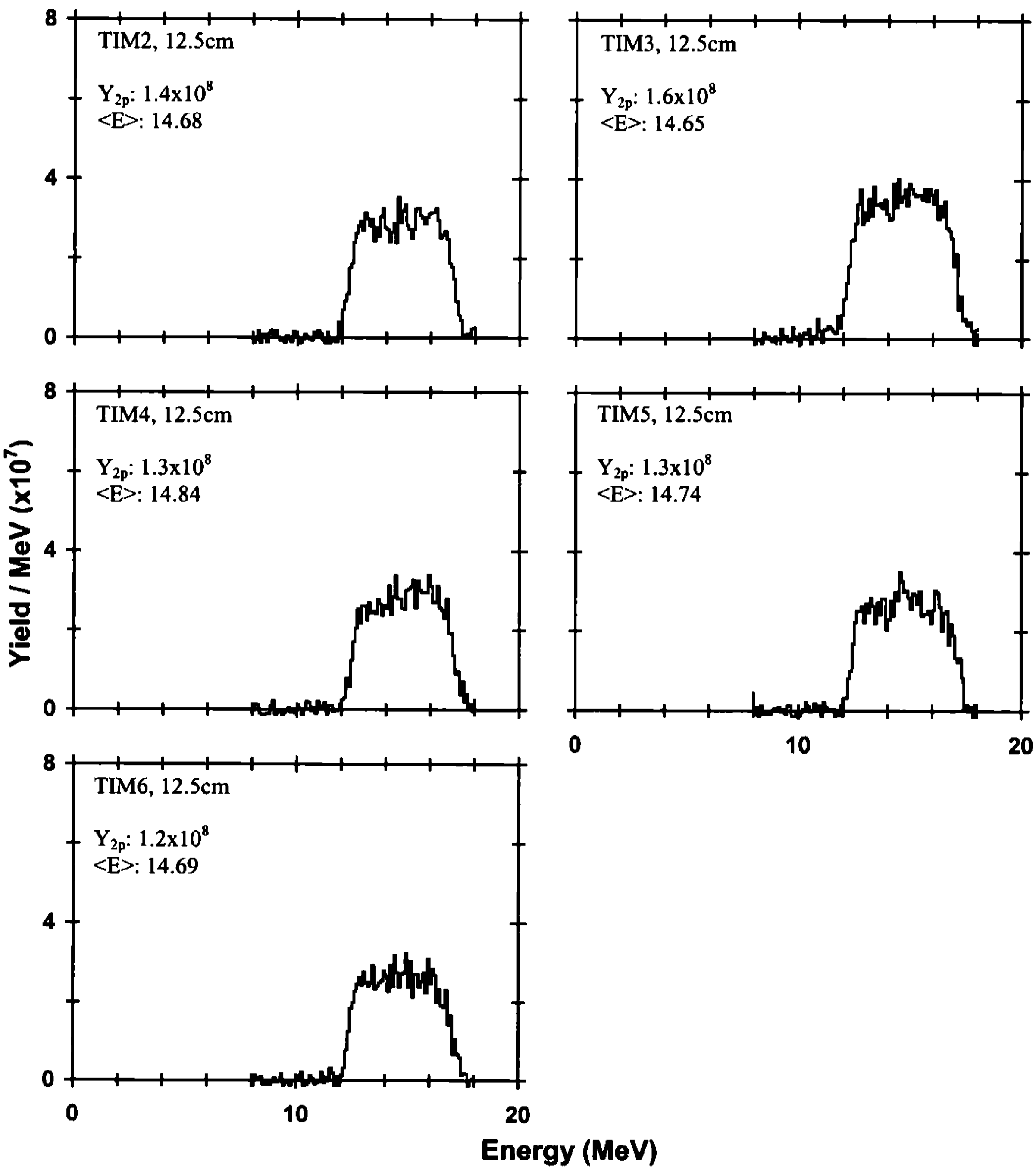

Shot #	Target	On-Target Energy (kJ)	Pulse Shape	Y_{1n} ($\times10^{11}$)	$\langle T_i \rangle_{Y1n}$ (keV)	Bang Time (ps)	Burn Width (ps)
30985	D_2(14.7) SiO_2[2.3] 909	11.0	SSD: SG0801	2.0 +/- 0.4	8.5 +/- 0.5	970 +/- 50	170 +/- 25

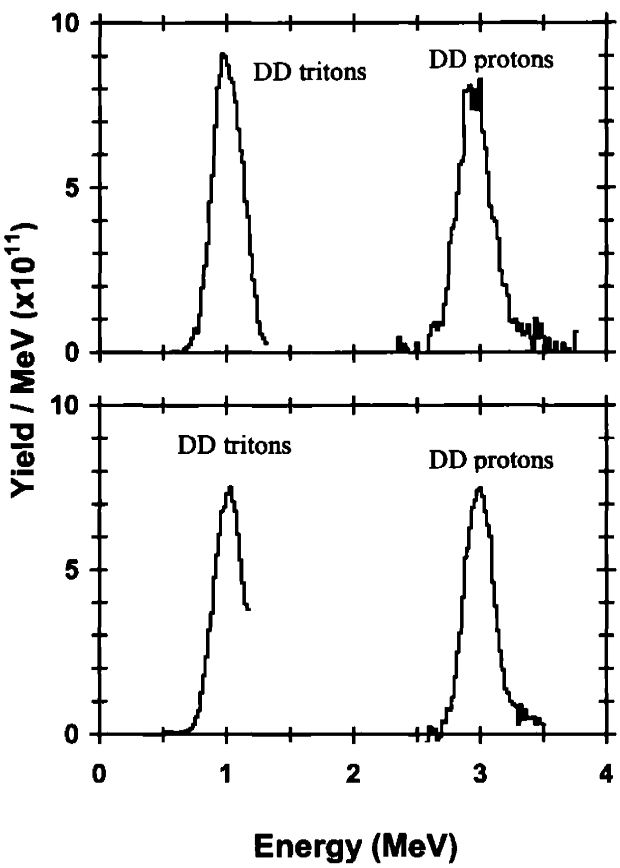

CPS-1 (0.5mm slit)

DD protons

Yield (Gaussian):	$(2.7 \pm 0.3) \times10^{11}$
$\langle E \rangle$ (Gaussian):	2.95 ± 0.02 MeV
σ (Gaussian):	0.14
$\langle T_i \rangle$:	12.7 keV

DD tritons

Yield (Gaussian):	$(2.7 \pm 0.3) \times10^{11}$
$\langle E \rangle$ (Gaussian):	1.01 ± 0.02 MeV
σ (Gaussian):	0.12
$\langle T_i \rangle$:	9.4 keV

CPS-2 (0.5mm slit)

DD protons

Yield (Gaussian):	$(2.2 \pm 0.2) \times10^{11}$
$\langle E \rangle$ (Gaussian):	3.0 ± 0.02 MeV
σ (Gaussian):	0.12
$\langle T_i \rangle$:	9.2 keV

DD tritons

Yield (Gaussian):	$(2.1 \pm 0.2) \times10^{11}$
$\langle E \rangle$ (Gaussian):	1.02 ± 0.02 MeV
σ (Gaussian):	0.11
$\langle T_i \rangle$:	7.9 keV

Shot #	$\langle Y_{2p} \rangle$ ($x10^8$)	Y_{2n} ($x10^7$)	$\rho R_{hot, 2p,}$ hot-spot (mg/cm^2)	$\rho R_{hot, 2n,}$ hot-spot (mg/cm^2)	$\rho R_{hot, 2p,}$ uniform (mg/cm^2)	$\rho R_{hot, 2n,}$ uniform (mg/cm^2)	$\langle E_{2p} \rangle$ (MeV)	ρR_{total} (mg/cm^2)
30985	1.1 +/- 0.1	6.2 +/- 1.1	3.0 + 0.4 - 0.6	2.9 + 0.4 - 0.6	4.0 + 0.5 - 0.8	3.9 + 0.5 - 0.8	14.69 +/- 0.1	N/A

Secondary proton spectra from WRF

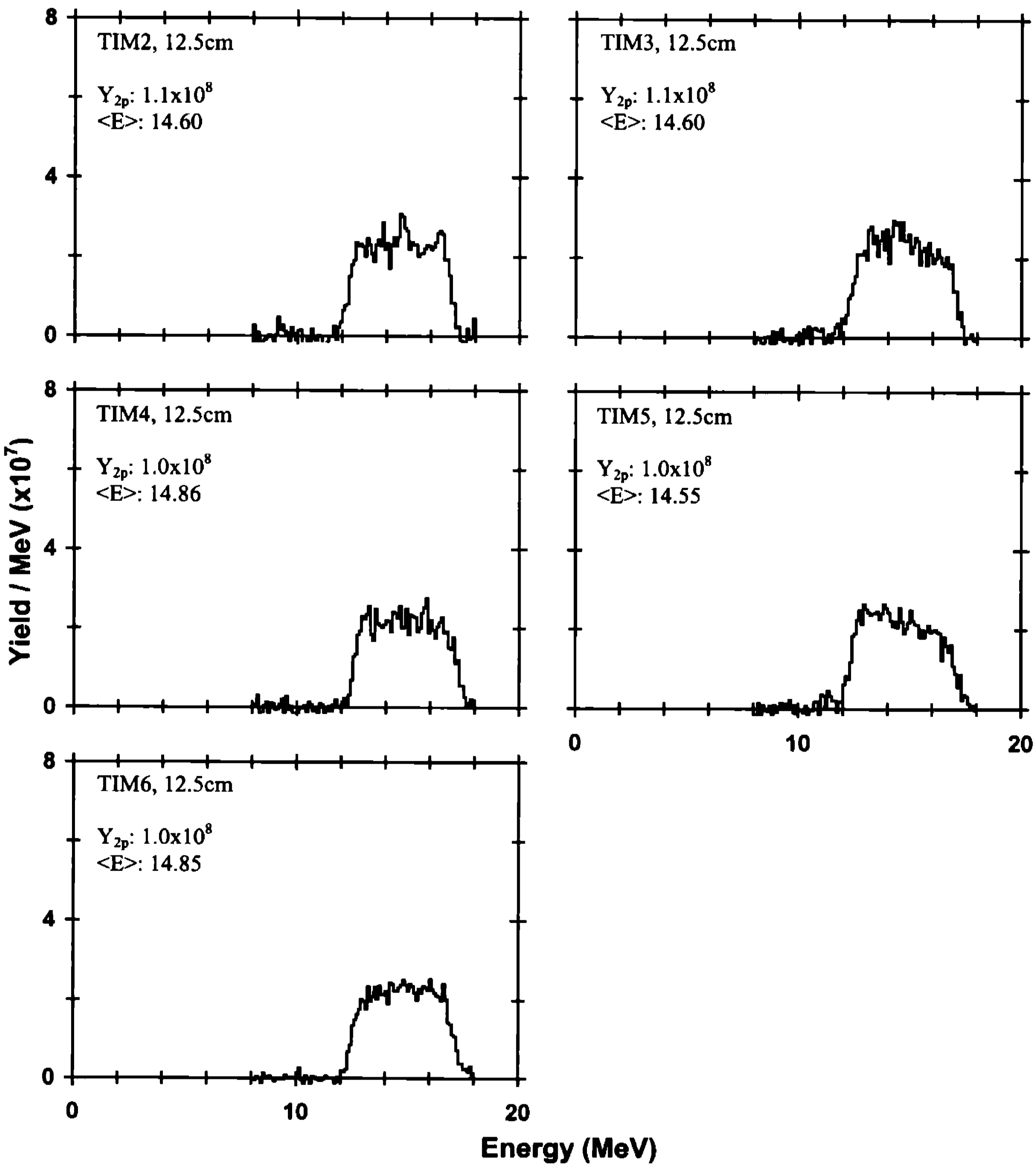

Summary of thick shell implosions

Shot #	Target	On-Target Energy (kJ)	Pulse Shape	Y_{1n} ($x10^{11}$)	$<T_i>_{Y1n}$ (keV)	Bang Time (ps)	Burn Width (ps)
27443	D2(15) CH[19.4] 934.8 μm	22.0	SSD: SG1018	1.5 +/- 0.2	4.1 +/- 0.5	1870 +/- 50	150 +/- 25

$<Y_{2p}>$ ($x10^8$)	Y_{2n} ($x10^8$)	$\rho R_{hot, 2p,}$ hot-spot (mg/cm^2)	$\rho R_{hot, 2n,}$ hot-spot (mg/cm^2)	$\rho R_{hot, 2p,}$ uniform (mg/cm^2)	$\rho R_{hot, 2n,}$ uniform (mg/cm^2)	$<E_{2p}>$ (MeV)	ρR_{total} (mg/cm^2)
1.5 +/- 0.2	2.3 +/- 0.3	5.0 +0.7 -1.0	12.8 +1.8 -2.6	6.8 +0.8 -0.7	16.4 +1.8 -2.7	13.1 +/- 0.1	57.1 +/- 2.9

Secondary proton spectra from WRF

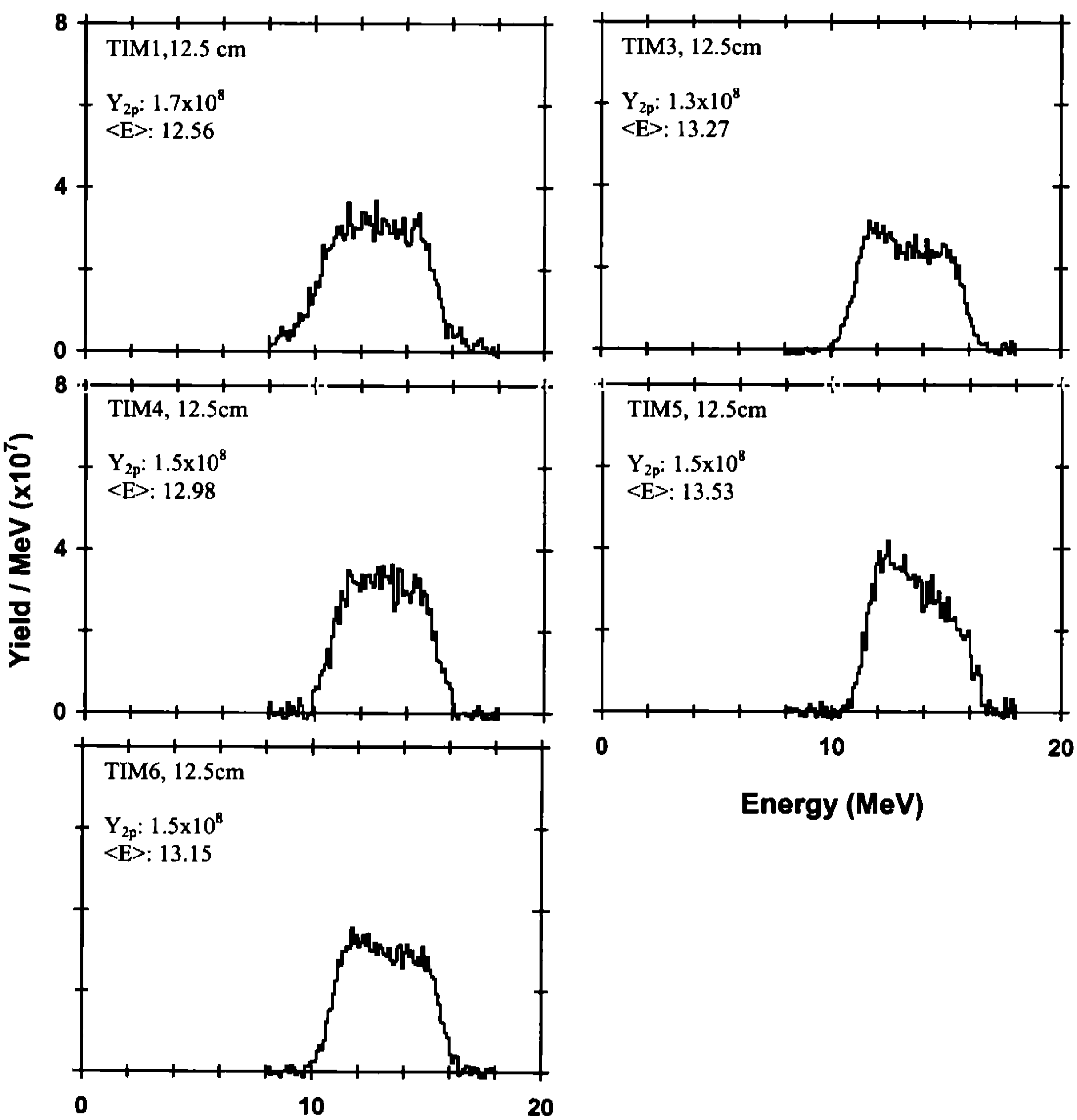

Shot #	Target	On-Target Energy (kJ)	Pulse Shape	Y_{1n} ($x10^{11}$)	$<T_i>_{Y1n}$ (keV)	Bang Time (ps)	Burn Width (ps)
27444	D2(15) CH[19.2] 935.4 μm	21.8	SSD: SG1018	1.1 +/- 0.1	4.7 +/- 0.5	1870 +/- 50	160 +/- 25

$<Y_{2p}>$ ($x10^7$)	Y_{2n} ($x10^8$)	$\rho R_{hot, 2p,}$ hot-spot (mg/cm^2)	$\rho R_{hot, 2n,}$ hot-spot (mg/cm^2)	$\rho R_{hot, 2p,}$ uniform (mg/cm^2)	$\rho R_{hot, 2n,}$ uniform (mg/cm^2)	$<E_{2p}>$ (MeV)	ρR_{total} (mg/cm^2)
6.8 +/- 1.0	1.1 +/- 0.2	3.3 +0.6 -0.8	9.0 +1.5 -2.1	4.2 +0.7 -1.0	11.4 +2.2 -3.1	13.55 +/- 0.1	44.0 +/- 2.9

Secondary proton spectra from WRF

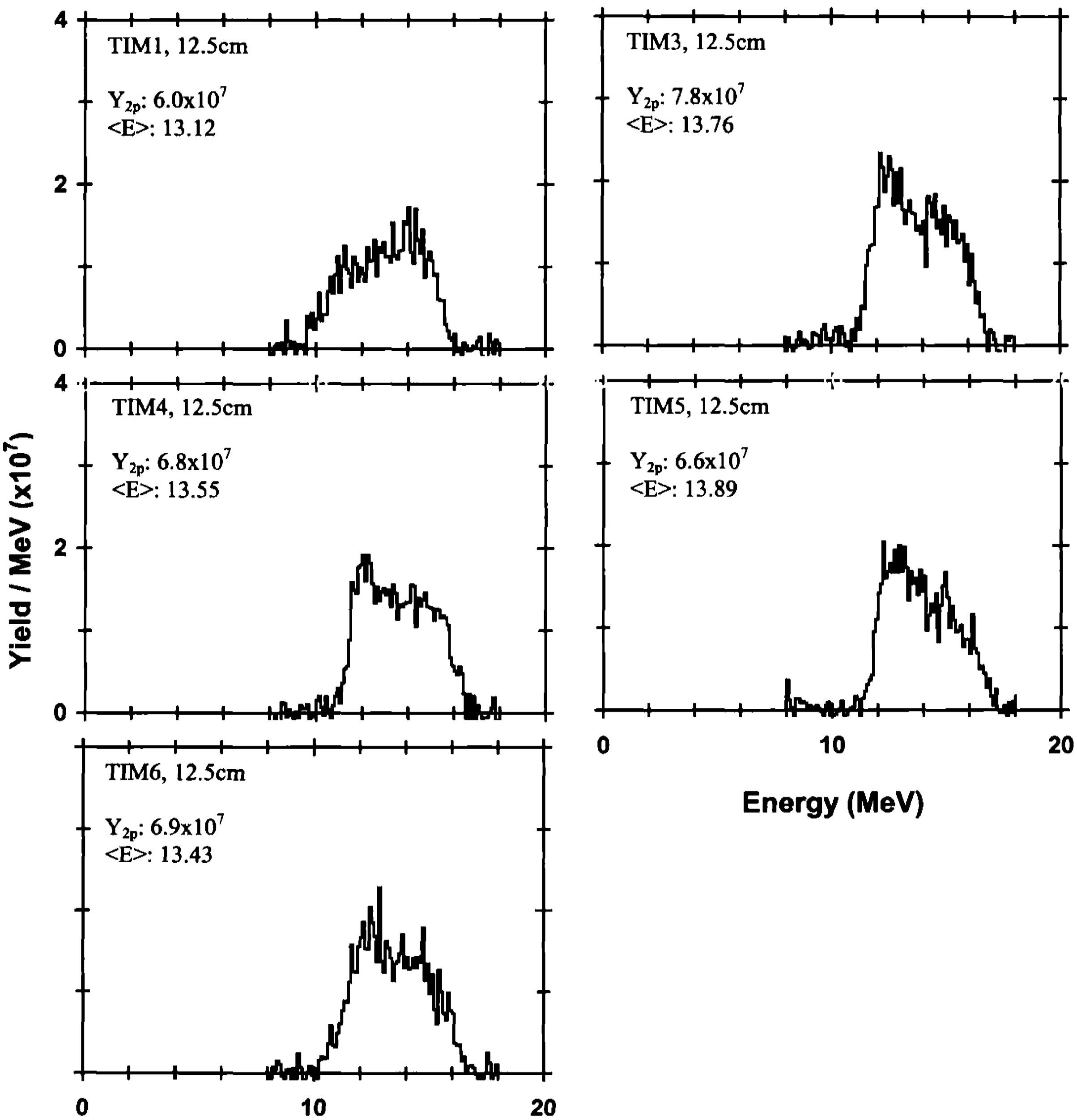

Shot #	Target	On-Target Energy (kJ)	Pulse Shape	Y_{1n} ($x10^{10}$)	$<T_i>_{Y1n}$ (keV)	Bang Time (ps)	Burn Width (ps)
27445	D2(15) CH[19.2] 939.4 µm	22.2	SSD: SG1018	7.7 +/- 0.8	3.6 +/- 0.5	1860 +/- 50	170 +/- 25

$<Y_{2p}>$ ($x10^7$)	Y_{2n} ($x10^7$)	$\rho R_{hot, 2p,}$ hot-spot (mg/cm²)	$\rho R_{hot, 2n,}$ hot-spot (mg/cm²)	$\rho R_{hot, 2p,}$ uniform (mg/cm²)	$\rho R_{hot, 2n,}$ uniform (mg/cm²)	$<E_{2p}>$ (MeV)	ρR_{total} (mg/cm²)
5.2 +/- 0.8	7.1 +/- 1.2	3.4 +0.6 -0.8	8.0 +1.4 -2.1	4.5 +0.9 -1.2	10.3 +1.8 -2.6	13.62 +/- 0.1	41.9 +/- 3.0

Secondary proton spectra from WRF

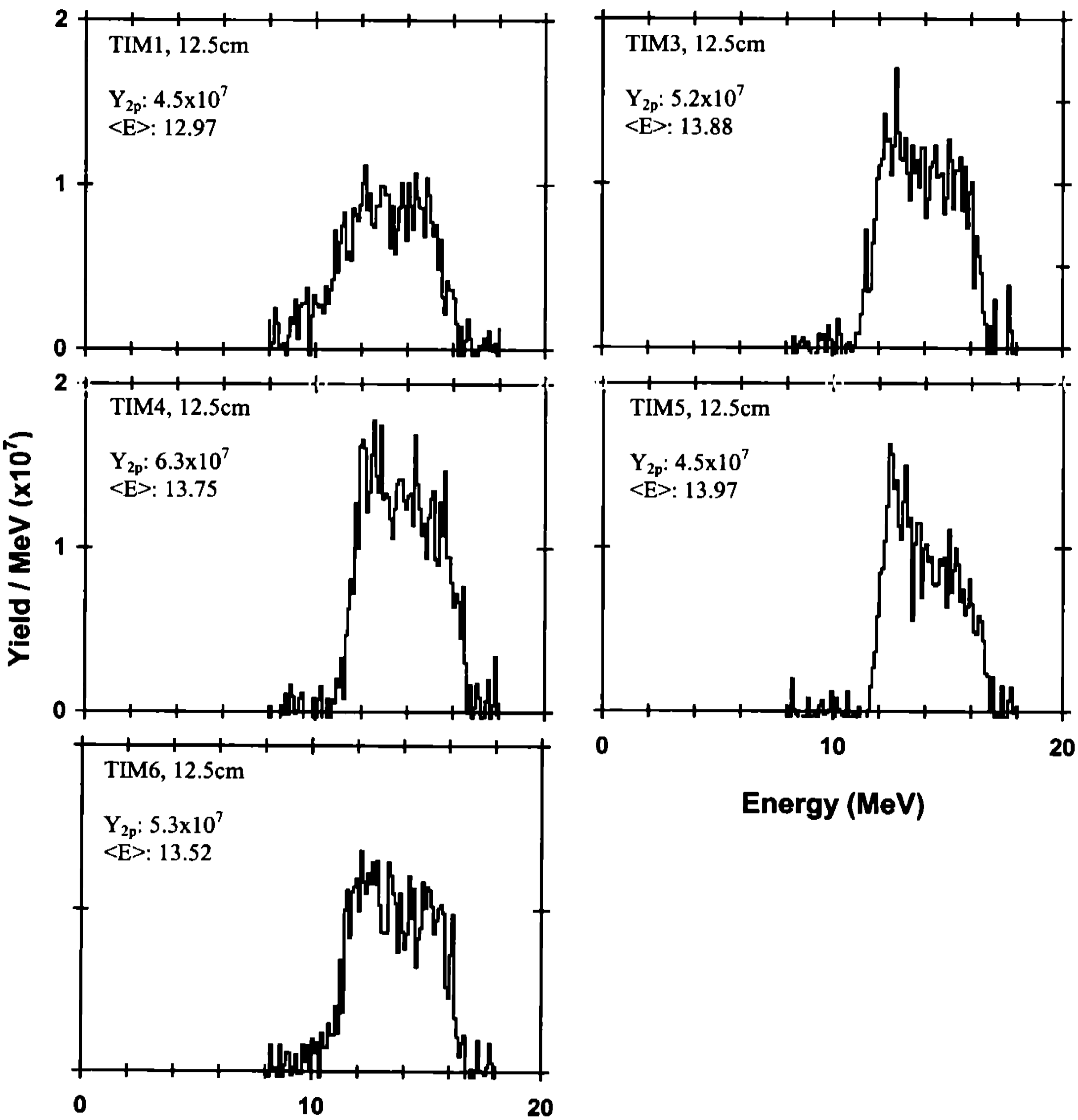

Shot #	Target	On-Target Energy (kJ)	Pulse Shape	Y_{1n} ($x10^{10}$)	$\langle T_i \rangle_{Y1n}$ (keV)	Bang Time (ps)	Burn Width (ps)
27446	D2(15) CH[19.3] 939.6 μm	21.6	SSD: SG1018	5.1 +/- 0.5	4.0 +/- 0.5	1850 +/- 50	170 +/- 25

$\langle Y_{2p} \rangle$ ($x10^7$)	Y_{2n} ($x10^7$)	$\rho R_{hot,\,2p,\,hot\text{-}spot}$ (mg/cm^2)	$\rho R_{hot,\,2n,\,hot\text{-}spot}$ (mg/cm^2)	$\rho R_{hot,\,2p,\,uniform}$ (mg/cm^2)	$\rho R_{hot,\,2n,\,uniform}$ (mg/cm^2)	$\langle E_{2p} \rangle$ (MeV)	ρR_{total} (mg/cm^2)
2.7 +/- 0.4	4.4 +/- 0.9	2.7 +0.5 -0.7	7.5 +1.6 -2.2	3.6 +0.6 -0.9	9.8 +2.0 -2.9	13.79 +/- 0.1	36.8 +/- 3.0

Secondary proton spectra from WRF

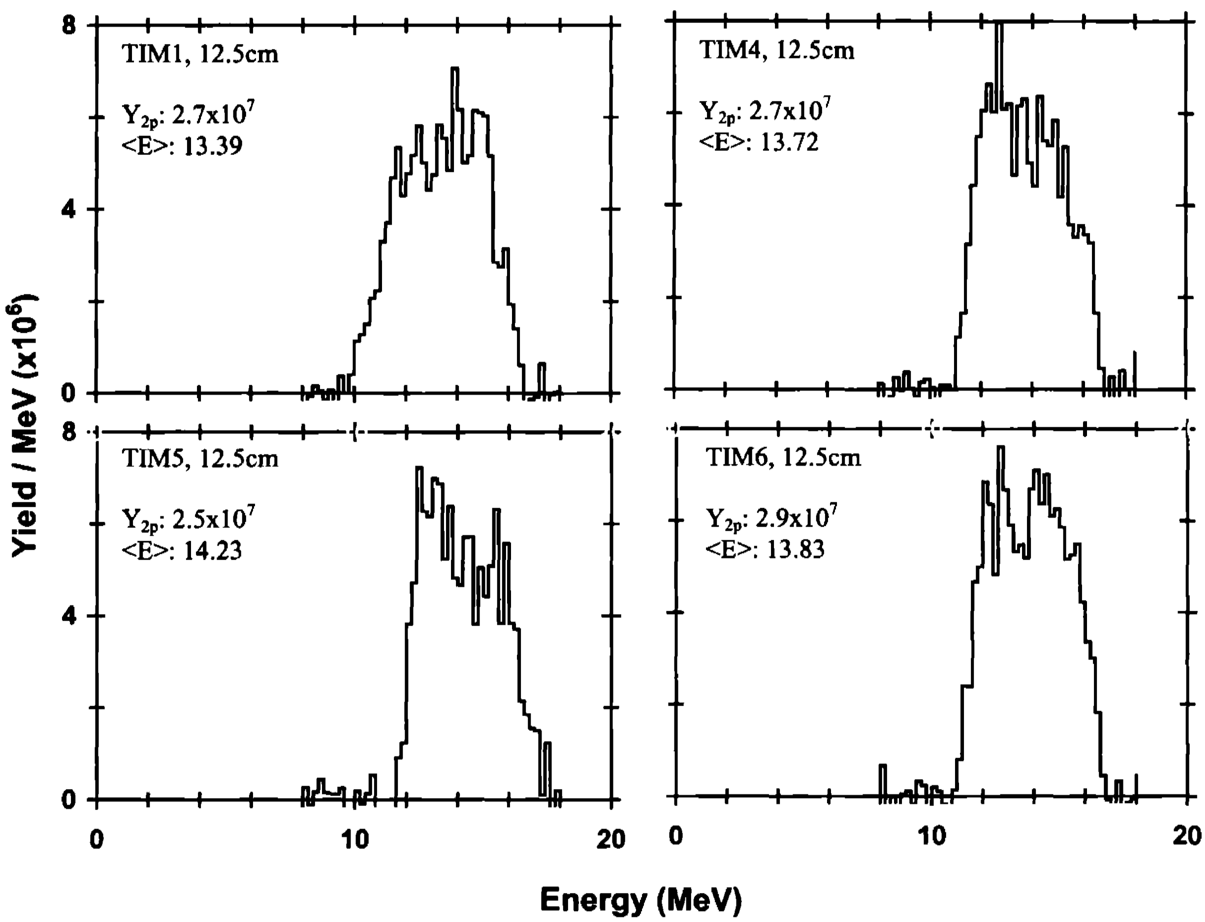

Shot #	Target	On-Target Energy (kJ)	Pulse Shape	Y_{1n} ($x10^{11}$)	$<T_i>_{Y1n}$ (keV)	Bang Time (ps)	Burn Width (ps)
27447	D2(15) CH[19.3] 930.6 μm	21.6	SSD: SG1018	1.4 +/- 0.1	3.6 +/- 0.5	1840 +/- 50	160 +/- 25

$<Y_{2p}>$ ($x10^8$)	Y_{2n} ($x10^8$)	$\rho R_{hot, 2p,}$ hot-spot (mg/cm^2)	$\rho R_{hot, 2n,}$ hot-spot (mg/cm^2)	$\rho R_{hot, 2p,}$ uniform (mg/cm^2)	$\rho R_{hot, 2n,}$ uniform (mg/cm^2)	$<E_{2p}>$ (MeV)	ρR_{total} (mg/cm^2)
1.7 +/- 0.2	2.9 +/- 0.4	5.9 +0.8 -1.2	16.2 +2.2 -3.1	8.7 +2.0 -1.5	20.6 +2.7 -4.0	12.83 +/- 0.1	64.9 +/- 2.8

Secondary proton spectra from WRF

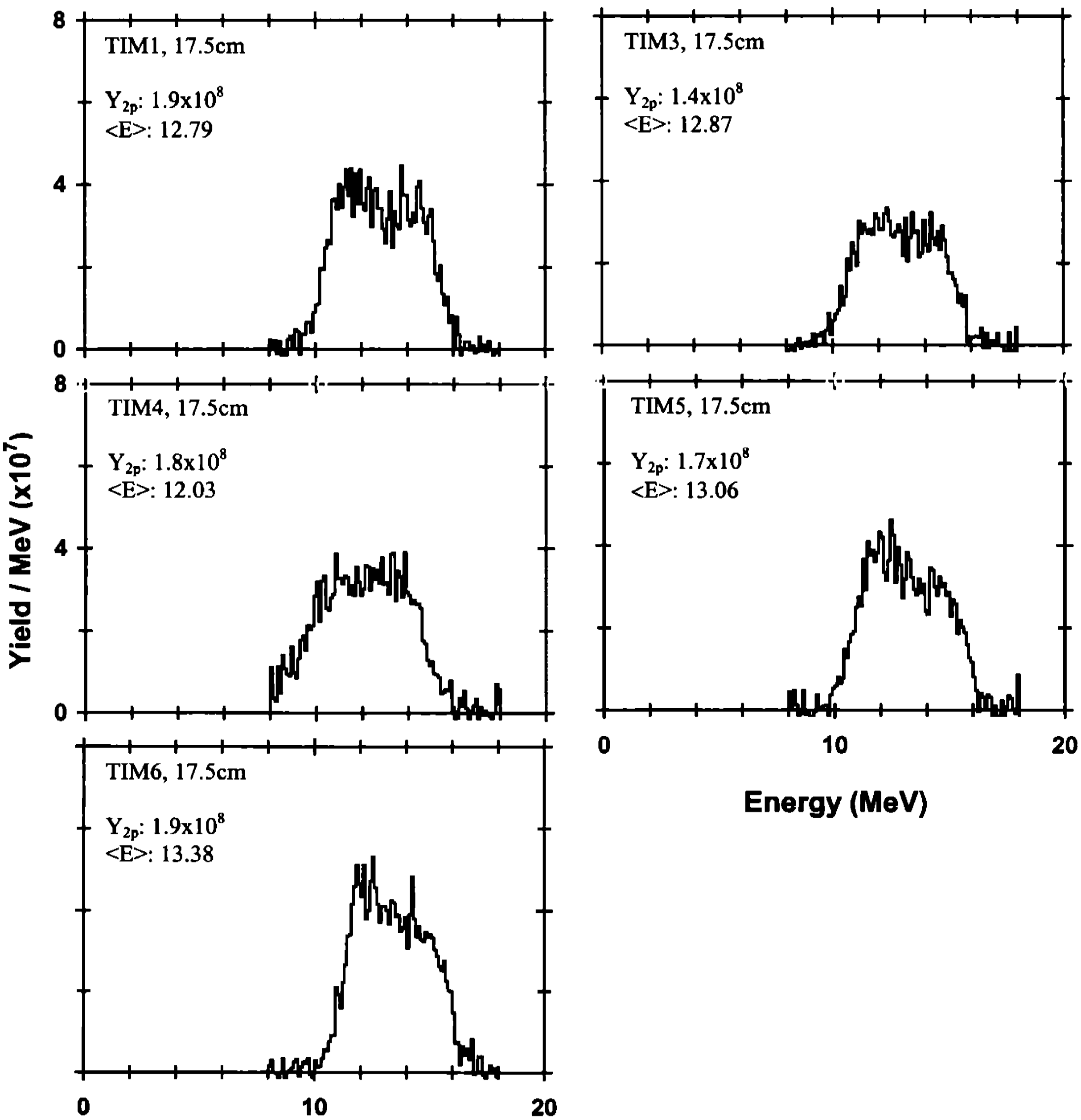

Shot #	Target	On-Target Energy (kJ)	Pulse Shape	Y_{1n} ($x10^{11}$)	$<T_i>_{Y1n}$ (keV)	Bang Time (ps)	Burn Width (ps)
27448	D2(15) CH[19.2] 930.4 μm	21.6	SSD: SG1018	1.4 +/- 0.1	3.8 +/- 0.5	1790 +/- 50	160 +/- 25

$<Y_{2p}>$ ($x10^8$)	Y_{2n} ($x10^8$)	$\rho R_{hot, 2p,}$ hot-spot (mg/cm^2)	$\rho R_{hot, 2n,}$ hot-spot (mg/cm^2)	$\rho R_{hot, 2p,}$ uniform (mg/cm^2)	$\rho R_{hot, 2n,}$ uniform (mg/cm^2)	$<E_{2p}>$ (MeV)	ρR_{total} (mg/cm^2)
1.9 +/- 0.2	2.0 +/- 0.3	7.2 + -1.4	11.7 +1.7 -2.5	9.9 +2.5 -1.8	15.3 +2.3 -3.4	13.10 +/- 0.1	57.1 +/- 2.9

Secondary proton spectra from WRF

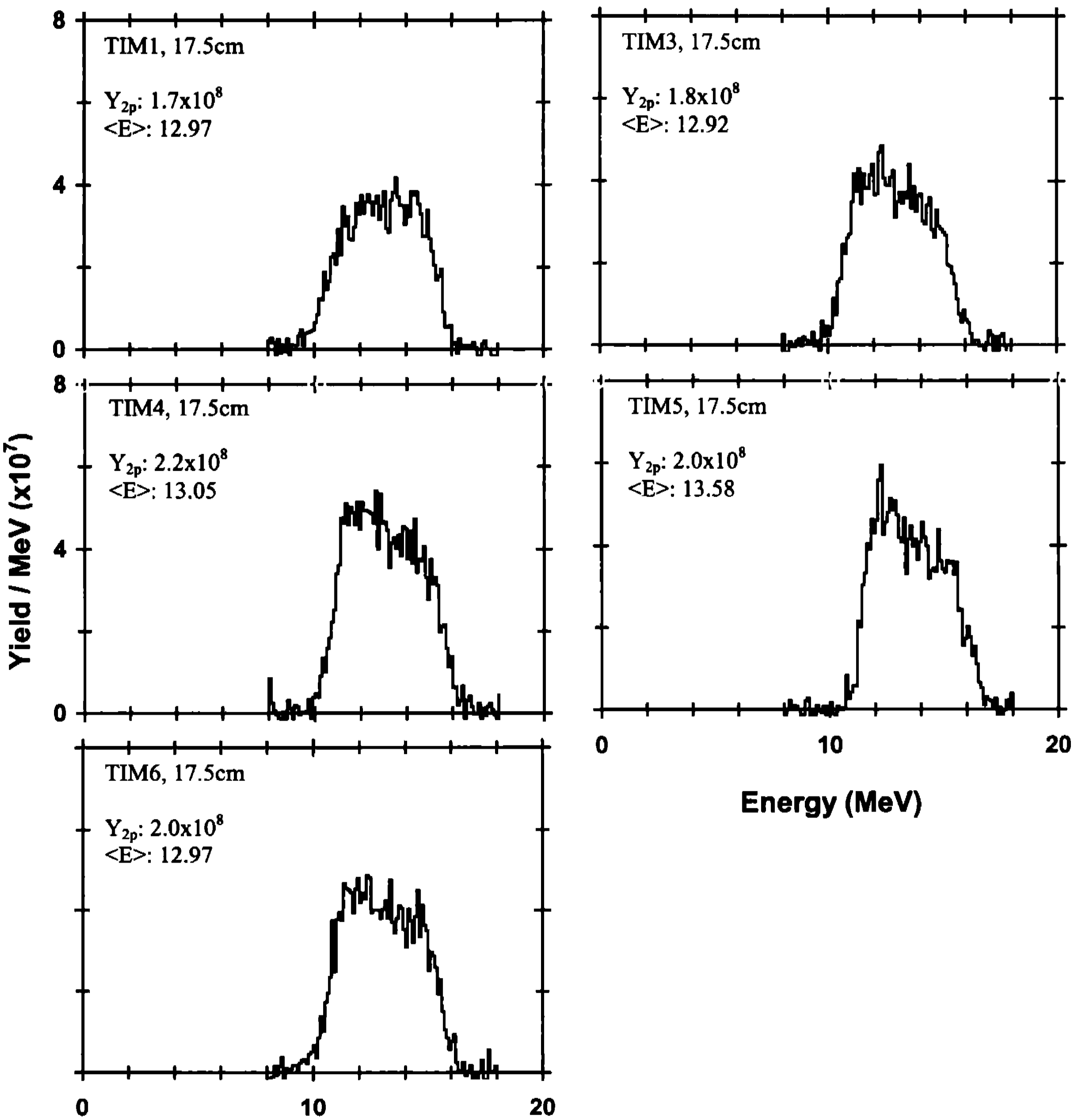

Shot #	Target	On-Target Energy (kJ)	Pulse Shape	Y_{1n} ($x10^{11}$)	$<T_i>_{Y1n}$ (keV)	Bang Time (ps)	Burn Width (ps)
27449	D2(15) CH[19.3] 939.6 μm	23.3	SSD: SG1018	1.6 +/- 0.2	4.2 +/- 0.5	1810 +/- 50	160 +/- 25

$<Y_{2p}>$ ($x10^8$)	Y_{2n} ($x10^8$)	$\rho R_{hot,\,2p,}$ hot-spot (mg/cm^2)	$\rho R_{hot,\,2n,}$ hot-spot (mg/cm^2)	$\rho R_{hot,\,2p,}$ uniform (mg/cm^2)	$\rho R_{hot,\,2n,}$ uniform (mg/cm^2)	$<E_{2p}>$ (MeV)	ρR_{total} (mg/cm^2)
1.6 +/- 0.2	2.3 +/- 0.3	4.9 +0.7 -0.9	11.8 +1.7 -2.5	6.8 +1.1 -1.0	15.6 +2.2 -3.2	13.21 +/- 0.1	54.0 +/- 2.9

Secondary proton spectra from WRF

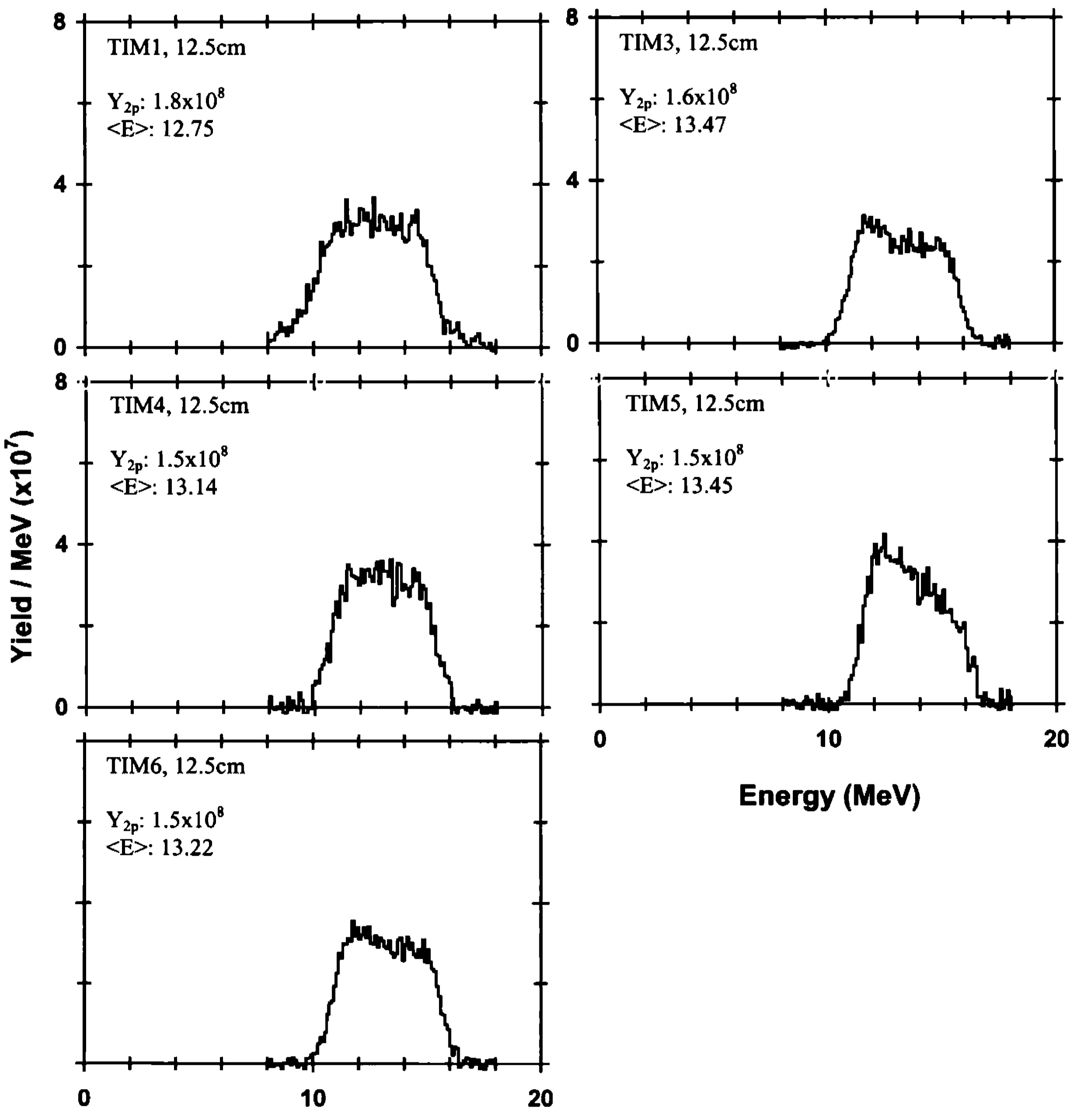

Shot #	Target	On-Target Energy (kJ)	Pulse Shape	Y_{1n} ($x10^{11}$)	$\langle T_i \rangle_{Y1n}$ (keV)	Bang Time (ps)	Burn Width (ps)
27450	D2(15) CH[19.3] 933.6 μm	22.1	SSD: SG1018	1.0 +/- 0.1	4.3 +/- 0.5	1810 +/- 50	160 +/- 25

$\langle Y_{2p} \rangle$ ($x10^7$)	Y_{2n} ($x10^8$)	$\rho R_{hot, 2p,}$ hot-spot (mg/cm^2)	$\rho R_{hot, 2n,}$ hot-spot (mg/cm^2)	$\rho R_{hot, 2p,}$ uniform (mg/cm^2)	$\rho R_{hot, 2n,}$ uniform (mg/cm^2)	$\langle E_{2p} \rangle$ (MeV)	ρR_{total} (mg/cm^2)
8.9 +/- 0.9	1.3 +/- 0.2	4.4 +0.6 -0.8	10.9 +1.7 -2.5	6.0 +/- 0.9	14.3 +2.3 -3.3	13.51 +/- 0.1	45.2 +/- 3.0

Secondary proton spectra from WRF

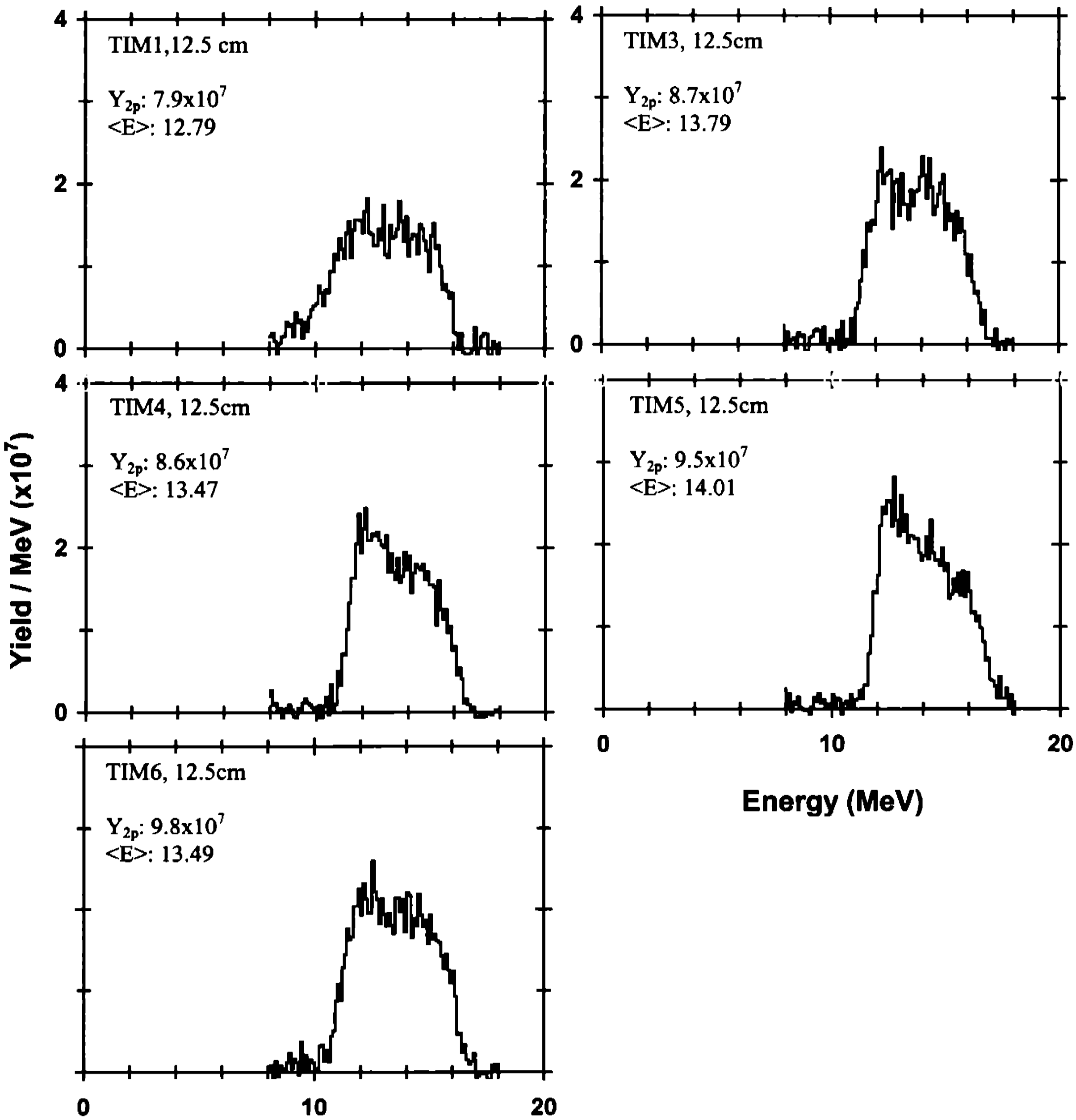

Shot #	Target	On-Target Energy (kJ)	Pulse Shape	Y_{1n} ($x10^{11}$)	$\langle T_i \rangle_{Y1n}$ (keV)	Bang Time (ps)	Burn Width (ps)
27454	D2(15) CH[19.4] 942.8 μm	22.2	SSD: SG1018	1.4 +/- 0.1	3.3 +/- 0.5	1870 +/- 50	160 +/- 25

$\langle Y_{2p} \rangle$ ($x10^8$)	Y_{2n} ($x10^8$)	$\rho R_{hot,\,2p,}$ hot-spot (mg/cm^2)	$\rho R_{hot,\,2n,}$ hot-spot (mg/cm^2)	$\rho R_{hot,\,2p,}$ uniform (mg/cm^2)	$\rho R_{hot,\,2n,}$ uniform (mg/cm^2)	$\langle E_{2p} \rangle$ (MeV)	ρR_{total} (mg/cm^2)
1.8 +/- 0.2	2.3 +/- 0.3	6.2 +1.0 -0.9	12.8 +1.8 -2.6	9.9 +3.7 -2.2	16.7 +2.2 -3.2	13.13 +/- 0.1	56.3 +/- 2.9

Secondary proton spectra from WRF

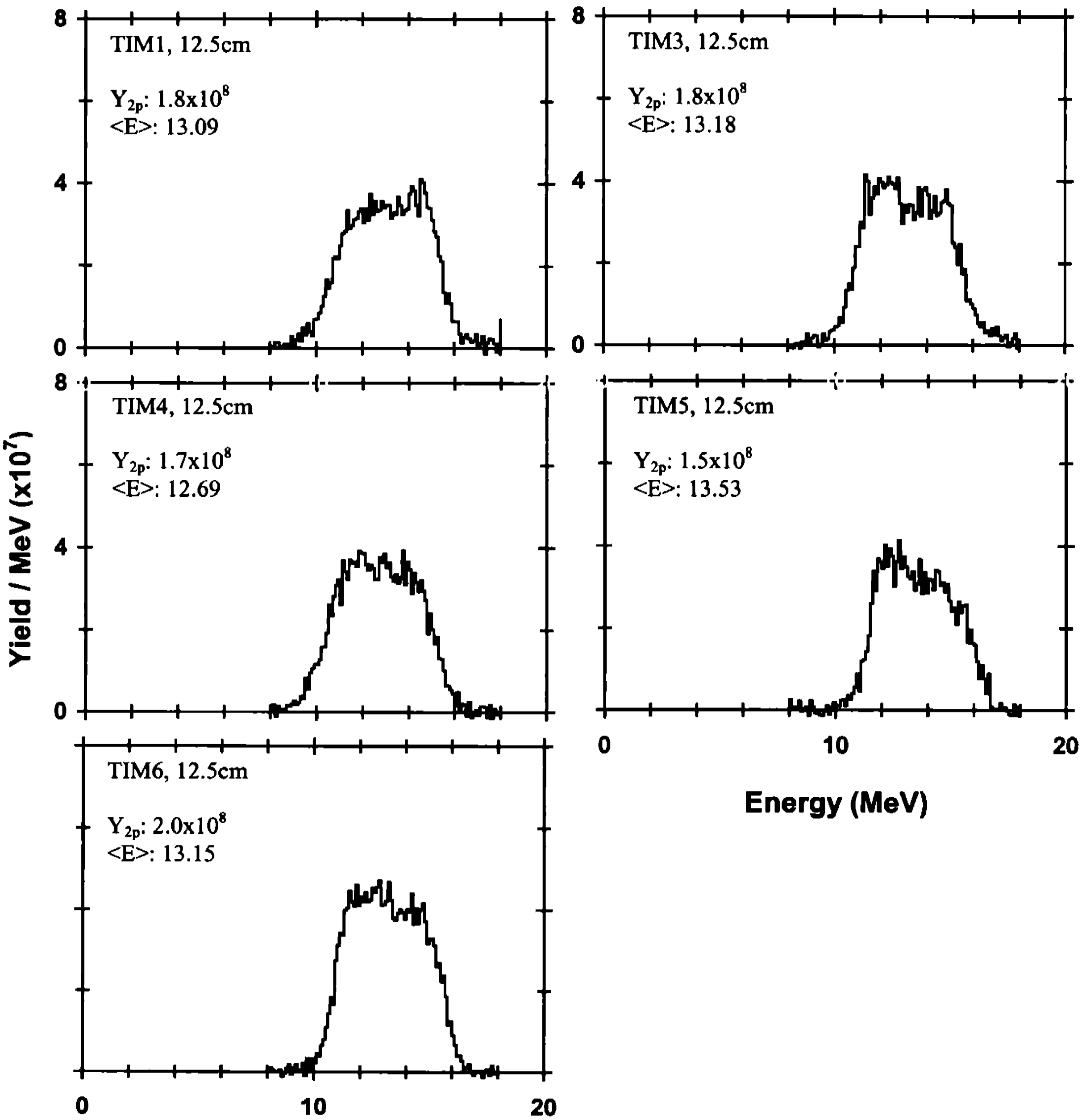

Shot #	Target	On-Target Energy (kJ)	Pulse Shape	Y_{1n} ($x10^{11}$)	$<T_i>_{Y1n}$ (keV)	Bang Time (ps)	Burn Width (ps)
27455	D2(15) CH[19.3] 940.6 μm	21.7	SSD: SG1018	1.1 +/- 0.1	5.1 +/- 0.5	1860 +/- 50	140 +/- 25

$<Y_{2p}>$ ($x10^8$)	Y_{2n} ($x10^8$)	$\rho R_{hot, 2p,}$ hot-spot (mg/cm^2)	$\rho R_{hot, 2n,}$ hot-spot (mg/cm^2)	$\rho R_{hot, 2p,}$ uniform (mg/cm^2)	$\rho R_{hot, 2n,}$ uniform (mg/cm^2)	$<E_{2p}>$ (MeV)	ρR_{total} (mg/cm^2)
1.0 +/- 0.1	1.4 +/- 0.2	4.5 + -3.3	10.9 +1.7 -2.5	6.2 +0.9 -1.2	14.3 +2.2 -3.2	13.19 +/- 0.1	54.5 +/- 2.9

Secondary proton spectra from WRF

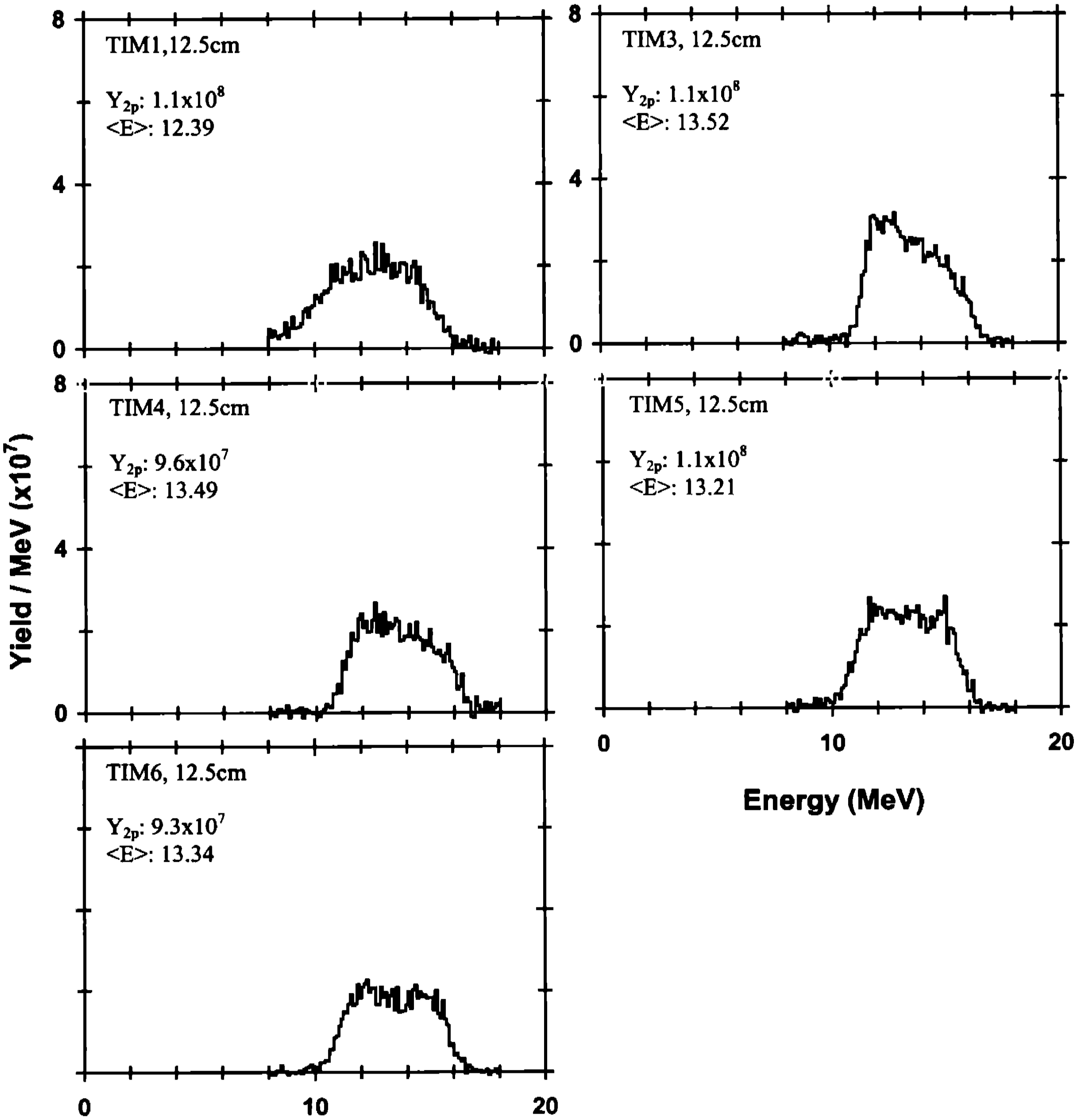

Shot #	Target	On-Target Energy (kJ)	Pulse Shape	Y_{1n} ($x10^{11}$)	$\langle T_i \rangle_{Y1n}$ (keV)	Bang Time (ps)	Burn Width (ps)
30621	D2(15.0) CH[19.4] 937.8 μm	N/A	SSD: SG1018	1.5 +/- 0.2	3.6 +/- 0.5	1890 +/- 50	170 +/- 25

$\langle Y_{2p} \rangle$ ($x10^8$)	Y_{2n} ($x10^8$)	$\rho R_{hot, 2p,}$ hot-spot (mg/cm^2)	$\rho R_{hot, 2n,}$ hot-spot (mg/cm^2)	$\rho R_{hot, 2p,}$ uniform (mg/cm^2)	$\rho R_{hot, 2n,}$ uniform (mg/cm^2)	$\langle E_{2p} \rangle$ (MeV)	ρR_{total} (mg/cm^2)
2.3 +/- 0.2	2.5 +/- 0.3	7.4 +1.2 -1.1	13.3 +1.8 -2.6	12.6 +5.6 -3.1	17.2 +2.2 -3.2	13.3 +/- 0.1	51.3 +/- 2.9

Secondary proton spectra from WRF

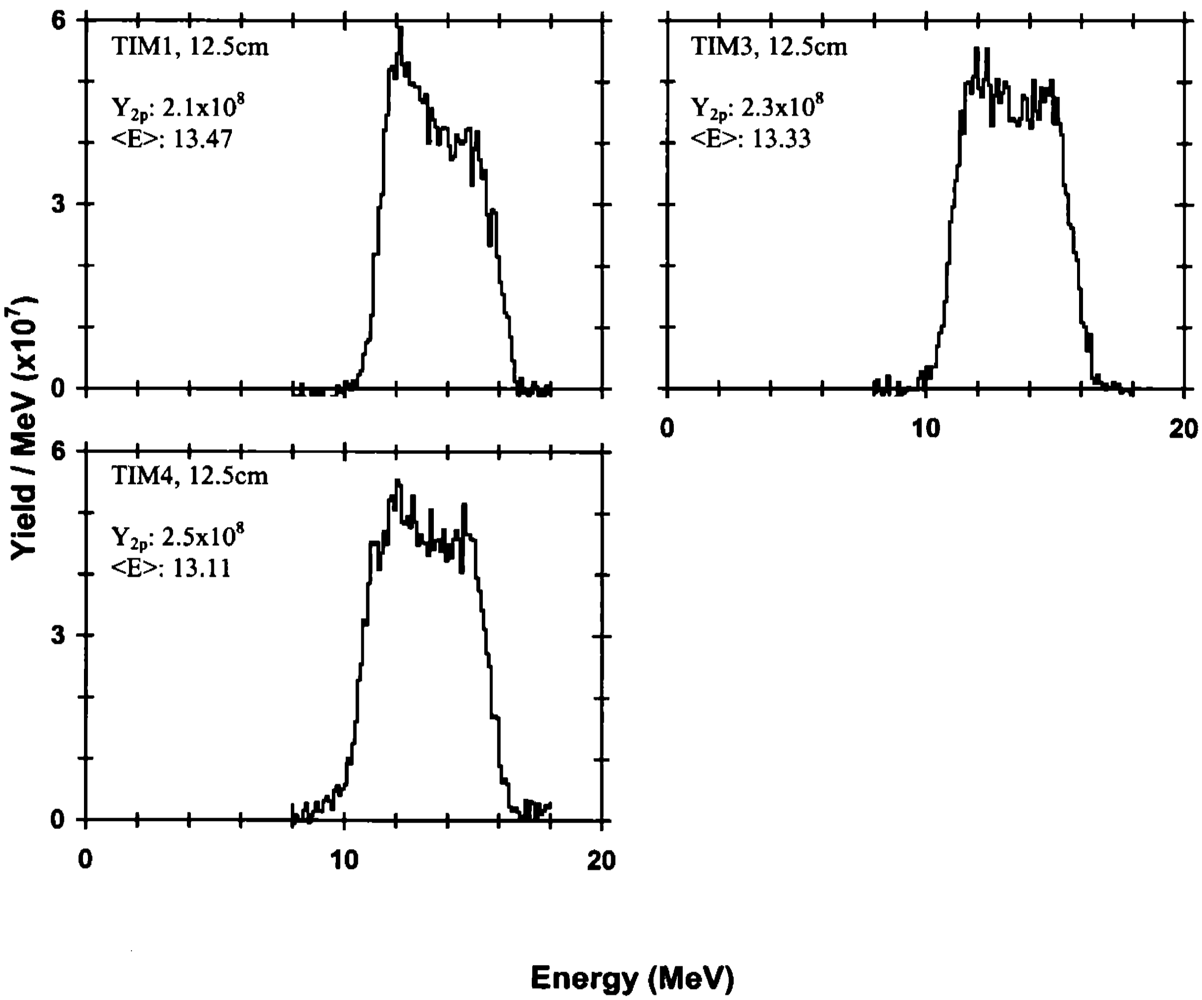

Shot #	Target	On-Target Energy (kJ)	Pulse Shape	Y_{1n} ($x10^{11}$)	$\langle T_i \rangle_{Y1n}$ (keV)	Bang Time (ps)	Burn Width (ps)
30626	D2(15.0) CH[19.1] 948.2 μm	22.5	SSD: SG1018	1.9 +/- 0.3	4.1 +/- 0.5	1900 +/- 50	140 +/- 25

$\langle Y_{2p} \rangle$ ($x10^8$)	Y_{2n} ($x10^8$)	$\rho R_{hot, 2p,}$ hot-spot (mg/cm^2)	$\rho R_{hot, 2n,}$ hot-spot (mg/cm^2)	$\rho R_{hot, 2p,}$ uniform (mg/cm^2)	$\rho R_{hot, 2n,}$ uniform (mg/cm^2)	$\langle E_{2p} \rangle$ (MeV)	ρR_{total} (mg/cm^2)
4.1 +/- 0.4	3.8 +/- 0.4	11.1 +3.4 -2.3	16.1 +2.7 -3.8	24.5 + -11.4	20.6 +3.2 -4.6	12.78 +/- 0.1	66.3 +/- 2.8

Secondary proton spectra from WRF

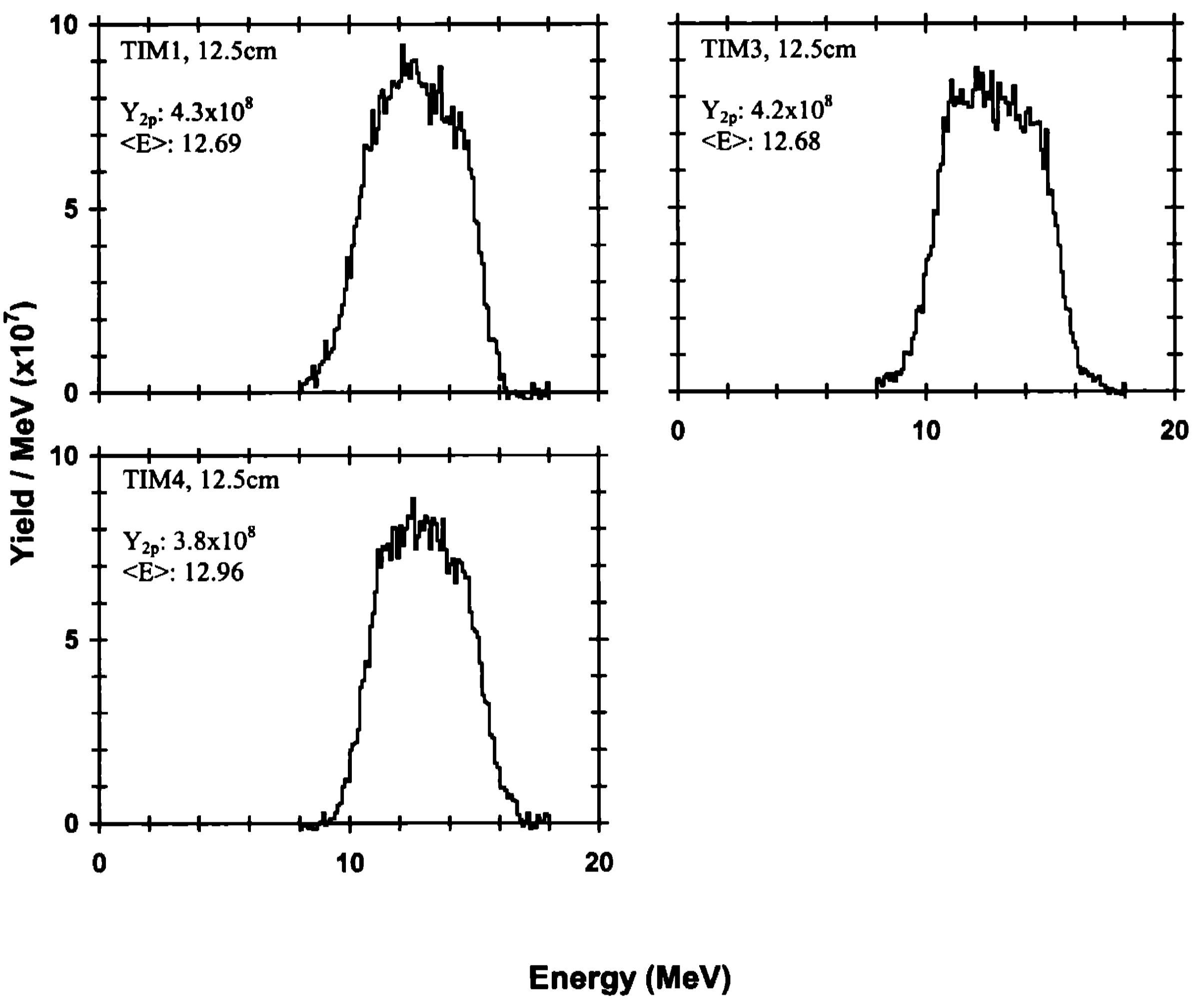

Shot #	Target	On-Target Energy (kJ)	Pulse Shape	Y_{1n} ($x10^{11}$)	$<T_i>_{Y1n}$ (keV)	Bang Time (ps)	Burn Width (ps)
30627	D2(15.0) CH[19.4] 941.8 μm	22.5	SSD: SG1018	1.8 +/- 0.3	3.7 +/- 0.5	1890 +/- 50	160 +/- 25

$<Y_{2p}>$ ($x10^8$)	Y_{2n} ($x10^8$)	$\rho R_{hot, 2p,}$ hot-spot (mg/cm²)	$\rho R_{hot, 2n,}$ hot-spot (mg/cm²)	$\rho R_{hot, 2p,}$ uniform (mg/cm²)	$\rho R_{hot, 2n,}$ uniform (mg/cm²)	$<E_{2p}>$ (MeV)	ρR_{total} (mg/cm²)
3.7 +/- 0.4	4.3 +/- 0.5	10.7 +4.3 -2.4	18.5 +2.9 -4.2	28.3 + -16.5	23.1 +3.5 -5.2	12.67 +/- 0.1	66.4 +/- 2.8

Secondary proton spectra from WRF

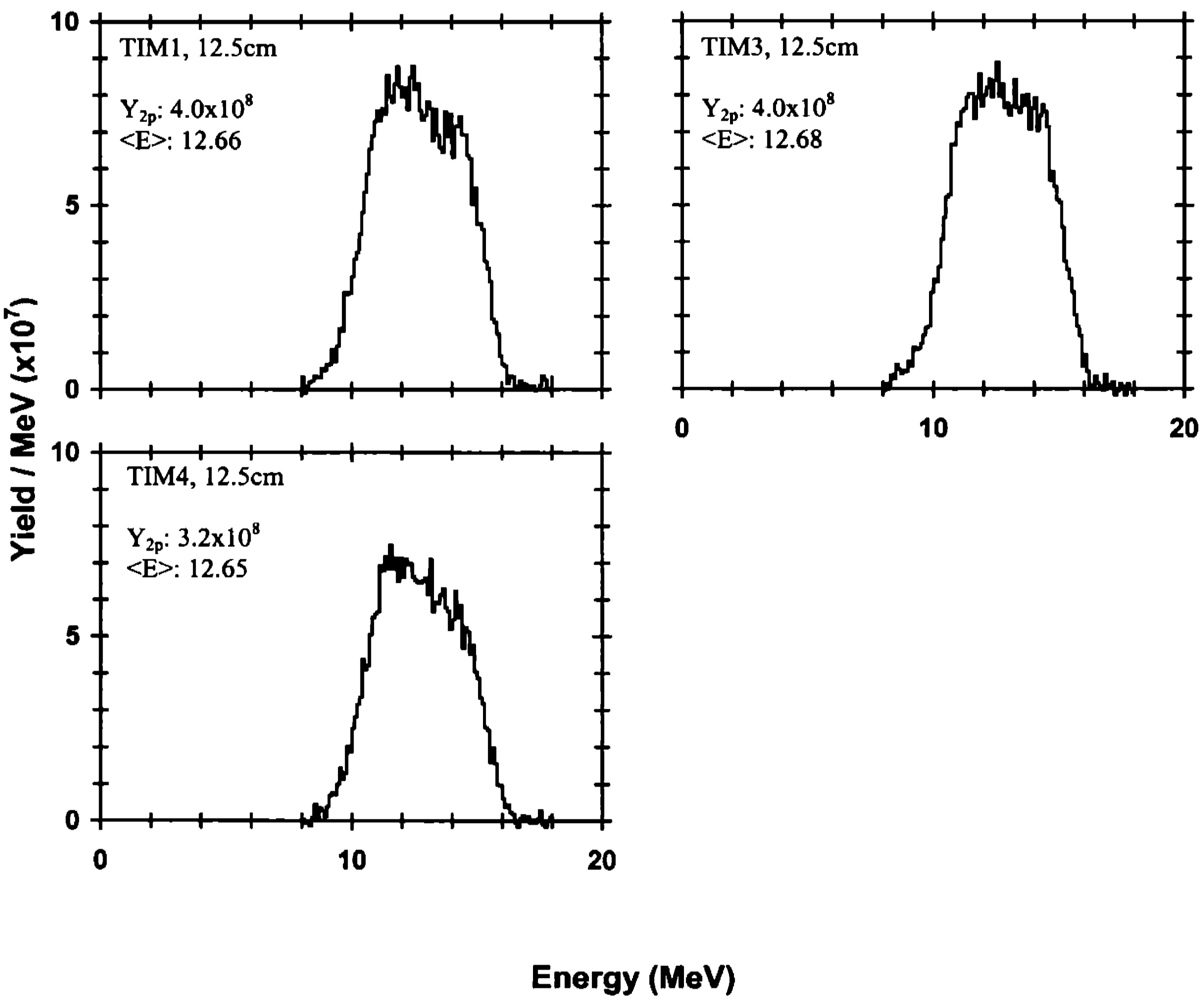

Shot #	Target	On-Target Energy (kJ)	Pulse Shape	Y_{1n} ($x10^{11}$)	$\langle T_i \rangle_{Y1n}$ (keV)	Bang Time (ps)	Burn Width (ps)
30628	D2(15.0) CH[19.3] 945.6 μm	22.5	SSD: SG1018	2.0 +/- 0.3	4.0 +/- 0.5	1880 +/- 50	160 +/- 25

$\langle Y_{2p} \rangle$ ($x10^8$)	Y_{2n} ($x10^8$)	$\rho R_{hot, 2p,}$ hot-spot (mg/cm^2)	$\rho R_{hot, 2n,}$ hot-spot (mg/cm^2)	$\rho R_{hot, 2p,}$ uniform (mg/cm^2)	$\rho R_{hot, 2n,}$ uniform (mg/cm^2)	$\langle E_{2p} \rangle$ (MeV)	ρR_{total} (mg/cm^2)
4.4 +/- 0.4	4.1 +/- 0.5	11.6 +4.5 -2.6	16.6 +2.7 -3.9	28.6 + -13.7	20.9 +2.6 -3.8	12.81 +/- 0.1	65.4 +/- 2.8

Secondary proton spectra from WRF

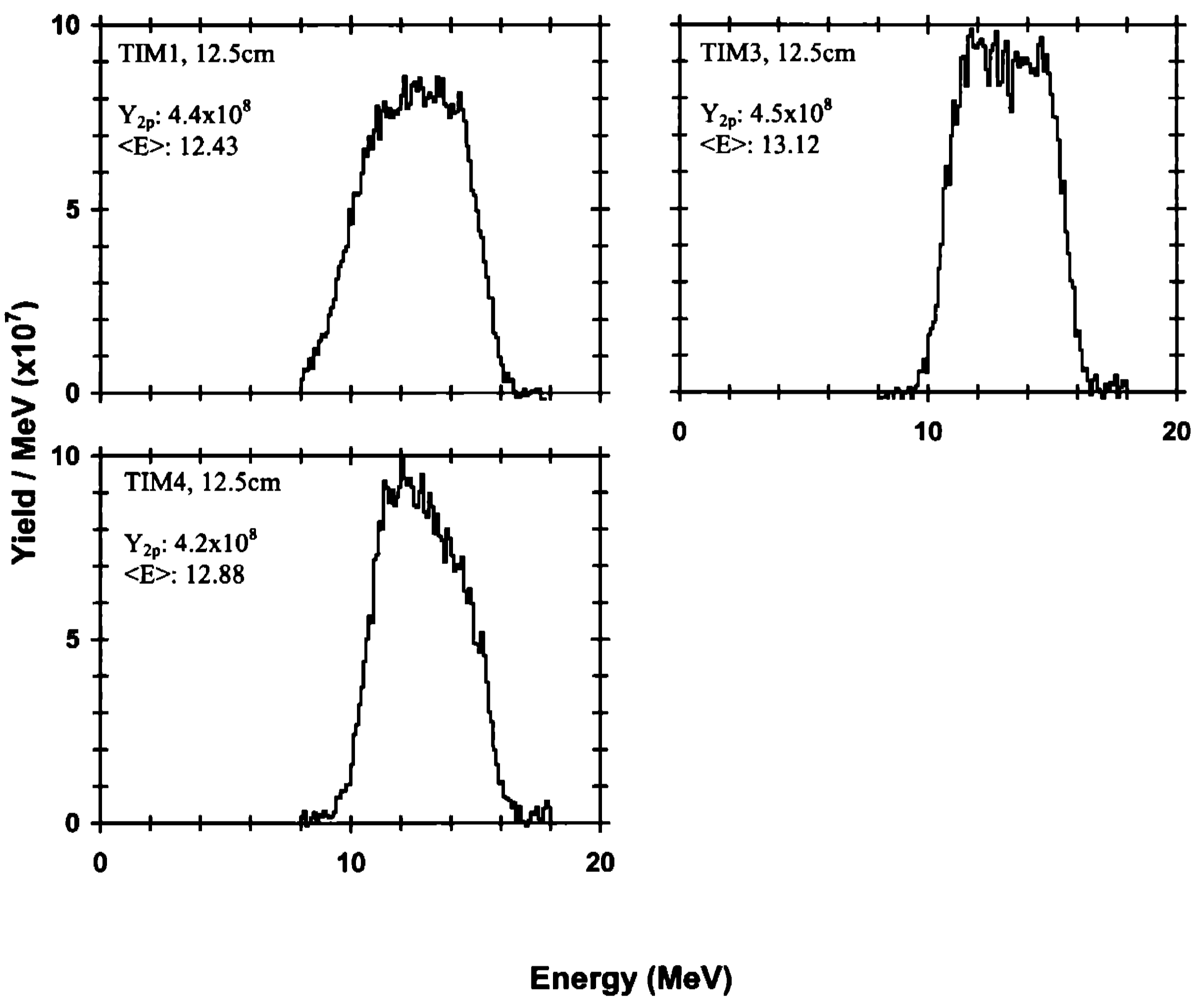

Shot #	Target	On-Target Energy (kJ)	Pulse Shape	Y_{1n} ($x10^{11}$)	$<T_i>_{Y1n}$ (keV)	Bang Time (ps)	Burn Width (ps)
30629	D2(15.0) CH[20.6] 945.2 μm	22.9	SSD: SG1018	1.5 +/- 0.2	3.5 +/- 0.5	1950 +/- 50	180 +/- 25

$<Y_{2p}>$ ($x10^8$)	Y_{2n} ($x10^8$)	$\rho R_{hot, 2p,}$ hot-spot (mg/cm^2)	$\rho R_{hot, 2n,}$ hot-spot (mg/cm^2)	$\rho R_{hot, 2p,}$ uniform (mg/cm^2)	$\rho R_{hot, 2n,}$ uniform (mg/cm^2)	$<E_{2p}>$ (MeV)	ρR_{total} (mg/cm^2)
3.7 +/- 0.4	3.1 +/- 0.4	13.9 + -3.3	16.4 +2.2 -3.1	N/A	20.4 +2.6 -3.8	12.51 +/- 0.1	73.8 +/- 2.8

Secondary proton spectra from WRF

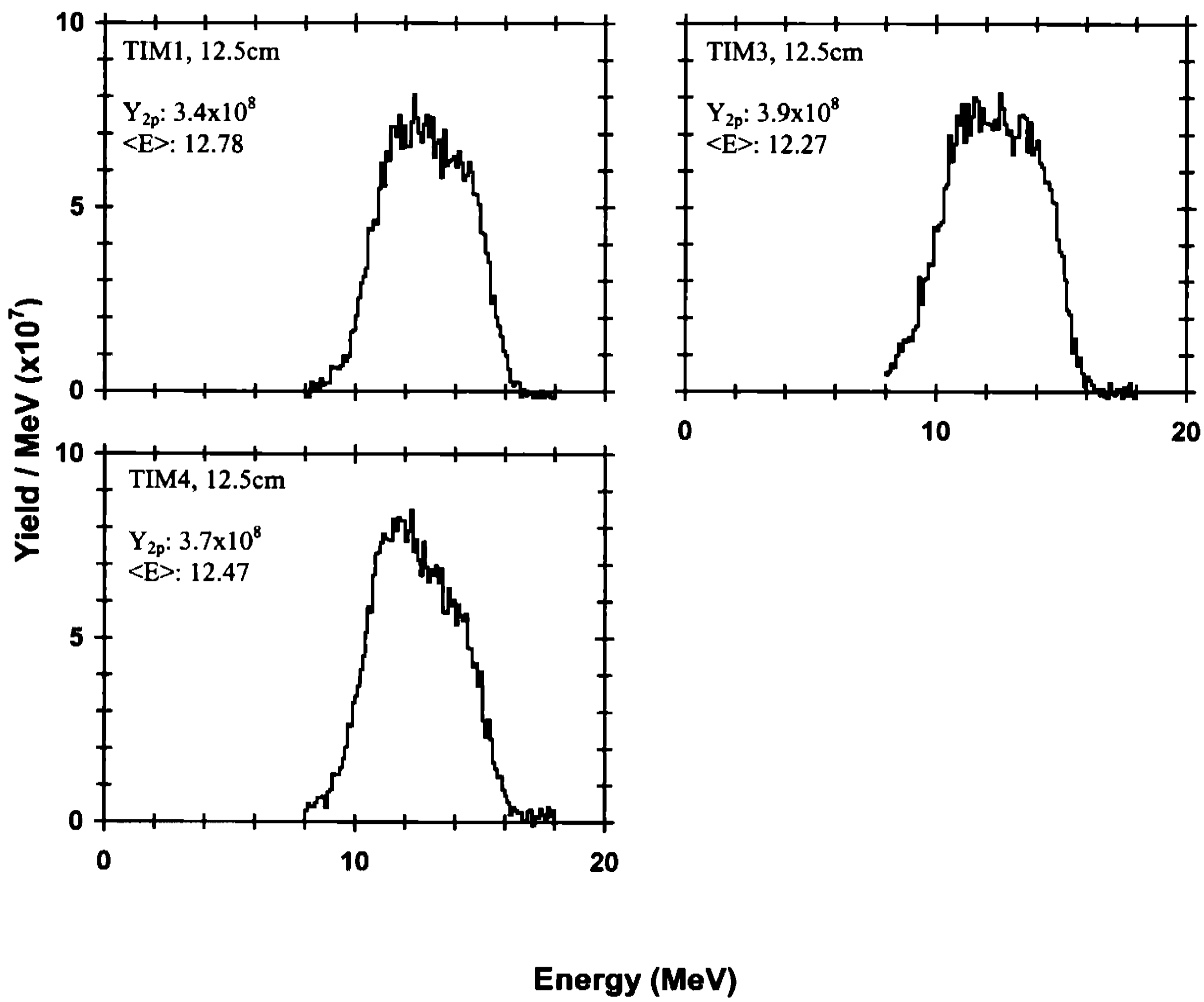

Shot #	Target	On-Target Energy (kJ)	Pulse Shape	Y_{1n} $(x10^{11})_n$	$<T_i>_{Y1n}$ (keV)	Bang Time (ps)	Burn Width (ps)
32130	D2(15.0) CH[19.1] 878.2	24.2	SSD: SG1018	2.4 +/- 0.4	4.1 +/- 0.5	1720 +/- 50	145 +/- 25

$<Y_{2p}>$ $(x10^8)$	Y_{2n} $(x10^8)$	$\rho R_{hot, 2p,}$ hot-spot (mg/cm^2)	$\rho R_{hot, 2n,}$ hot-spot (mg/cm^2)	$\rho R_{hot, 2p,}$ uniform (mg/cm^2)	$\rho R_{hot, 2n,}$ uniform (mg/cm^2)	$<E_{2p}>$ (MeV)	ρR_{total} (mg/cm^2)
5.7 +/- 0.6	4.1 +/- 0.5	13.4 + -3.3	14.2 +2.4 -3.4	N/A	18.0 +2.4 -3.4	12.74 +/- 0.1	67.4 +/- 2.8

Secondary proton spectra from WRF

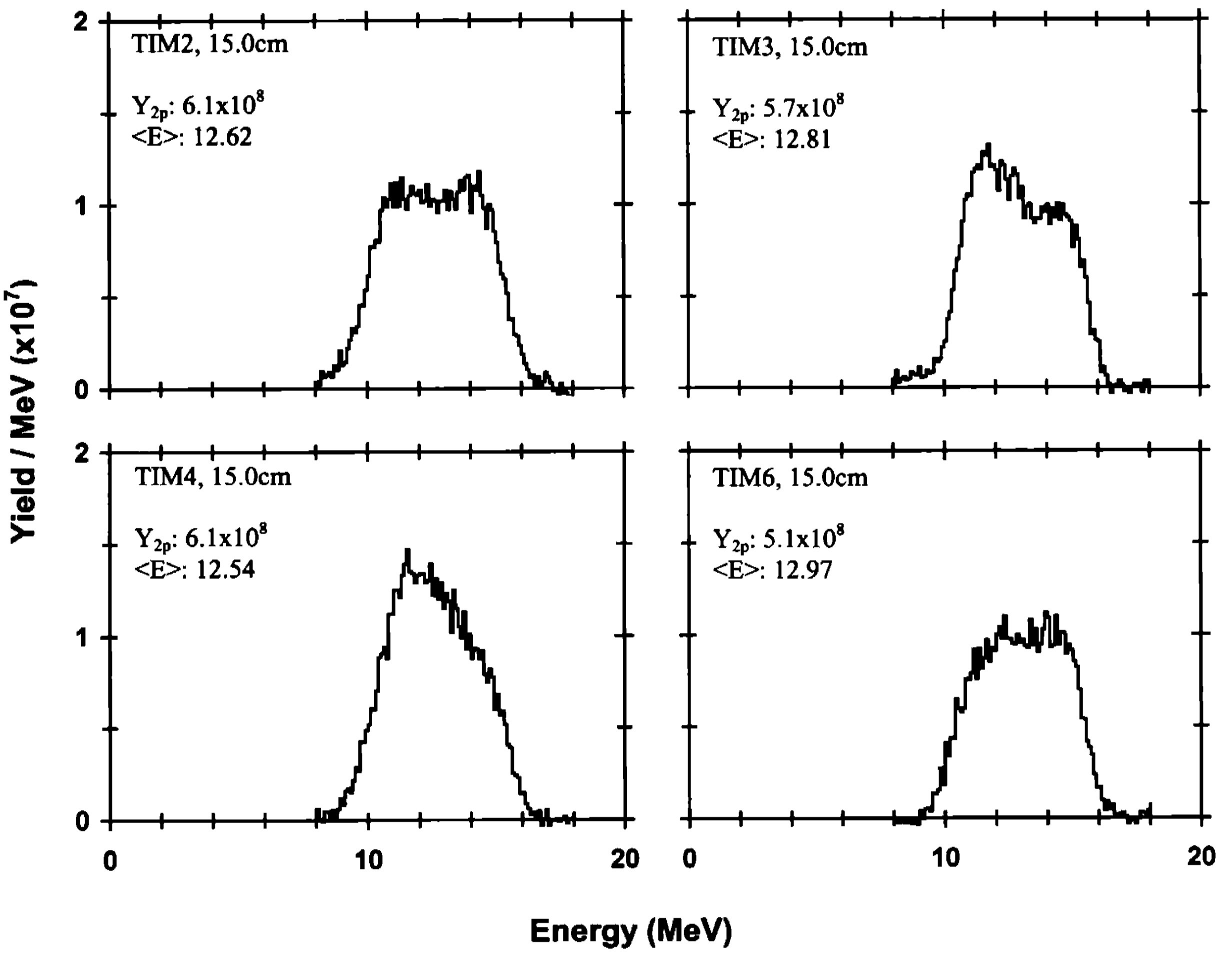

Shot #	Target	On-Target Energy (kJ)	Pulse Shape	Y_{1n} ($x10^{11}$)	$<T_i>_{Y1n}$ (keV)	Bang Time (ps)	Burn Width (ps)
32227	D2(15.0) CH[19.1] 880.2 μm	24.6	SSD: SG1018	2.1 +/- 0.3	4.1 +/- 0.5	1714 +/- 50	208 +/- 25

$<Y_{2p}>$ ($x10^8$)	Y_{2n} ($x10^8$)	$\rho R_{hot, 2p,}$ hot-spot (mg/cm^2)	$\rho R_{hot, 2n,}$ hot-spot (mg/cm^2)	$\rho R_{hot, 2p,}$ uniform (mg/cm^2)	$\rho R_{hot, 2n,}$ uniform (mg/cm^2)	$<E_{2p}>$ (MeV)	ρR_{total} (mg/cm^2)
4.3 +/- 0.4	4.0 +/- 0.5	10.3 +2.7 -2.1	15.5 +2.6 -3.7	20.7 + -7.2	19.8 +2.6 -3.8	12.78 +/- 0.1	66.3 +/- 2.8

Secondary proton spectra from WRF

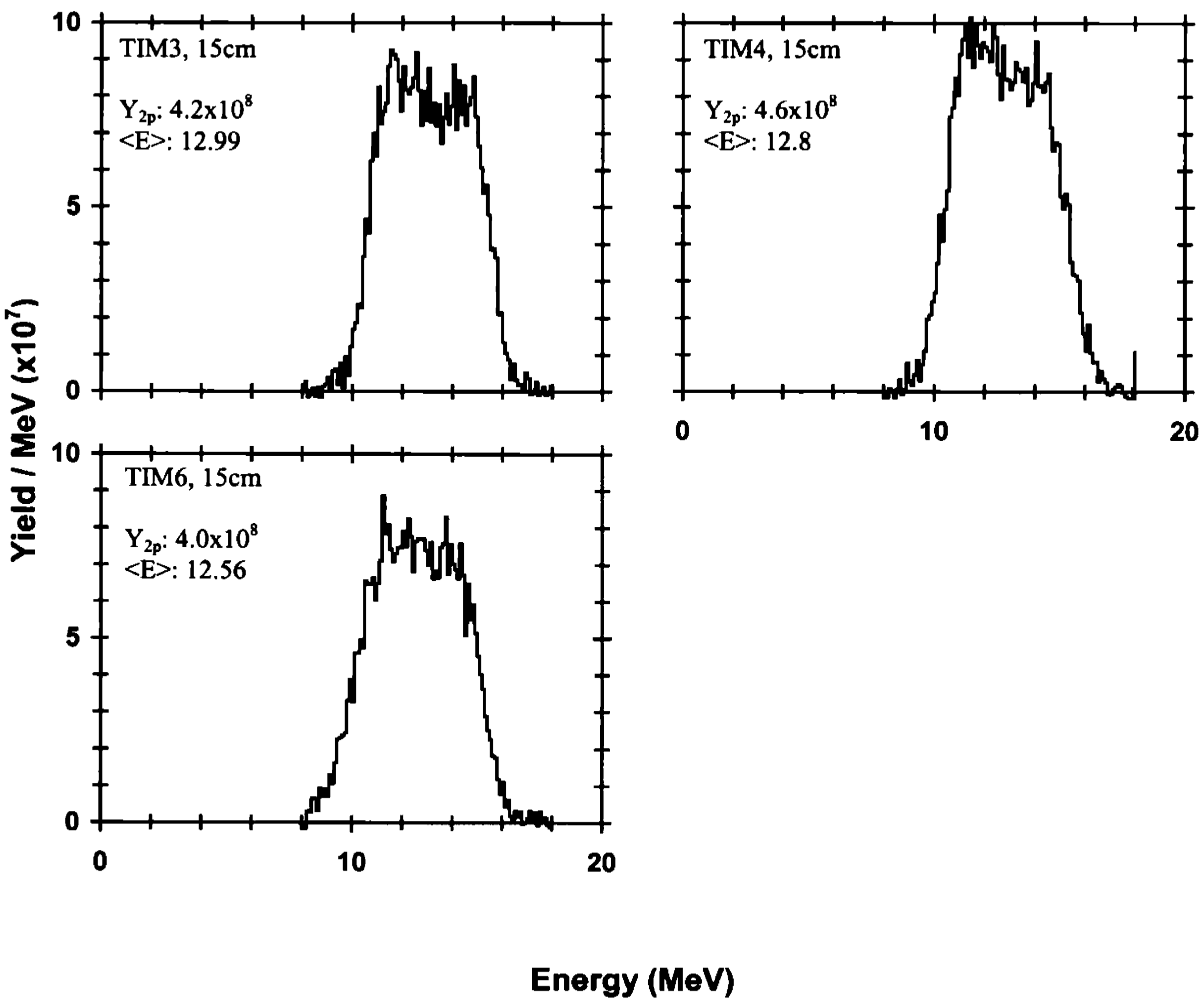

Shot #	Target	On-Target Energy (kJ)	Pulse Shape	Y_{1n} ($x10^{11}$)	$<T_i>_{Y1n}$ (keV)	Bang Time (ps)	Burn Width (ps)
32276	D2(15.0) CH[19.3] 876.6 μm	23.1	SSD: SG1018	1.6 +/- 0.2	4.4 +/- 0.5	1708 +/- 50	164 +/- 25

$<Y_{2p}>$ ($x10^8$)	Y_{2n} ($x10^8$)	$\rho R_{hot, 2p, hot-spot}$ (mg/cm^2)	$\rho R_{hot, 2n, hot-spot}$ (mg/cm^2)	$\rho R_{hot, 2p, uniform}$ (mg/cm^2)	$\rho R_{hot, 2n, uniform}$ (mg/cm^2)	$<E_{2p}>$ (MeV)	ρR_{total} (mg/cm^2)
2.5 +/- 0.3	3.0 +/- 0.4	7.8 +1.2 -1.1	15.5 +2.1 -3.1	11.4 +2.7 -2.1	19.7 +2.7 -4.0	12.57 +/- 0.1	72.2 +/- 2.8

Secondary proton spectra from WRF

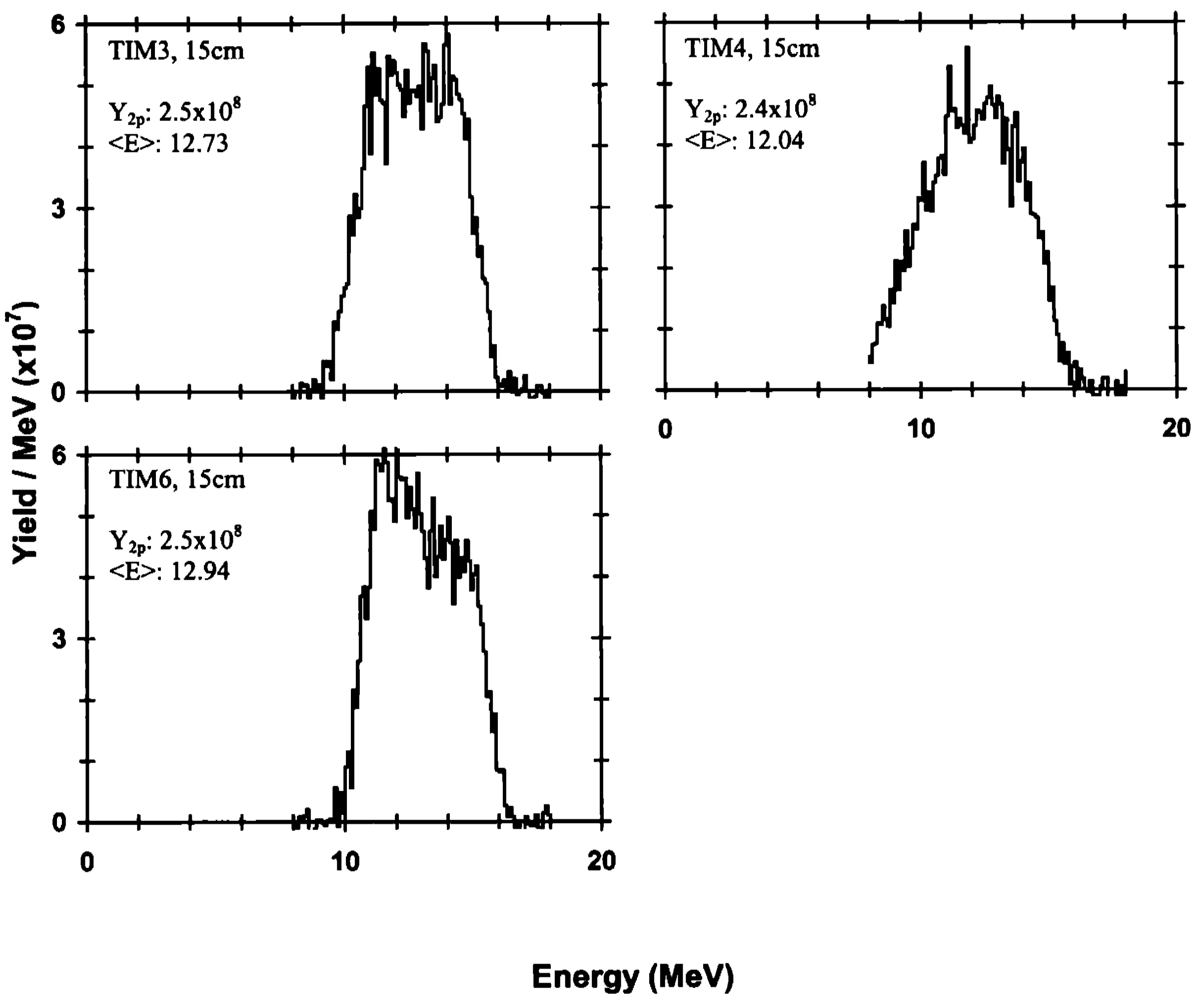

Shot #	Target	On-Target Energy (kJ)	Pulse Shape	Y_{1n} ($x10^{11}$)	$<T_i>_{Y1n}$ (keV)	Bang Time (ps)	Burn Width (ps)
32851	D2(15.0) CH[19.4] 877.8 μm	22.8	SSD: SG1018	1.7 +/- 0.2	4.3 +/- 0.5	1733 +/- 50	168 +/- 25

$<Y_{2p}>$ ($x10^8$)	Y_{2n} ($x10^8$)	$\rho R_{hot, 2p, hot-spot}$ (mg/cm^2)	$\rho R_{hot, 2n, hot-spot}$ (mg/cm^2)	$\rho R_{hot, 2p, uniform}$ (mg/cm^2)	$\rho R_{hot, 2n, uniform}$ (mg/cm^2)	$<E_{2p}>$ (MeV)	ρR_{total} (mg/cm^2)
3.2 +/- 0.3	2.6 +/- 0.3	9.5 +1.6 -1.4	13.1 +1.9 -2.7	15.8 +6.8 -3.9	16.5 +2.2 -3.1	12.89 +/- 0.1	63.2 +/- 2.8

Secondary proton spectra from WRF

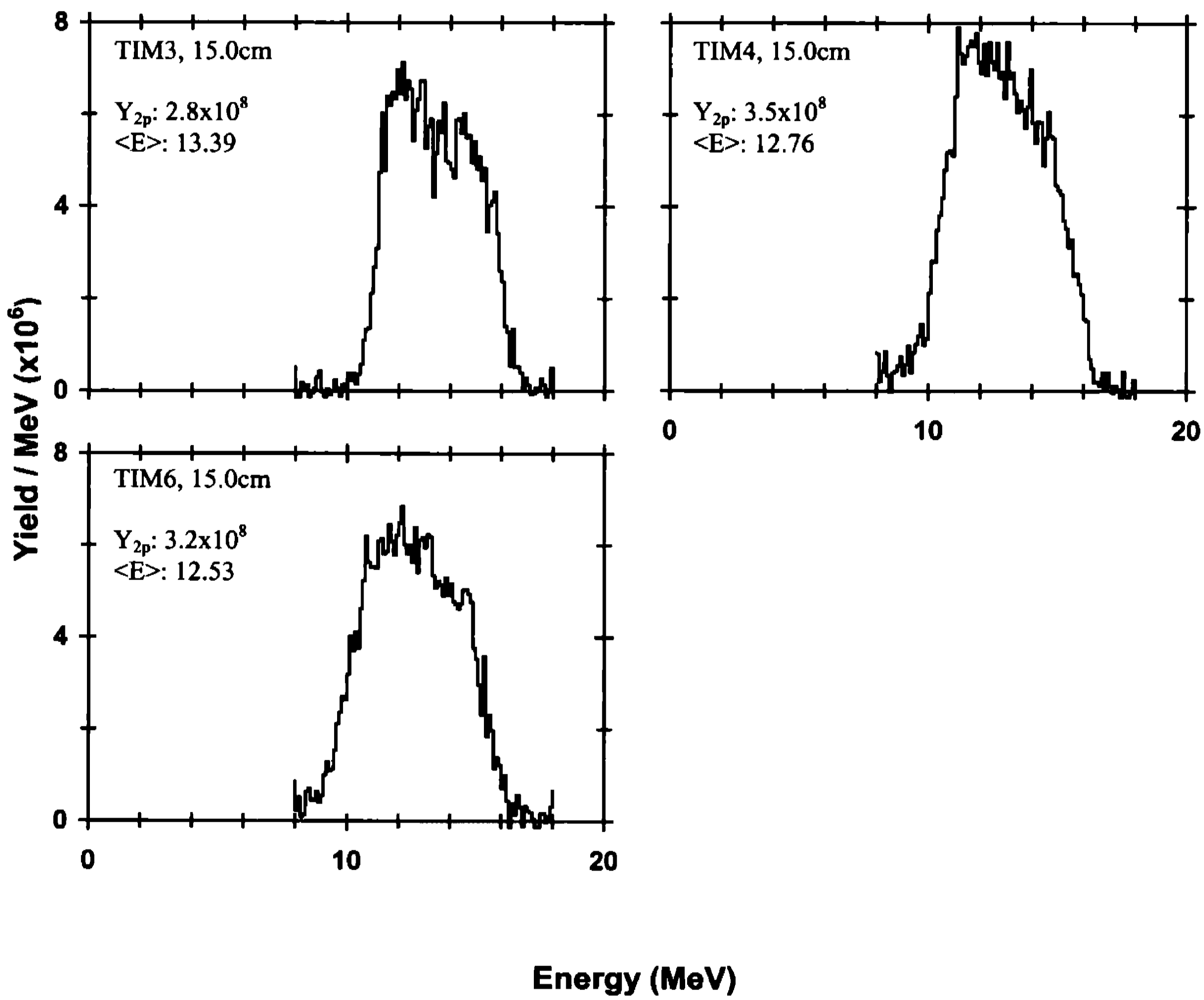

Summary of cryogenic implosions

Shot #	Target	On-Target Energy (kJ)	Pulse Shape	Y_{1n} ($x10^{10}$)	$<T_i>_{Y1n}$ (keV)	Bang Time (ps)	Burn Width (ps)
28199	CRYO	21.7	SSD: SG1018	1.1 +/- 0.1	3.1 +/- 0.5	1620 +/- 50	330 +/- 25

$<Y_{2p}>$ ($x10^7$)	Y_{2n} ($x10^7$)	$\rho R_{hot, 2p,}$ hot-spot (mg/cm^2)	$\rho R_{hot, 2n,}$ hot-spot (mg/cm^2)	$\rho R_{hot, 2p,}$ uniform (mg/cm^2)	$\rho R_{hot, 2n,}$ uniform (mg/cm^2)	$<E_{2p}>$ (MeV)	ρR_{total} (mg/cm^2)
1.6 +/- 0.2	9.5 +/- 1.5	7.5 +1.9 -1.5	44.4 +5.4 -7.5	13.1 +10.8 -4.2	45.5 +6.0 -7.3	13.89 +/- 0.1	35.1 +/- 3.1

Secondary proton spectra from WRF

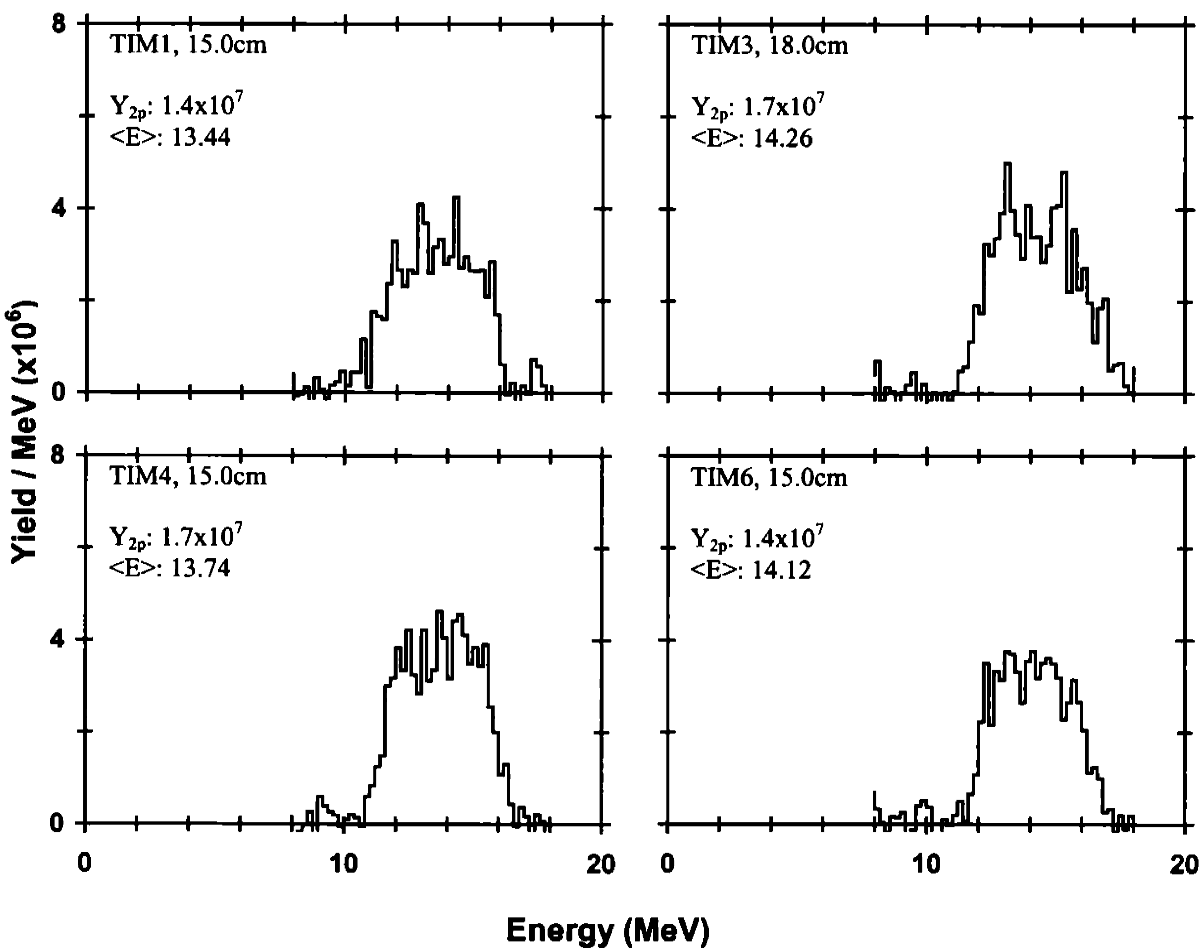

Shot #	Target	On-Target Energy (kJ)	Pulse Shape	Y_{1n} ($x10^{11}$)	$<T_i>_{Y1n}$ (keV)	Bang Time (ps)	Burn Width (ps)
28900	CRYO	23.3	SSD: SG1018	1.2 +/- 0.1	3.6 +/- 0.5	1620 +/- 50	170 +/- 25

$<Y_{2p}>$ ($x10^8$)	Y_{2n} ($x10^9$)	$\rho R_{hot, 2p,}$ hot-spot (mg/cm^2)	$\rho R_{hot, 2n,}$ hot-spot (mg/cm^2)	$\rho R_{hot, 2p,}$ uniform (mg/cm^2)	$\rho R_{hot, 2n,}$ uniform (mg/cm^2)	$<E_{2p}>$ (MeV)	ρR_{total} (mg/cm^2)
2.3 +/- 0.2	1.2 +/- 0.1	9.3 +1.9 -1.5	49.8 +5.0 -6.9	17.5 + 16.4 - 6.0	51.1 + 5.5 - 6.6	13.31 +/- 0.1	53.1 +/- 3.0

Secondary proton spectra from WRF

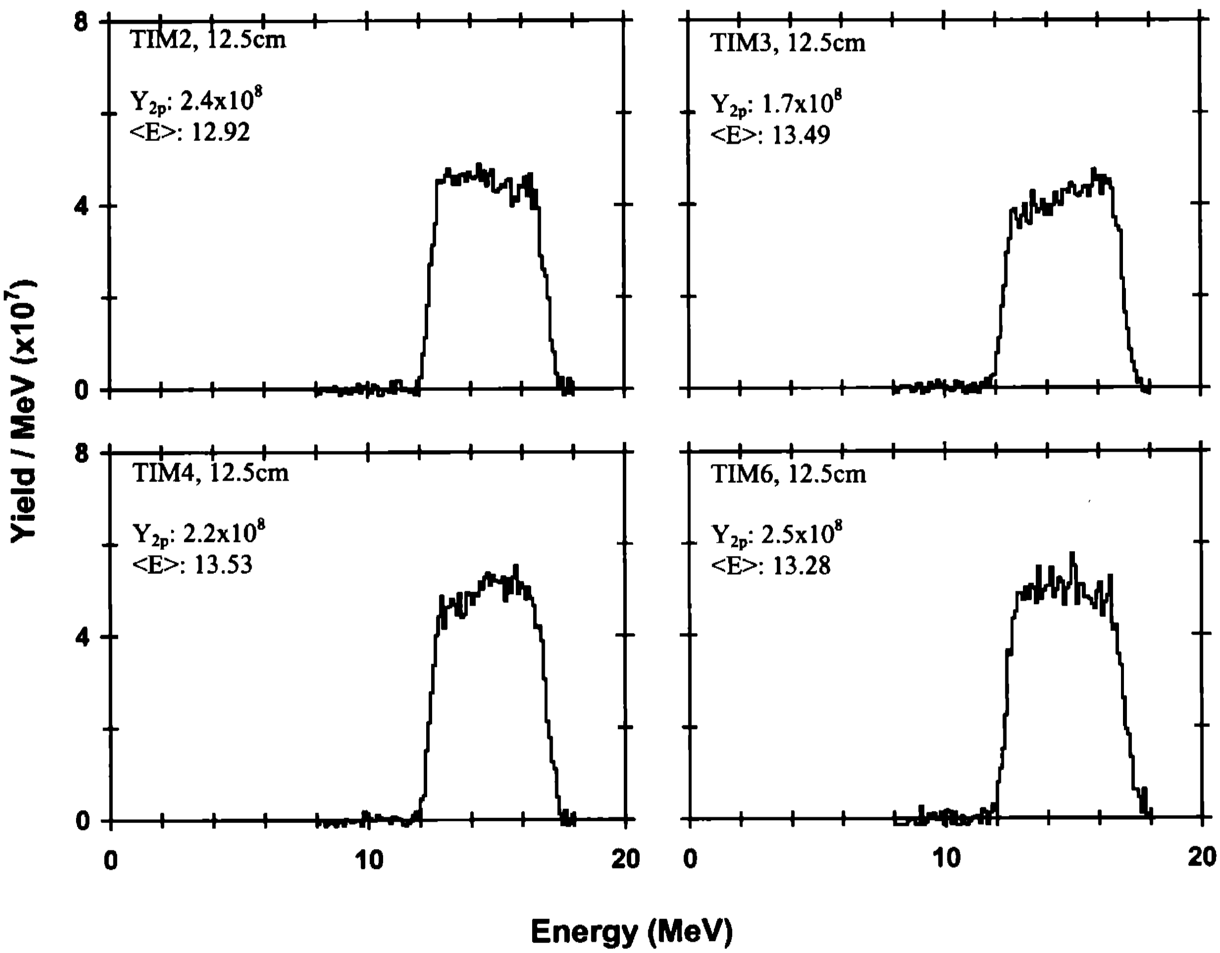

Shot #	Target	On-Target Energy (kJ)	Pulse Shape	Y_{1n} $(x10^{10})$	$<T_i>_{Y1n}$ (keV)	Bang Time (ps)	Burn Width (ps)
31279	CRYO	23.1	SSD: SG1018	1.1 +/- 0.1	3.8 +/- 0.5	1830 +/- 50	750 +/- 25

$<Y_{2p}>$ $(x10^7)$	Y_{2n} $(x10^7)$	$\rho R_{hot, 2p,}$ hot-spot (mg/cm^2)	$\rho R_{hot, 2n,}$ hot-spot (mg/cm^2)	$\rho R_{hot, 2p,}$ uniform (mg/cm^2)	$\rho R_{hot, 2n,}$ uniform (mg/cm^2)	$<E_{2p}>$ (MeV)	ρR_{total} (mg/cm^2)
1.2 +/- 0.2	6.5 +/- 1.1	5.6 +1.0 -1.4	39.0 +5.3 -7.8	7.5 +1.8 -1.5	42.9 +4.9 -7.1	13.95 +/- 0.1	33.2 +/- 3.1

Secondary proton spectra from WRF

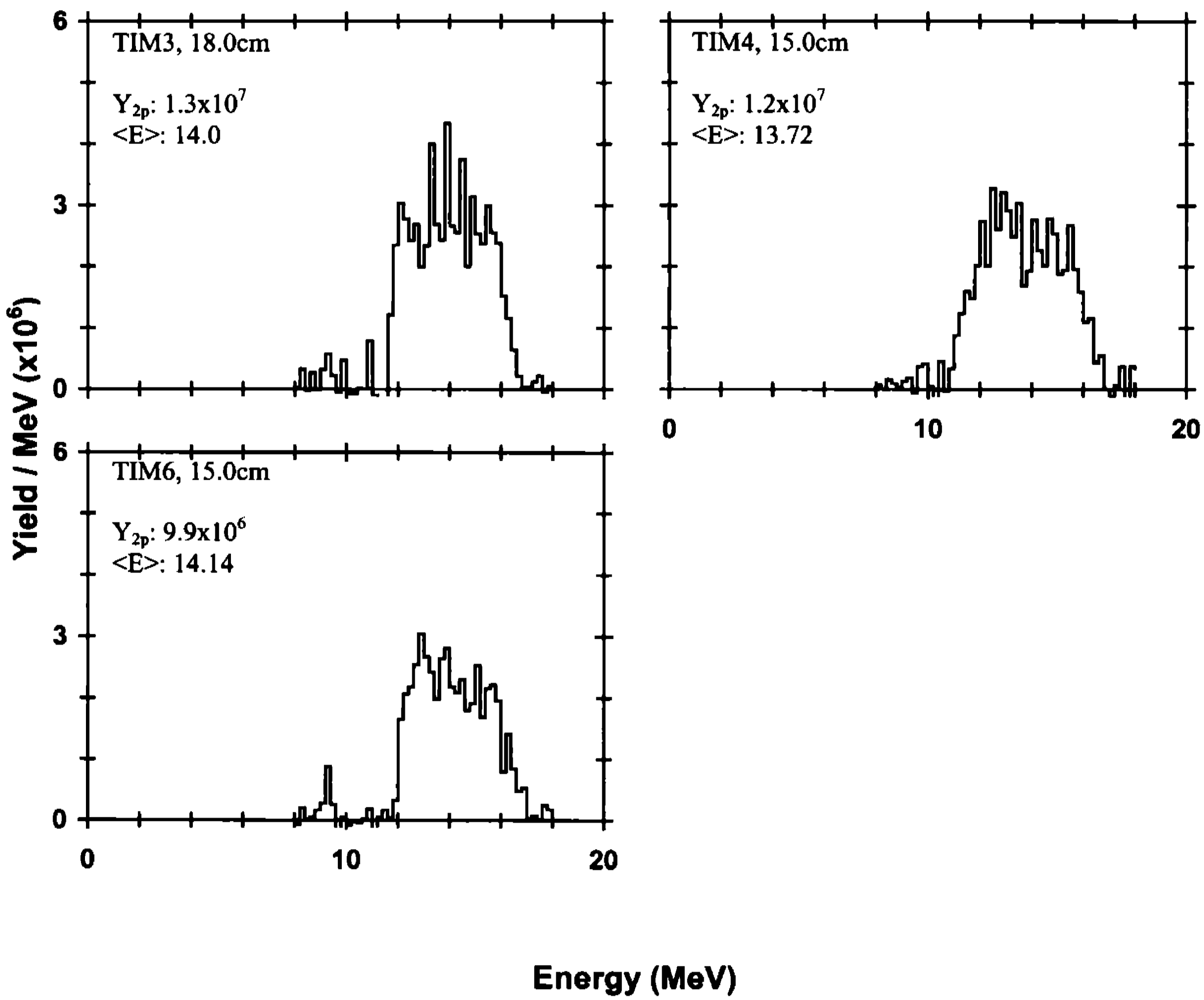

Shot #	Target	On-Target Energy (kJ)	Pulse Shape	Y_{1n} ($x10^{10}$)	$<T_i>_{Y1n}$ (keV)	Bang Time (ps)	Burn Width (ps)
31281	CRYO	23.0	SSD: SG1018	2.1 +/- 0.2	2.8 +/- 0.5	1780 +/- 50	290 +/- 25

$<Y_{2p}>$ ($x10^7$)	Y_{2n} ($x10^8$)	$\rho R_{hot, 2p, hot-spot}$ (mg/cm^2)	$\rho R_{hot, 2n, hot-spot}$ (mg/cm^2)	$\rho R_{hot, 2p, uniform}$ (mg/cm^2)	$\rho R_{hot, 2n, uniform}$ (mg/cm^2)	$<E_{2p}>$ (MeV)	ρR_{total} (mg/cm^2)
3.5 +/- 0.5	2.0 +/- 0.3	9.4 + -2.6	43.4 +5.4 -7.1	31.8 + -23.3	44.7 +6.4 -7.5	13.84 +/- 0.1	36.7 +/- 3.1

Secondary proton spectra from WRF

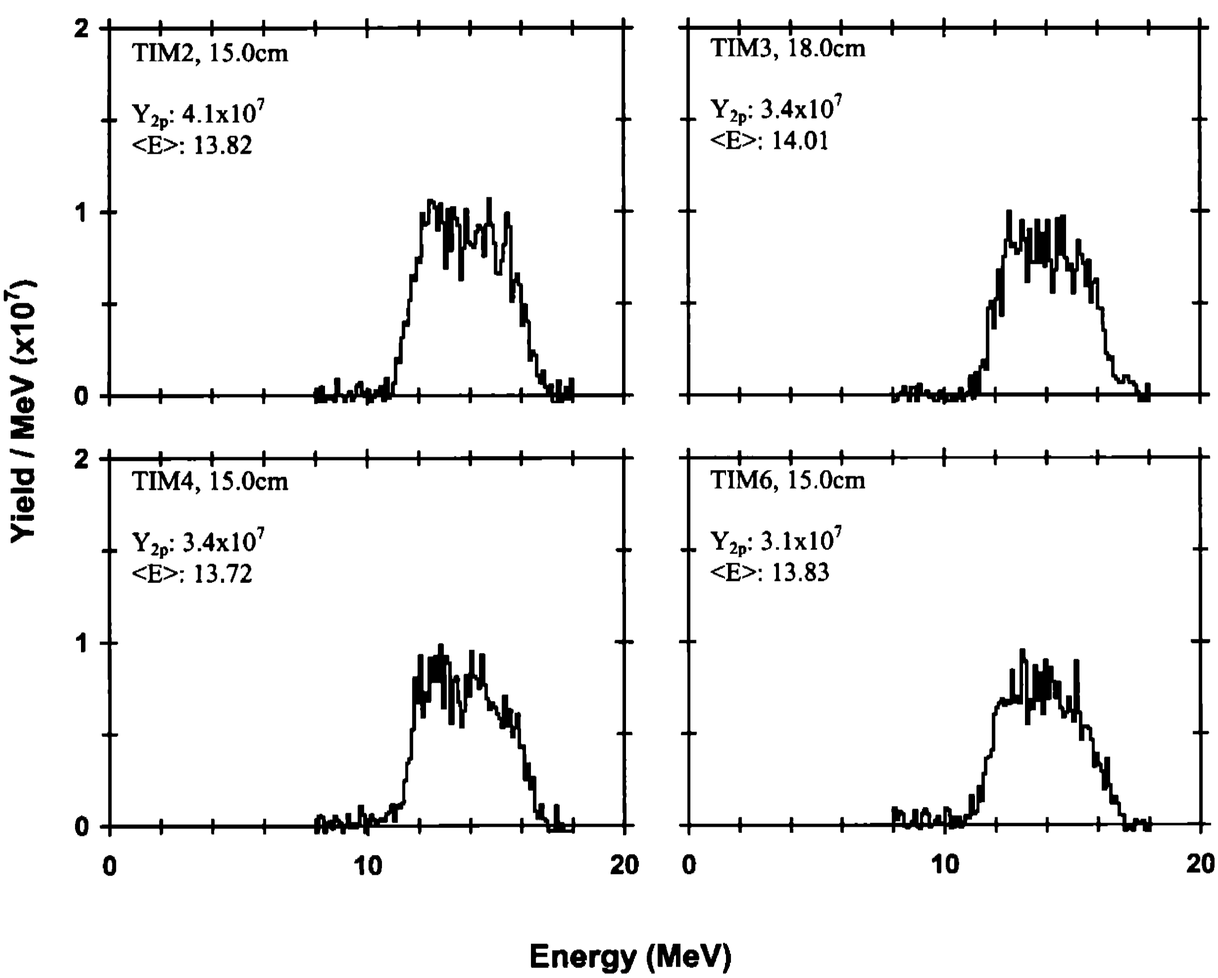

Shot #	Target	On-Target Energy (kJ)	Pulse Shape	Y_{1n} ($x10^{10}$)	$<T_i>_{Y1n}$ (keV)	Bang Time (ps)	Burn Width (ps)
32129	CRYO	24.1	SSD: SG1018	6.2 +/- 0.6	3.6 +/- 0.5	1650 +/- 50	244 +/- 25

$<Y_{2p}>$ ($x10^8$)	Y_{2n} ($x10^8$)	$\rho R_{hot, 2p, hot-spot}$ (mg/cm^2)	$\rho R_{hot, 2n, hot-spot}$ (mg/cm^2)	$\rho R_{hot, 2p, uniform}$ (mg/cm^2)	$\rho R_{hot, 2n, uniform}$ (mg/cm^2)	$<E_{2p}>$ (MeV)	ρR_{total} (mg/cm^2)
1.4 +/- 0.1	7.0 +/- 0.8	13.0 + -3.0	54.8 +5.6 -7.5	52.7 + -41.3	56.7 +6.4 -7.7	13.52 +/- 0.1	46.7 +/- 3.1

Secondary proton spectra from WRF

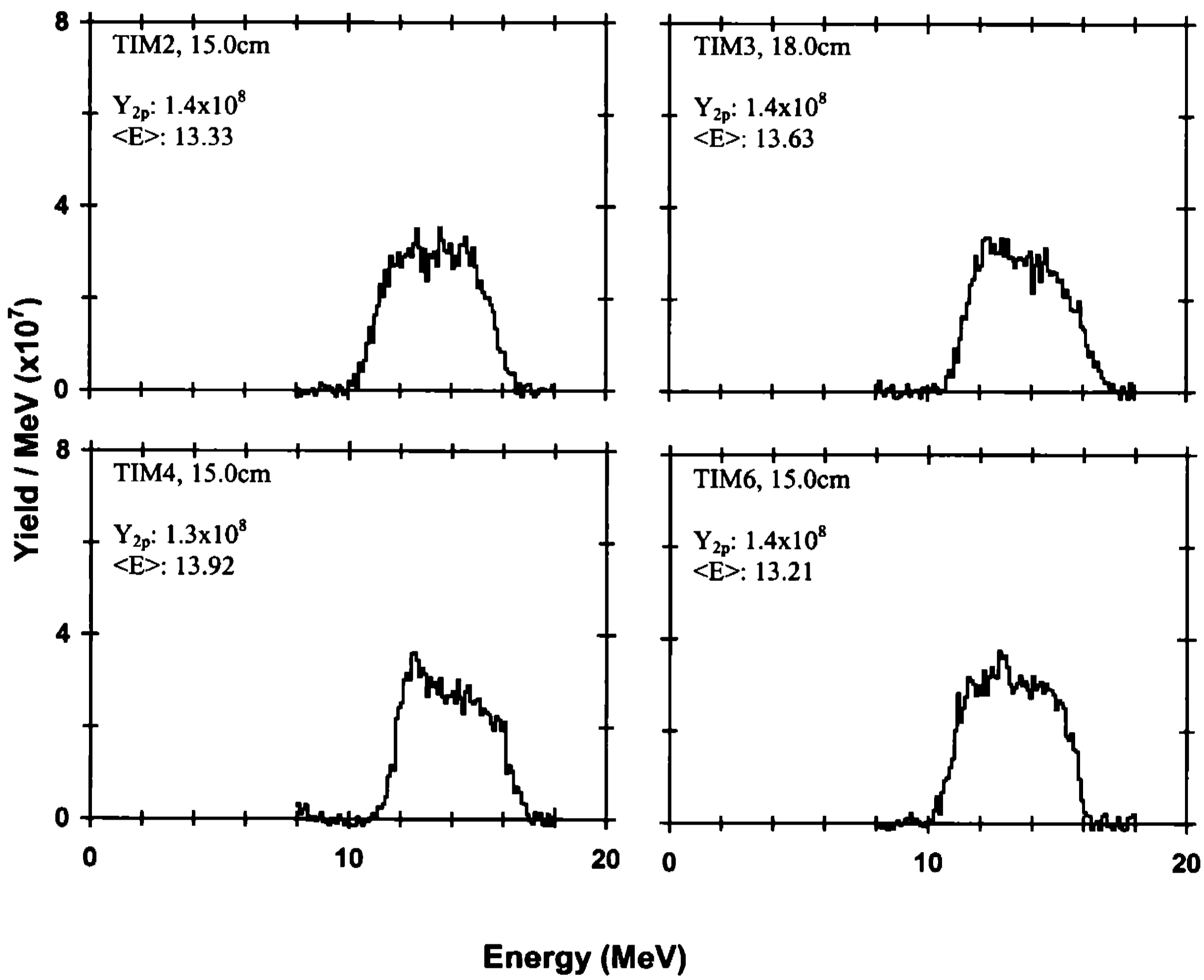

Shot #	Target	On-Target Energy (kJ)	Pulse Shape	Y_{1n} ($x10^{11}$)	$\langle T_i \rangle_{Y1n}$ (keV)	Bang Time (ps)	Burn Width (ps)
32223	CRYO	24.4	SSD: SG1018	1.2 +/- 0.1	3.9 +/- 0.5	1560 +/- 50	300 +/- 25

$\langle Y_{2p} \rangle$ ($x10^8$)	Y_{2n} ($x10^9$)	$\rho R_{hot, 2p,}$ hot-spot (mg/cm^2)	$\rho R_{hot, 2n,}$ hot-spot (mg/cm^2)	$\rho R_{hot, 2p,}$ uniform (mg/cm^2)	$\rho R_{hot, 2n,}$ uniform (mg/cm^2)	$\langle E_{2p} \rangle$ (MeV)	ρR_{total} (mg/cm^2)
3.1 +/- 0.3	1.2 +/- 0.1	16.3 + -4.8	53.3 +5.2 -7.2	N/A	56.2 +5.7 -7.0	13.62 +/- 0.1	43.6 +/- 3.1

Secondary proton spectra from WRF

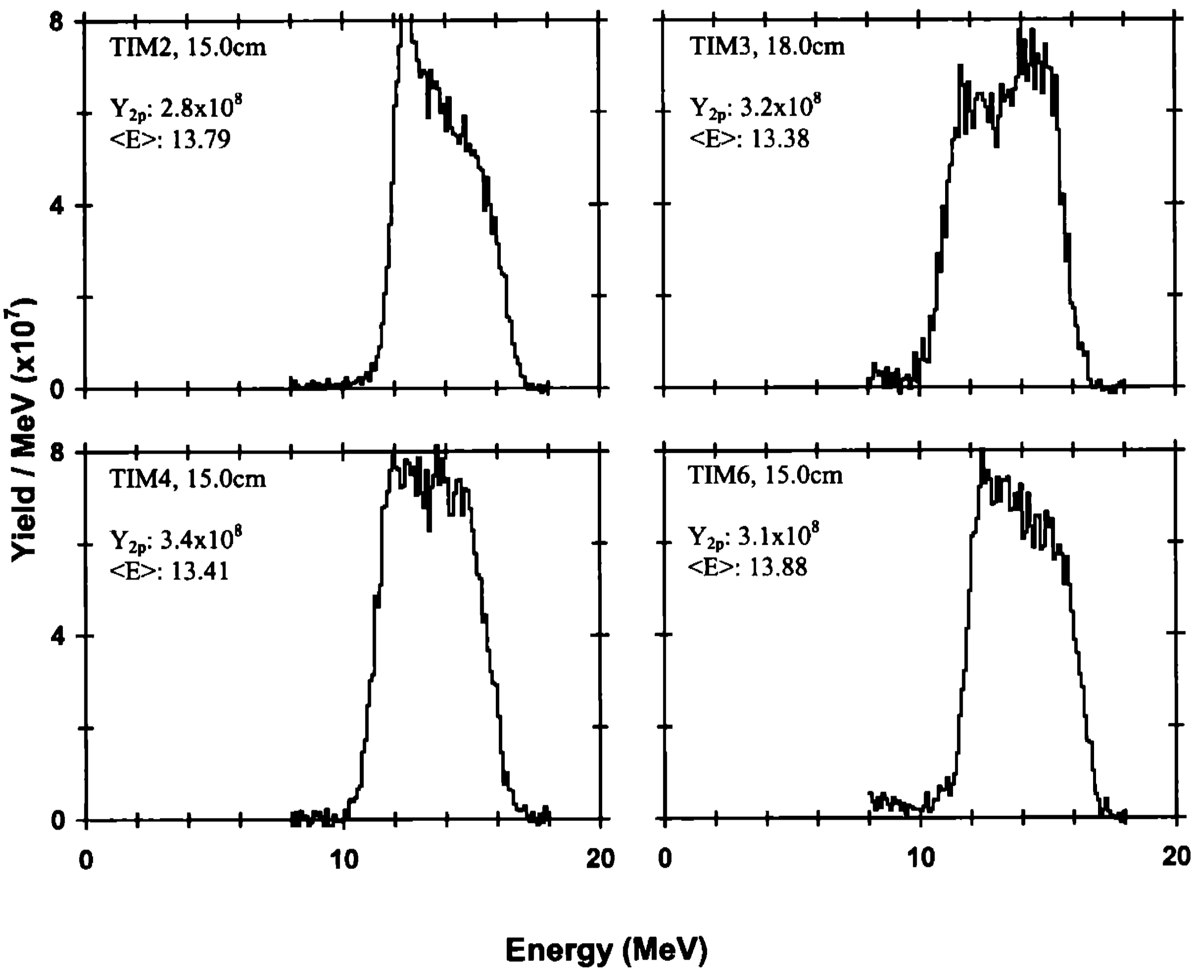

Shot #	Target	On-Target Energy (kJ)	Pulse Shape	Y_{1n} ($x10^{10}$)	$<T_i>_{Y1n}$ (keV)	Bang Time (ps)	Burn Width (ps)
32225	CRYO	25.0	SSD: SG1018	3.2 +/- 0.3	3.7 +/- 0.5	1256 +/- 50	313 +/- 25

$<Y_{2p}>$ ($x10^7$)	Y_{2n} ($x10^8$)	$\rho R_{hot,\ 2p,\ hot\text{-}spot}$ (mg/cm^2)	$\rho R_{hot,\ 2n,\ hot\text{-}spot}$ (mg/cm^2)	$\rho R_{hot,\ 2p,\ uniform}$ (mg/cm^2)	$\rho R_{hot,\ 2n,\ uniform}$ (mg/cm^2)	$<E_{2p}>$ (MeV)	ρR_{total} (mg/cm^2)
3.5 +/- 0.5	1.1 +/- 0.2	> 5.7	> 25.5	7.5 +1.3 -1.1	30.4 +3.1 -4.4	14.48 +/- 0.1	16.2 +/- 3.3

Secondary proton spectra from WRF

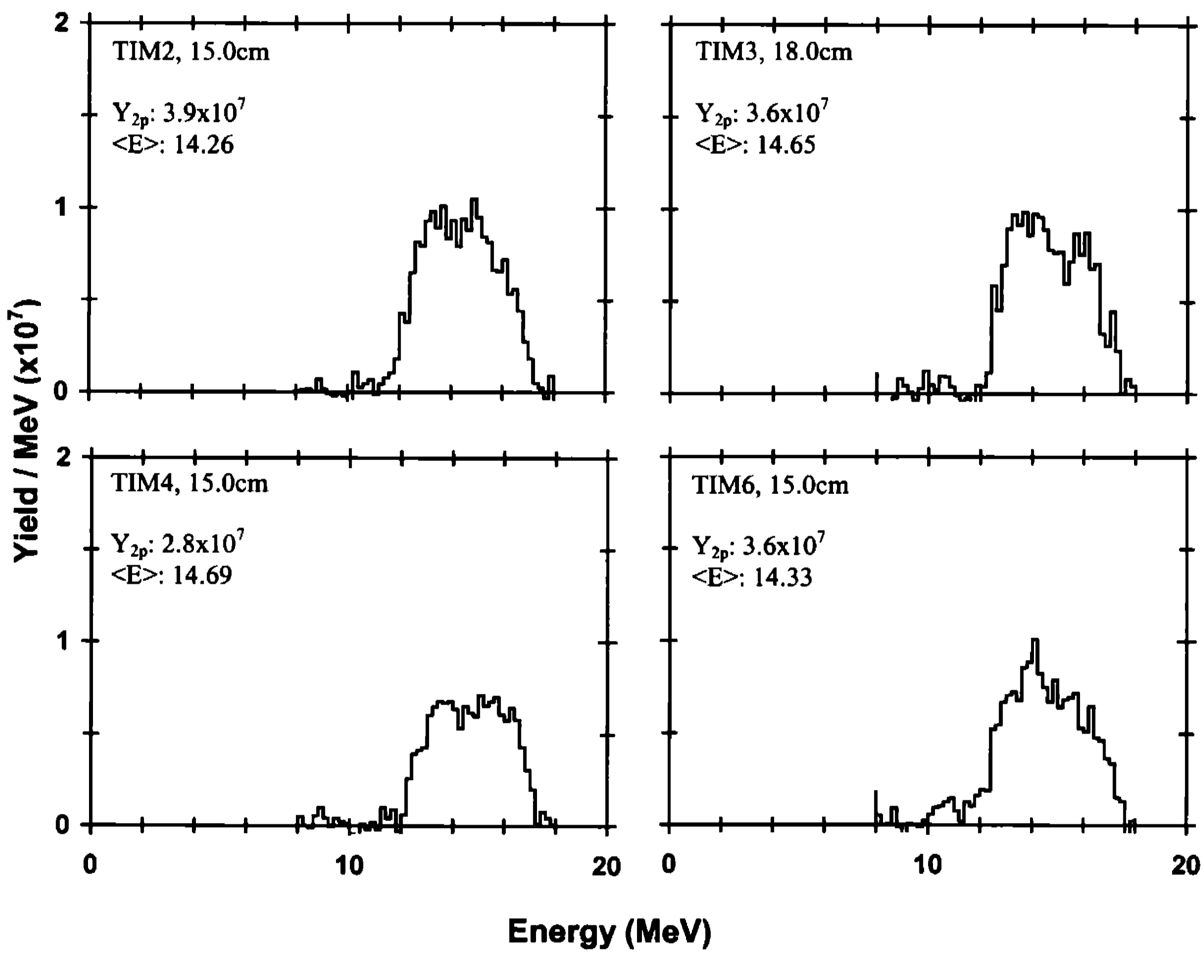

Shot #	Target	On-Target Energy (kJ)	Pulse Shape	Y_{1n} ($x10^{10}$)	$<T_i>_{Y1n}$ (keV)	Bang Time (ps)	Burn Width (ps)
32272	CRYO	23.2	SSD: SG1018	2.8 +/- 0.3	2.4 +/- 0.5	1660 +/- 50	300 +/- 25

$<Y_{2p}>$ ($x10^7$)	Y_{2n} ($x10^8$)	$\rho R_{hot,\,2p,\,hot\text{-}spot}$ (mg/cm^2)	$\rho R_{hot,\,2n,\,hot\text{-}spot}$ (mg/cm^2)	$\rho R_{hot,\,2p,\,uniform}$ (mg/cm^2)	$\rho R_{hot,\,2n,\,uniform}$ (mg/cm^2)	$<E_{2p}>$ (MeV)	ρR_{total} (mg/cm^2)
3.7 +/- 0.6	4.2 +/- 0.5	> 7.0	47.2 +7.5 -8.7	18.7 + -11.0	56.5 +9.0 -10.7	13.76 +/- 0.1	39.2 +/- 3.1

Secondary proton spectra from WRF

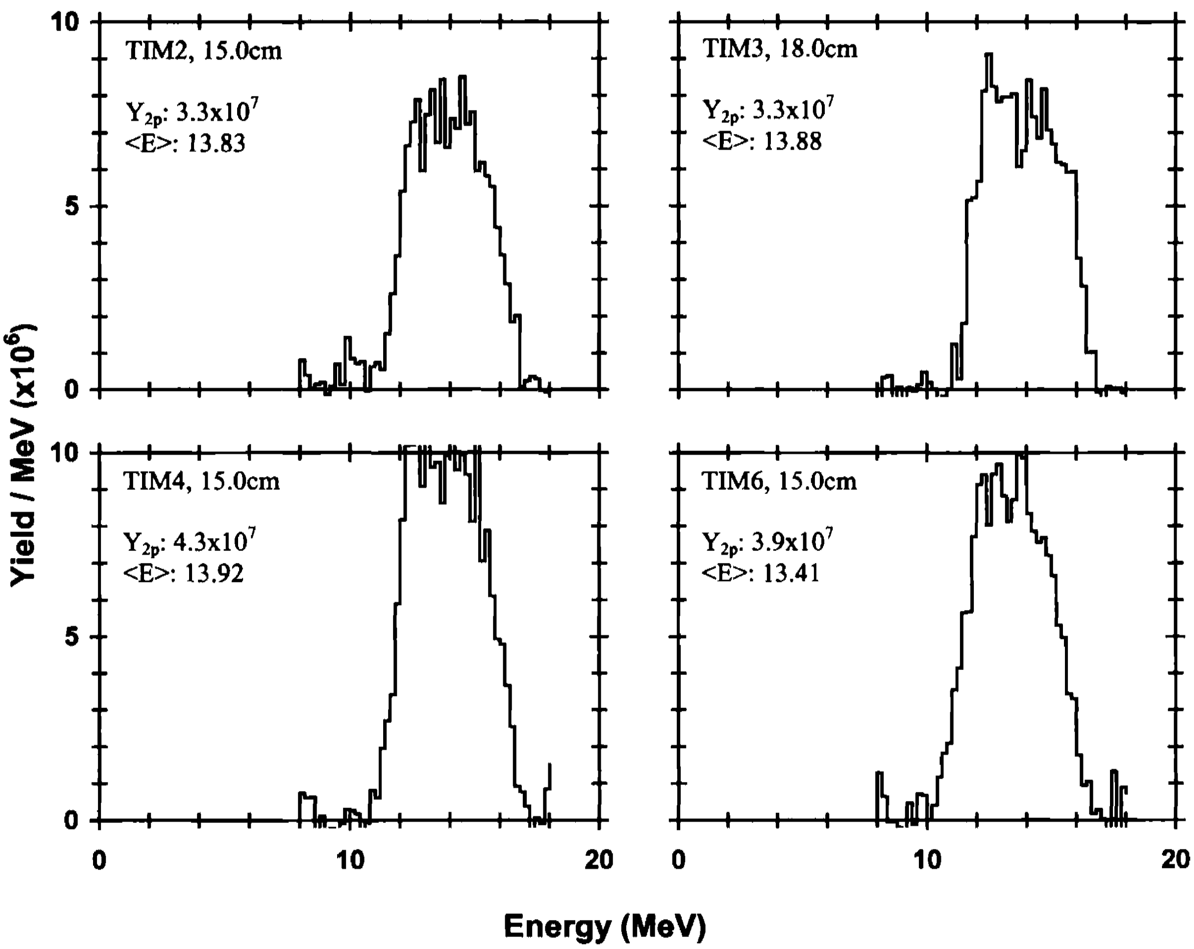

Shot #	Target	On-Target Energy (kJ)	Pulse Shape	Y_{1n} ($x10^{10}$)	$<T_i>_{Y1n}$ (keV)	Bang Time (ps)	Burn Width (ps)
32273	CRYO	23.2	SSD: SG1018	2.8 +/- 0.3	3.1 +/- 0.5	1705 +/- 50	131 +/- 25

$<Y_{2p}>$ ($x10^7$)	Y_{2n} ($x10^8$)	$\rho R_{hot, 2p,}$ hot-spot (mg/cm^2)	$\rho R_{hot, 2n,}$ hot-spot (mg/cm^2)	$\rho R_{hot, 2p,}$ uniform (mg/cm^2)	$\rho R_{hot, 2n,}$ uniform (mg/cm^2)	$<E_{2p}>$ (MeV)	ρR_{total} (mg/cm^2)
2.5 +/- 0.4	2.9 +/- 0.4	4.4 +0.8 -1.1	48.1 +5.5 -7.3	6.1 +1.1 -1.0	49.6 +6.3 -7.4	14.21 +/- 0.1	25.0 +/- 3.2

Secondary proton spectra from WRF

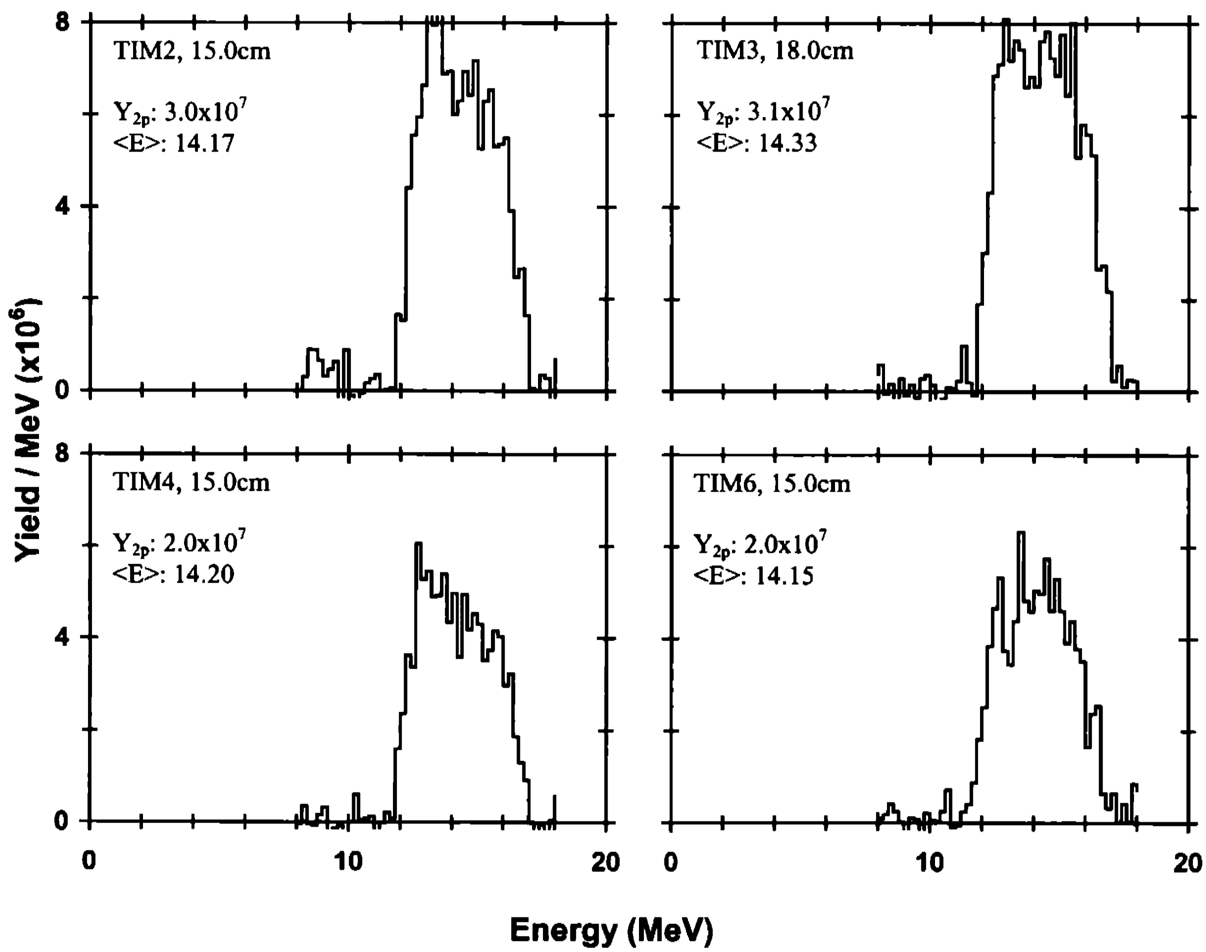

Shot #	Target	On-Target Energy (kJ)	Pulse Shape	Y_{1n} ($x10^{10}$)	$<T_i>_{Y1n}$ (keV)	Bang Time (ps)	Burn Width (ps)
32845	CRYO	23.5	SSD: SG1018	8.8 +/- 0.9	4.2 +/- 0.5	1617 +/- 50	243 +/- 25

$<Y_{2p}>$ ($x10^8$)	Y_{2n} ($x10^8$)	$\rho R_{hot, 2p, hot-spot}$ (mg/cm^2)	$\rho R_{hot, 2n, hot-spot}$ (mg/cm^2)	$\rho R_{hot, 2p, uniform}$ (mg/cm^2)	$\rho R_{hot, 2n, uniform}$ (mg/cm^2)	$<E_{2p}>$ (MeV)	ρR_{total} (mg/cm^2)
1.7 +/- 0.2	9.2 +/- 1.0	9.8 +1.7 -1.5	57.0 +5.5 -7.7	16.5 +7.8 -4.3	60 +5.8 -7.2	13.76 +/- 0.1	39.2 +/- 3.1

Secondary proton spectra from WRF

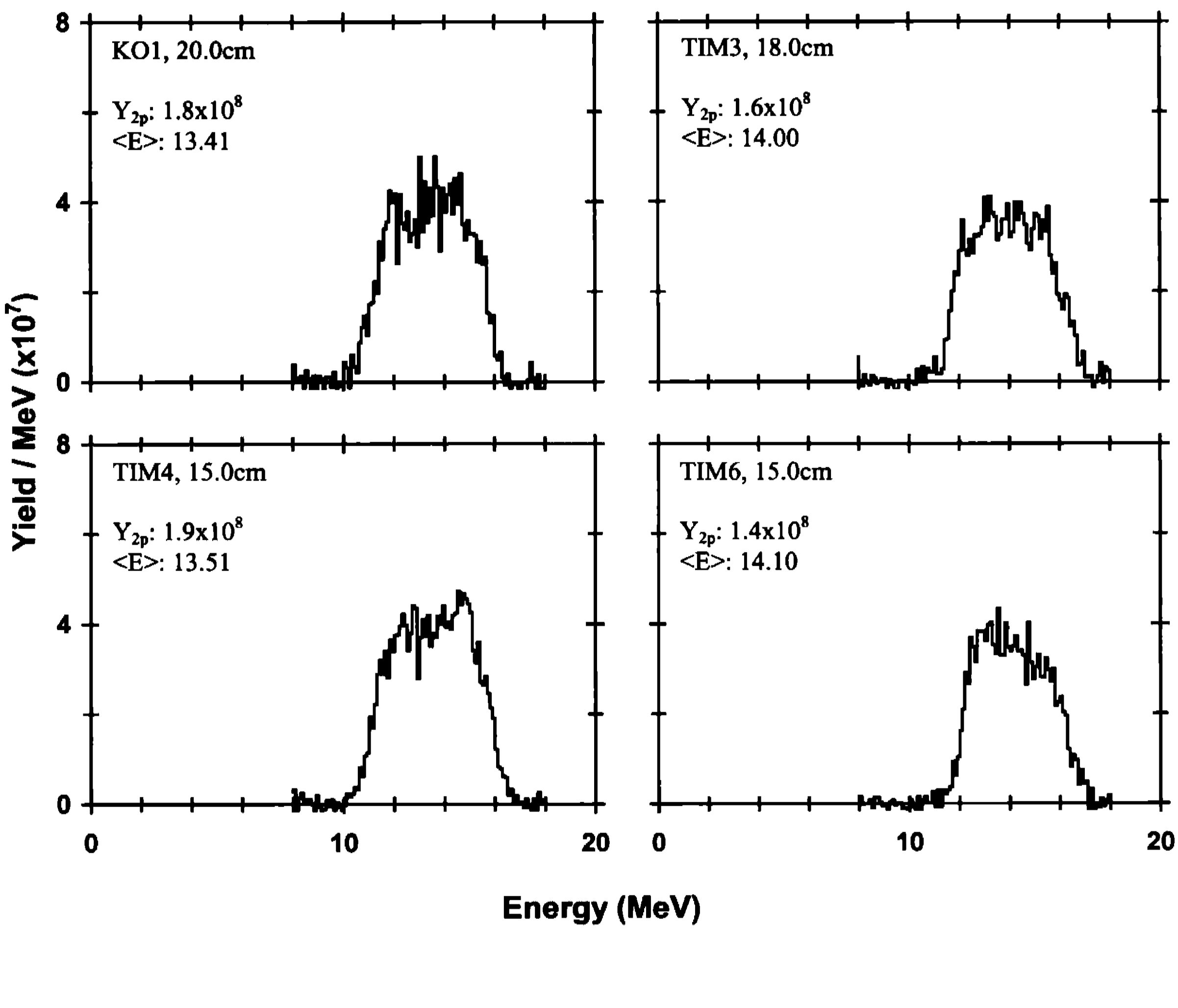

Shot #	Target	On-Target Energy (kJ)	Pulse Shape	Y_{1n} ($x10^{10}$)	$<T_i>_{Y1n}$ (keV)	Bang Time (ps)	Burn Width (ps)
33412	CRYO	21.5	SSD: SG1018	3.3 +/- 0.3	5.5 +/- 0.5	1250 +/- 50	550 +/- 25

$<Y_{2p}>$ ($x10^7$)	Y_{2n} ($x10^7$)	$\rho R_{hot,\,2p,}$ hot-spot (mg/cm^2)	$\rho R_{hot,\,2n,}$ hot-spot (mg/cm^2)	$\rho R_{hot,\,2p,}$ uniform (mg/cm^2)	$\rho R_{hot,\,2n,}$ uniform (mg/cm^2)	$<E_{2p}>$ (MeV)	ρR_{total} (mg/cm^2)
2.1 +/- 0.3	7.5 +/- 1.2	3.4 +0.6 -0.8	19.1 +3.3 -4.7	4.4 +0.7 -1.1	24.2 +3.8 -5.6	14.88	N/A

Secondary proton spectra from WRF

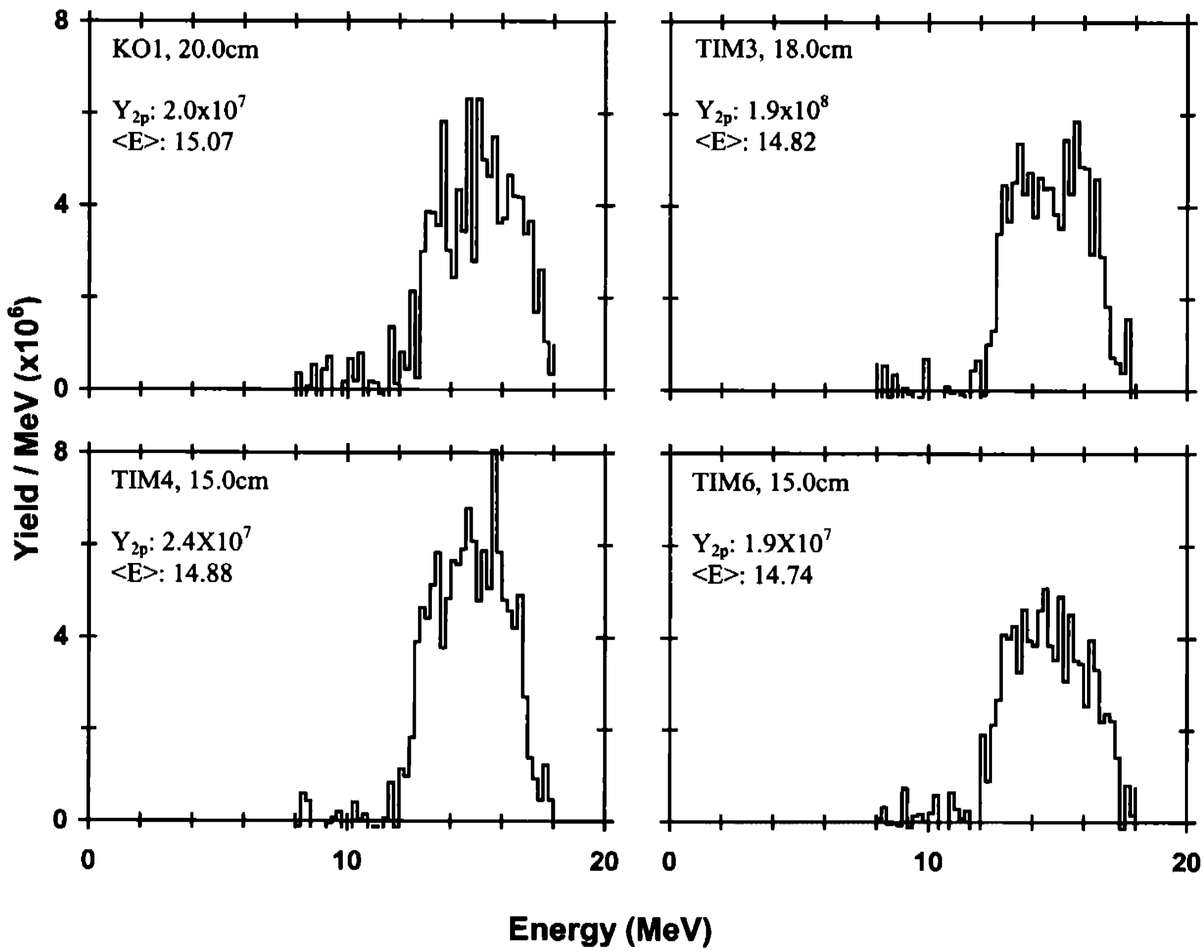

Shot #	Target	On-Target Energy (kJ)	Pulse Shape	Y_{1n} ($x10^{10}$)	$\langle T_i \rangle_{Y1n}$ (keV)	Bang Time (ps)	Burn Width (ps)
33413	CRYO	22.0	SSD: SG1018	6.7 +/- 0.7	3.2 +/- 0.5	1614 +/- 50	204 +/- 25

$\langle Y_{2p} \rangle$ ($x10^8$)	Y_{2n} ($x10^8$)	$\rho R_{hot, 2p,}$ hot-spot (mg/cm^2)	$\rho R_{hot, 2n,}$ hot-spot (mg/cm^2)	$\rho R_{hot, 2p,}$ uniform (mg/cm^2)	$\rho R_{hot, 2n,}$ uniform (mg/cm^2)	$\langle E_{2p} \rangle$ (MeV)	ρR_{total} (mg/cm^2)
1.3 +/- 0.1	7.2 +/- 0.8	10.8 + -2.4	49.8 +5.5 -7.2	37.9 + -29.1	51.5 +6.3 -7.4	13.66 +/- 0.1	42.3 +/- 3.1

Secondary proton spectra from WRF

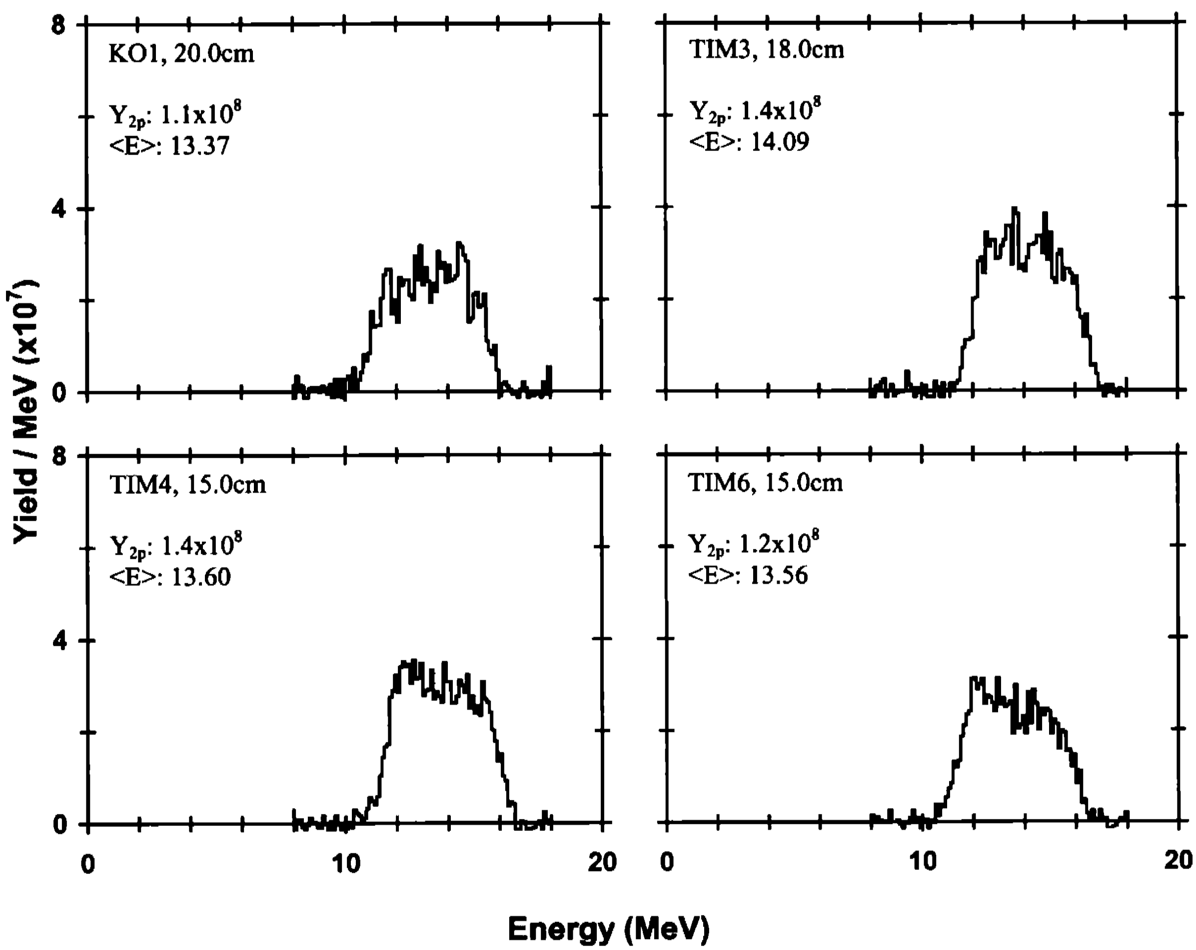

Shot #	Target	On-Target Energy (kJ)	Pulse Shape	Y_{1n} ($x10^{10}$)	$<T_i>_{Y1n}$ (keV)	Bang Time (ps)	Burn Width (ps)
33415	CRYO	23.1	SSD: SG1018	4.2 +/- 0.4	4.0 +/- 0.5	1641 +/- 50	251 +/- 25

$<Y_{2p}>$ ($x10^7$)	Y_{2n} ($x10^8$)	$\rho R_{hot, 2p,}$ hot-spot (mg/cm^2)	$\rho R_{hot, 2n,}$ hot-spot (mg/cm^2)	$\rho R_{hot, 2p,}$ uniform (mg/cm^2)	$\rho R_{hot, 2n,}$ uniform (mg/cm^2)	$<E_{2p}>$ (MeV)	ρR_{total} (mg/cm^2)
5.4 +/- 0.8	2.4 +/- 0.3	6.4 +1.2 -1.6	37.8 +4.3 -6.3	9.0 +1.8 -1.5	43.2 +4.4 -6.3	14.06 +/- 0.1	29.8 +/- 3.1

Secondary proton spectra from WRF

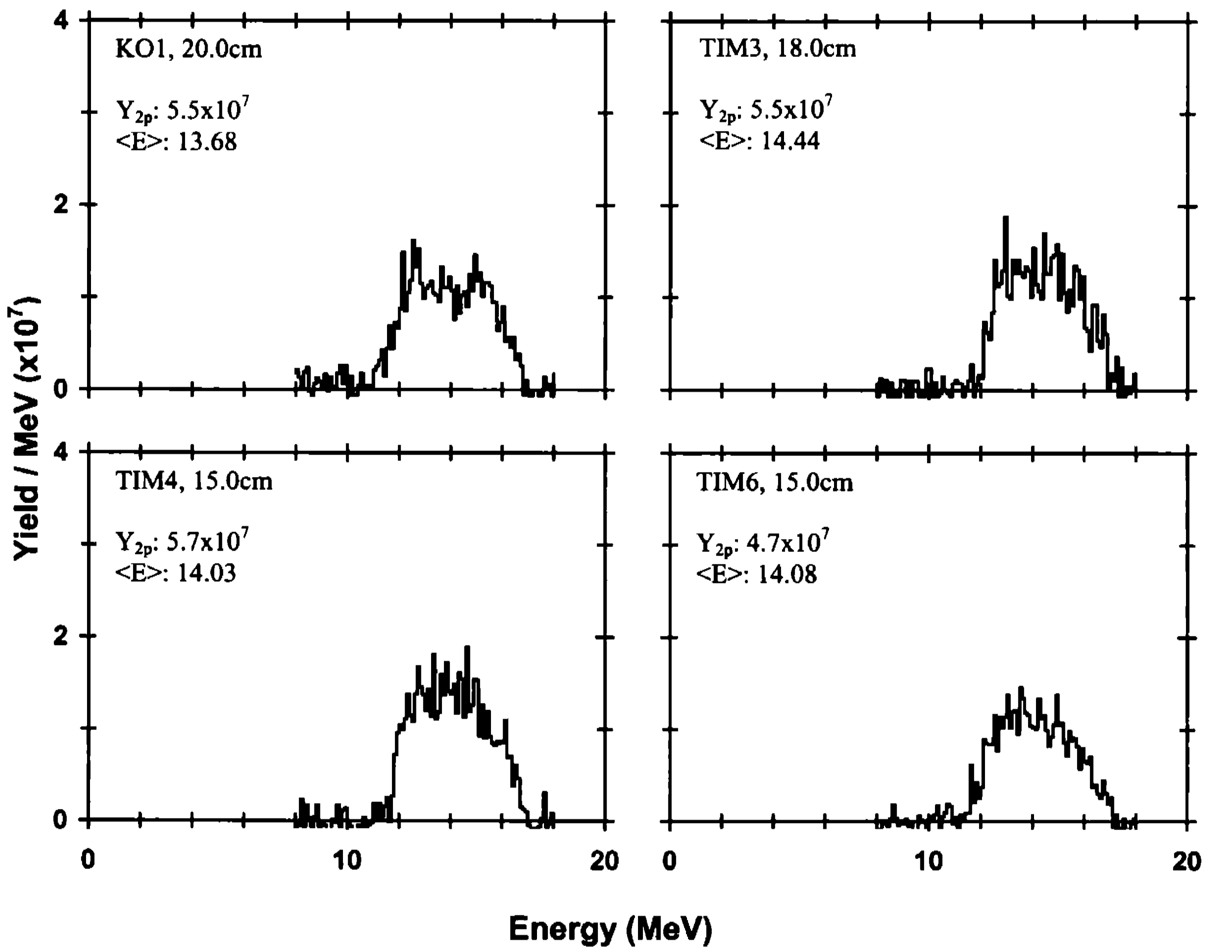

Shot #	Target	On-Target Energy (kJ)	Pulse Shape	Y_{1n} ($x10^{10}$)	$<T_i>_{Y1n}$ (keV)	Bang Time (ps)	Burn Width (ps)
33599	CRYO	22.7	SSD: SG1018	6.5 +/- 0.7	2.9 +/- 0.5	1654 +/- 50	191 +/- 25

$<Y_{2p}>$ ($x10^8$)	Y_{2n} ($x10^8$)	$\rho R_{hot,\,2p,}$ hot-spot (mg/cm²)	$\rho R_{hot,\,2n,}$ hot-spot (mg/cm²)	$\rho R_{hot,\,2p,}$ uniform (mg/cm²)	$\rho R_{hot,\,2n,}$ uniform (mg/cm²)	$<E_{2p}>$ (MeV)	ρR_{total} (mg/cm²)
1.4 +/- 0.1	6.9 +/- 0.8	> 9.2	46.6 +5.6 -7.1	N/A	48.3 +6.4 -7.4	13.61 +/- 0.1	43.9 +/- 3.1

Secondary proton spectra from WRF

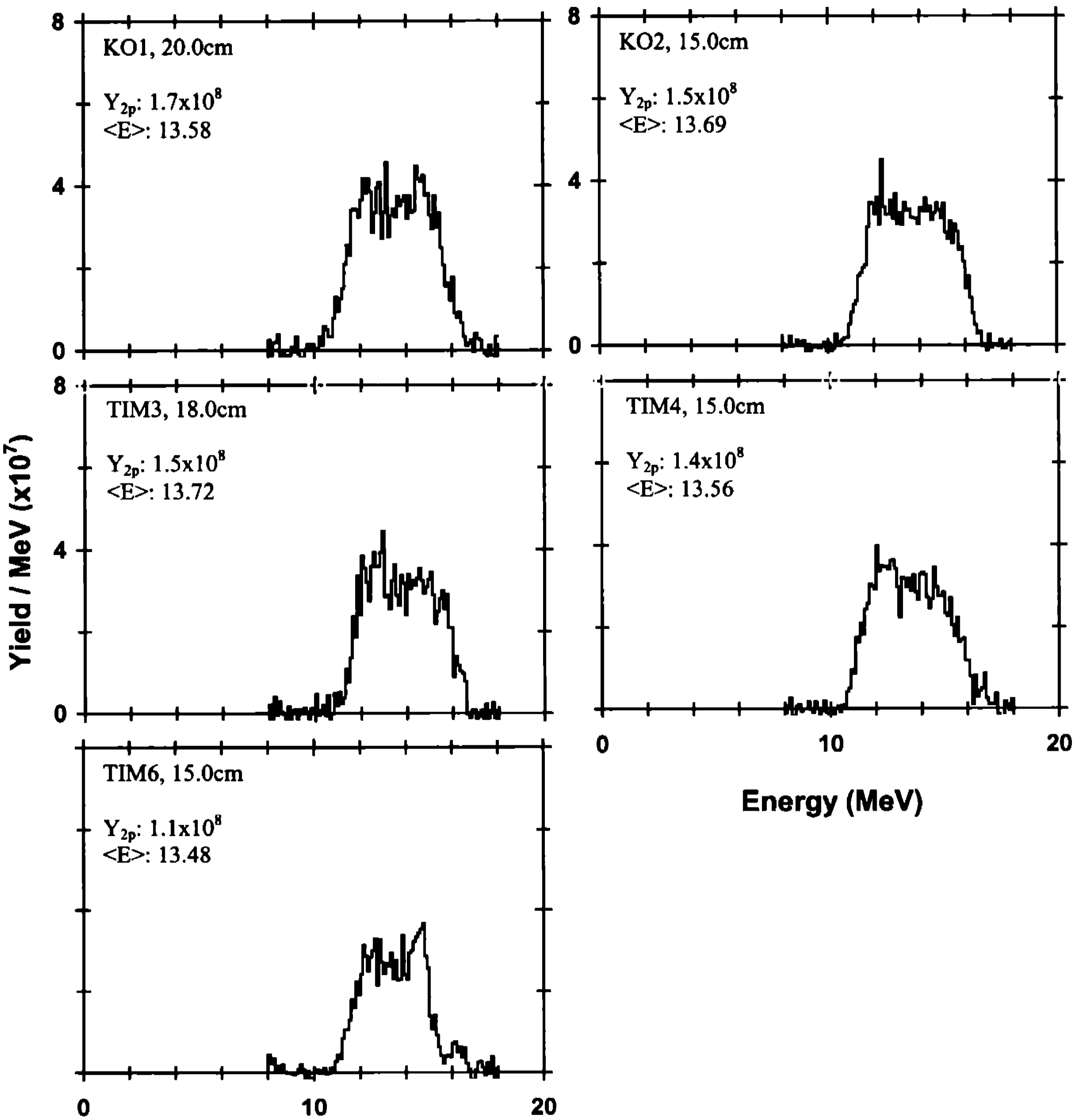

Shot #	Target	On-Target Energy (kJ)	Pulse Shape	Y_{1n} ($x10^{10}$)	$<T_i>_{Y1n}$ (keV)	Bang Time (ps)	Burn Width (ps)
33603	CRYO	22.6	SSD: SG1018	3.9 +/- 0.4	3.2 +/- 0.5	1672 +/- 50	179 +/- 25

$<Y_{2p}>$ ($x10^7$)	Y_{2n} ($x10^8$)	$\rho R_{hot, 2p,}$ hot-spot (mg/cm^2)	$\rho R_{hot, 2n,}$ hot-spot (mg/cm^2)	$\rho R_{hot, 2p,}$ uniform (mg/cm^2)	$\rho R_{hot, 2n,}$ uniform (mg/cm^2)	$<E_{2p}>$ (MeV)	ρR_{total} (mg/cm^2)
7.7 +/- 1.2	3.5 +/- 0.4	11.4 + -2.8	45.6 +5.1 -6.8	43.8 + -36.4	47.2 +5.7 -6.7	13.76 +/- 0.1	39.2 +/- 3.1

Secondary proton spectra from WRF

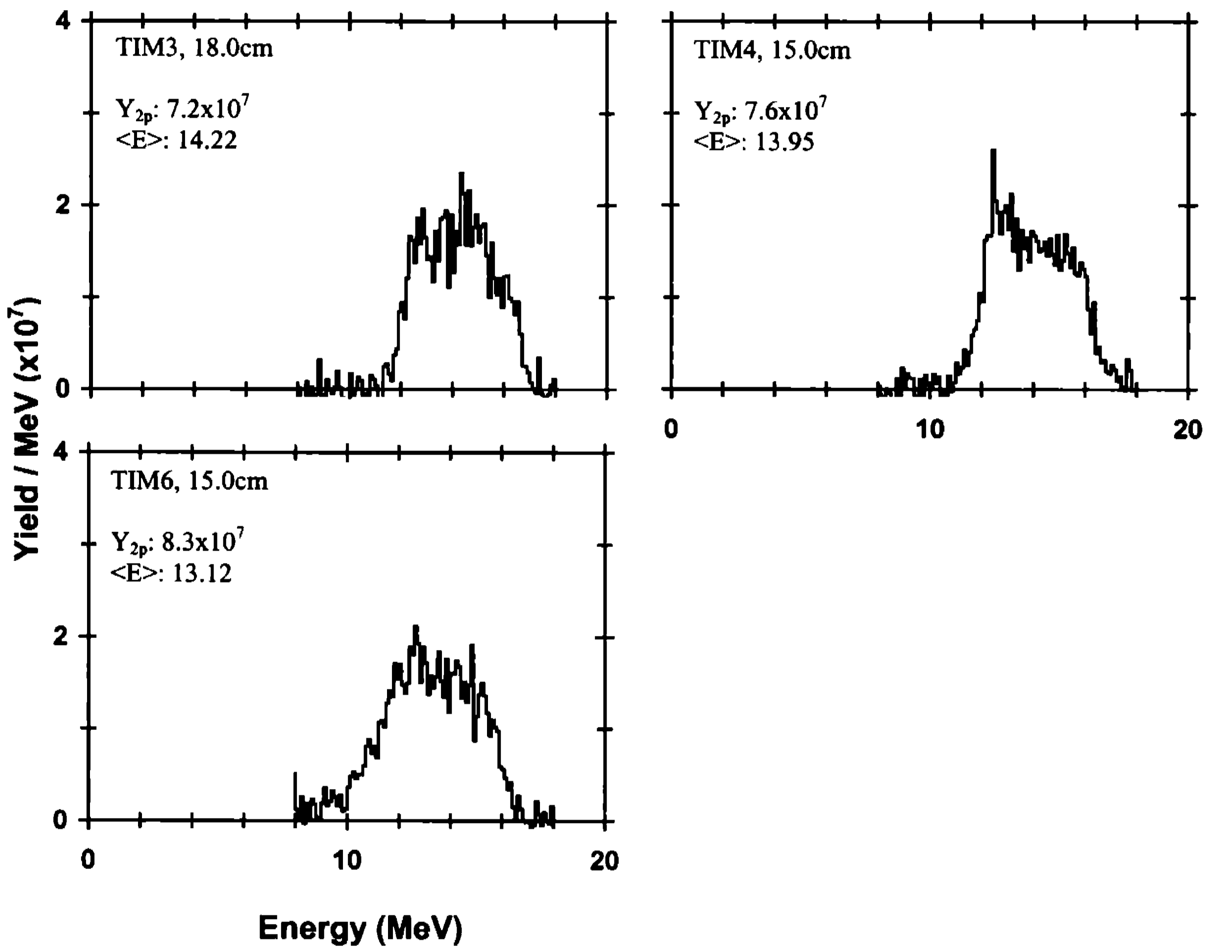

Shot #	Target	On-Target Energy (kJ)	Pulse Shape	Y_{1n} ($x10^{10}$)	$\langle T_i \rangle_{Y1n}$ (keV)	Bang Time (ps)	Burn Width (ps)
33688	CRYO	22.6	SSD: SG1018	4.7 +/- 0.5	3.1 +/- 0.5	1612 +/- 50	213 +/- 25

$\langle Y_{2p} \rangle$ ($x10^7$)	Y_{2n} ($x10^8$)	$\rho R_{hot,\,2p,}$ hot-spot (mg/cm^2)	$\rho R_{hot,\,2n,}$ hot-spot (mg/cm^2)	$\rho R_{hot,\,2p,}$ uniform (mg/cm^2)	$\rho R_{hot,\,2n,}$ uniform (mg/cm^2)	$\langle E_{2p} \rangle$ (MeV)	ρR_{total} (mg/cm^2)
8.2 +/- 1.2	5.2 +/- 0.6	8.2 +5.0 -2.1	49.3 +5.7 -7.3	23.8 + -12.7	51.3 +6.5 -7.6	13.83 +/- 0.1	37.0 +/- 3.1

Secondary proton spectra from WRF

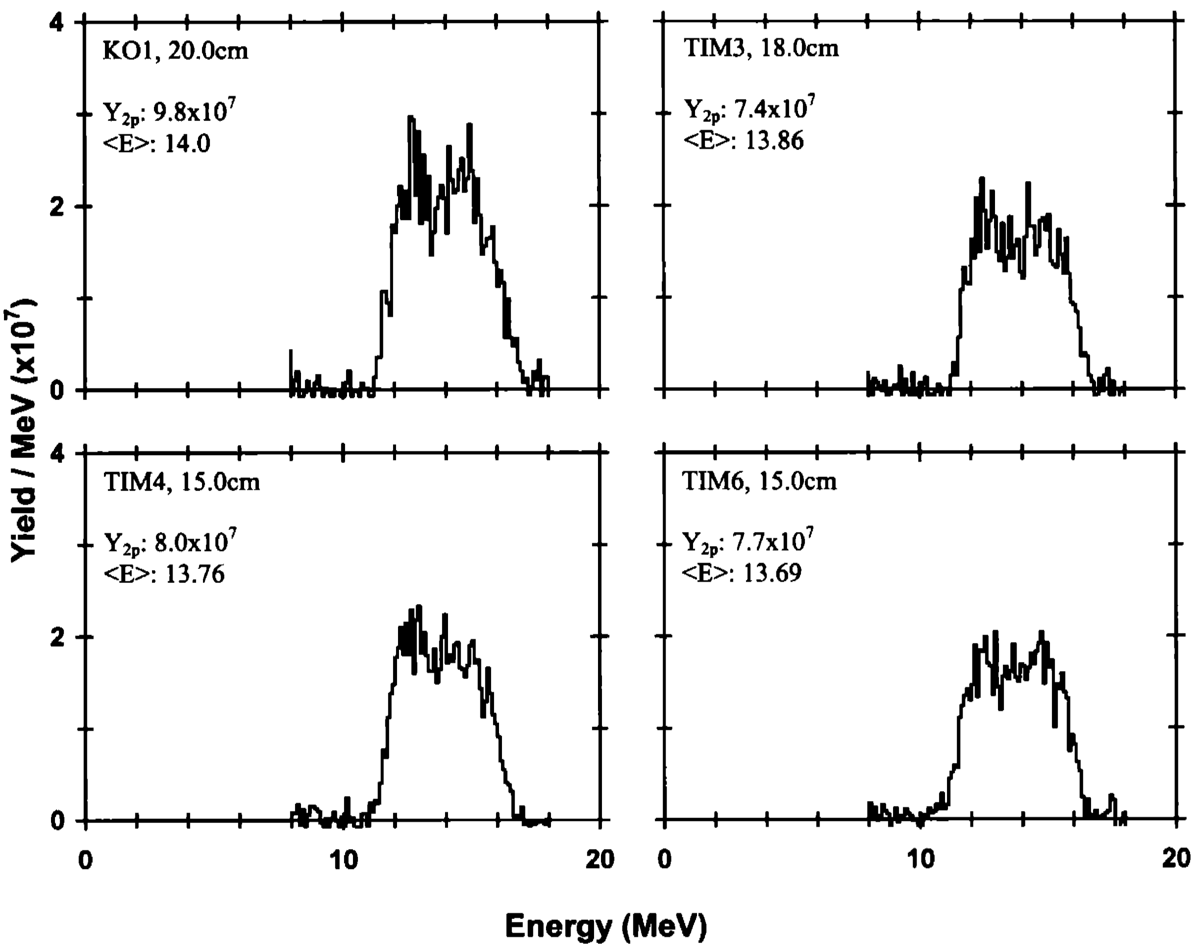

Bibliography

[1] J. H. Nuckolls, L. Wood, A. Thiessen, and G. B. Zimmerman, Nature **239**, 139 (1972).

[2] S. W. Haan, S. Pollanine, J. D. Lindl *et al.*, Phys. Plasmas **2**, 2480 (1995).

[3] J. D. Lindl, R. L. McCrory, and E. M. Campbell, Phys. Today **45**, 32 (1992).

[4] J. D. Lindl, Phys. Plasmas **2**, 3933 (1995).

[5] L. M. Hively, Nuclear Fusion **17**, 873 (1997).

[6] T. R. Boehly, D. L. Brown, R. S. Craxton *et al.*, Opt. Commun. **133**, 495 (1997)

[7] F. H. Séguin, J. A. Frenje, C. K. Li *et al.*, Rev. Sci. Instrum. **74**, 975 (2003).

[8] C. K. Li and R. D. Petrasso, Phys. Rev. Lett. **70**, 3059 (1993).

[9] R. A. Lerche, D. W. Phillion, and G. L. Tietbohl, Rev. Sci. Instrum. **66**, 933 (1995).

[10] H. Brysk, Plasma Physics **15**, 611 (1973).

[11] S. Glasstone and R. H. Lovberg, *Controlled Thermonuclear Reactions: An Introduction to Theory and Experiment* (Van Nostrand, Princeton, NJ, 1960).

[12] G. Lehner, Z. Physik **232**, 174 (1970)